

Flattened Gaussian Beam for Laser Paint Removal

Neil Carl du Preez

Thesis presented in partial fulfilment of the requirements for the degree
Master of Science at the Stellenbosch University



Supervisors: Prof. Erich G. Rohwer, Dr. Lourens R. Botha

March 2011

DECLARATION

By submitting this thesis electronically, I declare that the entirety of the work contained therein is my own, original work, that I am the sole author thereof (save to the extent explicitly otherwise stated), that the reproduction and publication thereof by Stellenbosch University will not infringe any third party rights and that I have not previously in its entirety or in part submitted it for obtaining any qualification.

Date : 1 March 2011

Copyright © 2011 Stellenbosch University

All rights reserved

ABSTRACT

Lasers are commonly used in the industry for various applications such as laser cutting, laser drilling, lithography, medical applications, surface cleaning and a myriad of other applications. In any application of a laser the beam properties are significant. In the paint removal application discussed in this thesis, the beam properties of the laser beam can have a large impact on the efficiency of the paint removal process. The pulse energy or the average output power of the laser is normally an important parameter in laser materials processing applications. The spatial profile or intensity distribution of the beam also has an influence on the process. The propagation of the laser beam from the laser to the working point is also significant in applying the laser beam to the material. In the ideal scenario one would like to control all the parameters of the laser in terms of the output, in energy or output power, the propagation of the laser beam and the intensity distribution of the beam.

The process of laser-based paint removal is no different to this. In this process a TEA CO₂ laser is used for the ablation of paint from a substrate. In this application high pulse energy is required from the laser together with good beam propagation properties for delivery of the beam over a long distance. For this application the multimode beam of the TEA CO₂ laser can be applied for the paint removal. The multimode beam has sufficiently high pulse energy for the paint removal process, but is not suitable for propagating over long distances through a beam path with a finite aperture. Furthermore the multimode beam does not have a uniform energy intensity distribution. It would therefore be ideal if the TEA CO₂ laser could be designed with a custom beam that has a uniform intensity distribution, high pulse energy and good beam propagation.

These requirements lead to the study of flattened irradiance profile laser beams. In this thesis flattened irradiance profile beams in the form of Flattened Gaussian beams are investigated. The theory of the Flattened Gaussian profile as well as the propagation of the beam is investigated. Furthermore the generation of such a beam internally to the laser resonator is studied. In succession to this a custom laser resonator was designed and implemented on the TEA CO₂ laser. The resulting Flattened Gaussian Beam was characterised and applied to the application of laser paint removal. It was finally shown that the Flattened Gaussian Beam could be successfully generated and applied with equal success in the application of laser paint removal.

OPSOMMING

Lasers word algemeen in die industrie gebruik vir toepassings soos laser snywerk, laser boorwerk, litografie, mediese toepassings, oppervlakreiniging en verskeie ander. In enige toepassing van 'n laser is die eienskappe van die laserbundel van groot belang vir die proses. In die verf verwydering toepassing wat bespreek word in hierdie tesis het die bundel eienskappe 'n groot invloed op die effektiwiteit van die verf stropings proses. Die pulsenergie of uitset drywing van die laser is gewoonlik 'n belangrike parameter in 'n materiaalverwerkings toepassing. Die ruimtelike profile of energie intensiteitprofiel van die bundel het ook 'n invloed op die proses. Die voortplanting van die bundel vanaf die laser na die werkpunt het ook 'n beduidende invloed op die toepassing van die laserbundel op die materiaal. In die ideale geval sal mens graag al die parameters van die laserbundel soos pulsenergie of drywing, die bundel voortplanting en energie intensiteitprofiel wil beheer.

Die toepassing van die laser vir verfverwydering vereis ook die beheer van hierdie unieke parameters wat reeds genoem is. In hierdie proses is 'n TEA CO₂ laser gebruik vir die verwydering van verf van 'n substraat. Die toepassing vereis hoë pulsenergie saam met goeie bundel voortplantingseienskappe vir lewering van die bundel oor lang afstande. Die multimode bundel van die laser kan gebruik word vir hierdie toepassing. Die multimode bundel bevat genoegsame energie vir die verfstropings proses maar is nie geskik vir voortplanting oor lang afstande deur 'n bundelpad wat 'n beperking op die bundel grootte het nie. Verder het die multimode bundel ook nie 'n uniforme energie intensiteitprofiel nie. Dit sou ideal wees as die TEA CO₂ laser toegerus kon word met 'n toepassingsgerigte bundel wat hoë puls energie, goeie bundel voortplanting en 'n uniforme intensiteitprofiel het.

Hierdie vereiste het gelei tot die studie van laserbundels met 'n uniforme plat energie intensiteitprofiel. In hierdie tesis word plat intensiteit bundels in die vorm van plat Gaussiese bundels ondersoek. Die teorie van plat Gaussiese bundels sowel as die voortplanting van hierdie bundels word hier ondersoek. Verder word die opwekking van hierdie bundels intern tot die laserresonator ook ondersoek. Na die ondersoek is daar oorgegaan in die ontwerp en implementering van 'n doelgemaakte resonator op 'n TEA CO₂ laser. Die resonator het 'n plat Gaussiese bundel as uitset gelever. Die bundel was gevolglik gekarakteriseer en aangewend in 'n

verfstropings toepassing. Ten einde is daar getoon dat 'n plat Gaussiese bundel suksesvol opgewek en toegepas kon word.

ACKNOWLEDGEMENTS

I would like to acknowledge and thank the following people and entities for their significant contributions to this thesis:

- My supervisor Dr. L.R. Botha for his encouragement, guidance, instruction, helpful discussions and insights during the work on this thesis. I also thank him for his role as a mentor to me on a continued basis over the last nine years.
- My supervisor Prof. E.G. Rohwer for his encouragement, guidance and understanding.
- Prof. A. Forbes for his significant contributions to the work that was performed with the DOE mirror. I also thank him for his mentorship and guidance now and in the past.
- Dr. S.P. Van Heerden for his mentorship and guidance in the past.
- My employers Dr. E. Ronander and Mr. C.D. Swart of SDI Lasers (Pty) Ltd for the opportunity to perform this work. I also thank them and my other colleagues at SDI Lasers for their encouragement.
- Mr. M.J. Botha for his participation in performing the laboratory work.
- The Department of Science and Technology (DST) - Innovation Fund (IF) which supported the work by grants for the project T60003, *Environmentally friendly laser paint stripping method for aircraft*, under which the laser used in this thesis was developed.
- My mother and father for their encouragement and support in completing this thesis.
- Mr. L. Kruger for encouragement and help with the proof reading and finalisation of the model and the manuscript.
- Ms. M. Sutton for her encouragement, support and prayer in completing this thesis.
- Mr. J. Robbie and Mr. D. Strauss for their encouragement and prayer.
- My heavenly Father for the blessing of the opportunity to be able to do this work.

TABLE OF CONTENTS

DECLARATION	i
ABSTRACT.....	ii
OPSOMMING	iii
ACKNOWLEDGEMENTS	v
LIST OF TABLES	viii
LIST OF FIGURES	ix
ANNEXURES	xi
ABBREVIATIONS	xii
1 INTRODUCTION	1
1.1 Topic introduction	1
1.2 Objectives.....	1
1.3 Research problem	2
1.4 Research questions	2
1.5 Restrictions.....	2
1.6 Assumptions	3
1.7 Chapter outline	3
2 LITERATURE REVIEW	5
3 BACKGROUND THEORY	7
3.1 Flattened irradiance profile beams	7
3.1.1 Flattened Gaussian beams with circular symmetry.....	8
3.1.2 Propagation of Flattened Gaussian beams with circular symmetry.....	11
3.1.3 Flattened Gaussian beams with rectangular symmetry.....	16
3.2 Beam shaping methods.....	20
3.3 Laser beam shaping internal to the laser resonator	22
3.4 Implementations of laser beam shaping	29
3.5 Stability analysis.....	32
4 METHODOLOGY.....	36

4.1	Design of the laser resonator with internal beam shaping.....	36
4.1.1	Propagating the FGB.....	36
4.1.2	Resonator design	39
4.1.3	Stability analysis	44
4.2	Laser beam characterisation	50
4.2.1	Pulse energy measurements	50
4.2.2	Beam profile measurements.....	50
4.2.3	Beam propagation measurements	54
5	RESULTS	60
5.1	Laser characterisation.....	60
5.1.1	Multimode beam results.....	60
5.1.2	TEM ₀₀ beam results	63
5.2	Installation of DOE in the laser resonator and FGB results.....	66
5.2.1	FGB results – open gain volume.....	66
5.2.2	FGB results – aperture in gain volume	69
5.3	Paint removal results	71
6	CONCLUSIONS, SUMMARY AND RECOMMENDATIONS.....	77
6.1	Conclusion.....	77
6.1.1	FGB theory.....	77
6.1.2	FGB implementation.....	78
6.1.3	FGB results	79
6.1.4	Paint removal results.....	82
6.2	Summary	83
6.3	Recommendations	83
7	REFERENCES.....	85
8	APPENDICES	88
8.1	MATLAB program.....	88

LIST OF TABLES

Table 5-1 – Multimode beam results	62
Table 5-2 – TEM ₀₀ beam results	65
Table 5-3 – FGB beam results	68
Table 5-4 - FGB beam results	70
Table 6-1 - Summary of laser beam parameters	79

LIST OF FIGURES

Figure 3-1 – Gaussian irradiance distribution and desired flattened irradiance distribution	7
Figure 3-2 - FG profiles plotted versus r for various values of N	10
Figure 3-3 - Rescaled FG profiles plotted versus r for various values of N	11
Figure 3-4 - Three dimensional plots of the intensity distribution for $N=4$	15
Figure 3-5 - Three dimensional plots of the intensity distribution for $N=25$	16
Figure 3-6 – Transverse field distributions for $N = 0, 1, 4$ and 9	19
Figure 3-7 – Three dimensional propagation plot for an $N=4$ FGB	19
Figure 3-8 - Three dimensional propagation plot for an $N=25$ FGB.....	20
Figure 3-9 - Beam shaping system diagram.....	20
Figure 3-10 - Symmetrical resonator with Graded Phase Mirrors.....	24
Figure 3-11 - Grade Phase Mirror resonator	25
Figure 3-12 - Resonator of test TEA CO ₂ laser by Bélanger et al. (12)	30
Figure 3-13 - Geometry for rectangular plane mirrors	35
Figure 4-1 – Amplitude of the numerical (black curve) and analytical (grey curve) beam propagation.....	38
Figure 4-2 - Phase of the numerical (black curve) and analytical (grey curve) beam propagation ...	39
Figure 4-3 - FGB intensity at the output coupler	40
Figure 4-4 - FGB phase at the output coupler.....	41
Figure 4-5 - FGB intensity profile at the mirror position	42
Figure 4-6 - FGB phase at the mirror position.....	42
Figure 4-7 - DOE mirror profile	43
Figure 4-8 - Modulated surface profile of the DOE mirror	43
Figure 4-9 – Beam profiles for the case of the introduced FGB and output beam after 5 round trips	45
Figure 4-10 - Phase of the FGB after 5 round trips	45
Figure 4-11 - Density plot of the propagation for the introduced FGB and output beam after 5 round trips.....	46
Figure 4-12 - Starting field of random noise.....	46
Figure 4-13 - Output beam intensity profile after 250 round trips.....	47
Figure 4-14 - Output beam phase after 250 round trips.....	47
Figure 4-15 - Round trip loss plot for the resonator	48

Figure 4-16 - Density plot of the output beam.....	49
Figure 4-17 - Output intensity profiles after 100, 150, 175 and 200 round trips.....	49
Figure 4-18 - Spiricon Pyrocam III.....	52
Figure 4-19 - Imaging of the beam	54
Figure 4-20 - Focus of two beams with different M^2 values.....	55
Figure 4-21 - Beam width measurements in focus area.....	56
Figure 4-22 - Beam size measurement results	58
Figure 5-1 – Multimode laser resonator.....	61
Figure 5-2 – Focused multimode beam size measurements	61
Figure 5-3 - Multimode beam far field image.....	62
Figure 5-4 - Multimode beam image at the output coupler	63
Figure 5-5 – TEM ₀₀ mode laser resonator	64
Figure 5-6 - Focused TEM ₀₀ beam size measurements	64
Figure 5-7 – TEM ₀₀ beam far field image.....	65
Figure 5-8 - TEM ₀₀ beam image at the output coupler	66
Figure 5-9 – FGB mode laser resonator.....	67
Figure 5-10 – Focused FGB beam size measurements	67
Figure 5-11 – FGB far field image.....	68
Figure 5-12 – FGB image at the output coupler	69
Figure 5-13 – FGB mode laser resonator with aperture.....	69
Figure 5-14 - Focused FGB beam size measurements.....	70
Figure 5-15 – FGB far field image.....	71
Figure 5-16 – Multimode paint removal results.....	73
Figure 5-17 – FGB paint removal results.....	74
Figure 5-18 - WH1500 TEA CO ₂ laser and beam delivery system	75
Figure 5-19 - The beam delivery system with the industrial robot arm.....	75
Figure 5-20 - Paint removal system in operation.....	76
Figure 6-1 - Far field images of the multimode beam (left) and TEM ₀₀ beam (right).....	81
Figure 6-2 - Far field images of the open aperture FGB (left) and apertured FGB (right).....	81
Figure 6-3 - Multimode beam (left) and FGB (right) paint removal results.....	82

ANNEXURES

Appendix 8.1 – MATLAB program

ABBREVIATIONS

CW	Continuous Wave
D4 σ	Second Moment
DOE	Diffraction Optic Element
DST	Department of Science and Technology
FD	Fermi Dirac
FG	Flattened Gaussian
FGB	Flattened Gaussian Beam
GPM	Graded Phase Mirror
IF	Innovation Fund
SG	Super Gaussian
SGB	Super Gaussian Beam
SL	Super Lorentzian
TEA	Transversely Excited Atmospheric
TEM	Transverse ElectroMagnetic

1 INTRODUCTION

1.1 Topic introduction

Gaussian beams are frequently encountered in the study and the application of laser beams. Lasers are commonly configured to produce Gaussian beams as their output beam. The propagation and propagation parameters as well as the mathematical description of Gaussian beams are well known and covered in various textbooks regarding lasers. Gaussian beams are useful and applicable in a variety of applications. The most salient property of the Gaussian beam is the fact that it has a Gaussian intensity distribution. This intensity distribution causes the circular Gaussian beam to have a high energy intensity peak in the centre of the beam, with the energy intensity decreasing towards the outer edges of the beam. In some applications this distributed energy intensity is not ideal.

Various laser applications require a laser beam that has a more uniform intensity distribution. This allows one to make better use of all the energy that is present in the laser beam or to make use of the entire volume of an amplifier module if the laser beam is passed through an amplifier. The desired uniform intensity distribution leads one to the study of Flattened Gaussian Beams (FGBs) or Super Gaussian Beams (SGBs). The FGB or SGB can take on various forms and is dependent on the optical system and the design that has been made. For applications where a uniform intensity distribution is required a SGB with a flat top intensity profile can be generated.

The propagation and propagation parameters as well as the mathematics of defining the FGB or SGB are, however, not as straight forward as for the simple Gaussian case. These topics have, however, been covered in various research papers in the past. The method of generation of the FGB or SGB has also been dealt with in many research papers. FGBs or SGBs can be formed by placing beam shaping elements in the beam path to shape the Gaussian laser beam into an FGB or SGB. The resonator of the laser and in particular the optics of the resonator can be designed in such a way that the laser naturally yields an FGB or SGB as the output beam.

1.2 Objectives

The objective of this thesis is to implement a resonator on a Transversely Excited Atmospheric (TEA) CO₂ laser that will make the laser to naturally yield an FGB. The FGB

beam will find its application in the field of coating removal from a substrate using the laser beam. To accomplish this task the theory on FGBs such as their mathematical representation and the modelling of the beam propagation will be studied. Furthermore the concept of laser beam shaping in the laser resonator with graded phase mirrors will be studied. Finally a mirror will be designed, manufactured and tested in the laser resonator and furthermore the beam will be characterised and used in a coating removal application.

1.3 Research problem

A variety of research work has been done in the past on the generation and propagation of the FGB. This includes theory on the generation of the FGB, theory on the propagation of the FGB through free space as well as modelling of the propagation of the FGB. The generation of the FGB within the laser resonator has also been studied.

The research performed in this thesis attempts to study the relevant theory on the topic of FGBs. Furthermore a resonator will be designed and implemented on a TEA CO₂ laser. The generated beam by the laser will be analysed and compared to the theoretical design and predictions. The aim of this thesis is to practically implement a Diffractive Optic Element (DOE) mirror on a laser, to characterise the output beam and to apply the output beam of the laser in a paint removal application where a flat top intensity profile for the beam would be ideal.

1.4 Research questions

The research in this thesis attempts to answer the following questions:

- How will one go about to design a resonator and a graded phase mirror element for implementation in a TEA CO₂ laser?
- What will the beam propagation characteristics for the FGB be and how does this compare to design and modelling predictions?
- How does the beam propagation parameters and pulse energy of the FGB compare to the multimode and Gaussian modes of the laser?
- Is the use of a beam with a flat top intensity distribution better in the application of coating removal from a substrate?

1.5 Restrictions

In the previous paragraphs the desire has been expressed to shape the output beam of a laser using a graded phase mirror or otherwise called DOE mirror in the laser resonator. The profile

that would need to be cut on the mirror to realise this might be very complex. The end design of the DOE mirror must be checked that it is actually possible to manufacture the mirror at an optics manufacturer. The accuracy to which the mirror profile can be machined on the optic is also another possible restriction. The manufacturing capability of the optics manufacturer might pose a possible restriction on what can be done.

1.6 Assumptions

With reference to the already stated restrictions it is, however, assumed that the optics manufacturers will be able to manufacture DOE mirrors for the laser resonator. It is also assumed that the optics can be manufactured to the required accuracy. The manufacturing of graded phase mirrors or DOE mirrors have been attempted by various authors and the assumption is therefore made that these mirrors can be manufactured if the design is reasonable.

1.7 Chapter outline

The study in this thesis will start off by reviewing the current literature that is available on the subjects of FGBs, SGBs, laser beam shaping and laser resonators with internal beam shaping elements.

Following the literature study the background theory will be studied and presented. The background theory will include the study of the mathematical representation of FGBs. This will include the cases of beams with a circular symmetry as well as beams with a rectangular symmetry. The theory of the propagation of these FGBs will also be presented. Furthermore the various techniques for laser beam shaping will be reviewed. Following this the theory on laser resonators and shaping of the laser beam internally in the resonator will also be studied and presented.

The background theory section of the thesis is followed by a discussion of the methodology of the study in this thesis. In that discussion the design of the laser resonator and the graded phase mirror element for the resonator will be treated. The stability of the cavity will be analysed to produce the desired mode using a Fox and Li analysis. The resulting beam from the resonator will be modelled and presented. Subsequently the optic will be manufactured for testing in the laser resonator. Furthermore the methodology of making the beam profile and beam propagation characteristic measurements in the laboratory will be treated.

In succession to this the results of the study will be presented. This will include the practical results measured in the laboratory on the laser where the resonator with the graded phase mirror is implemented. The results will show the beam profile of the laser beam as well as the beam propagation characteristics. The outcome of the coating removal application using the flat top beam will also be presented.

The thesis concludes with discussions on the FGB theory and implementation, the results of the modelled FGB compared with the laboratory measured results, the resonator design using the graded phase mirror element and the application of the flat top beam in laser paint removal. Finally some recommendations for future work are discussed.

2 LITERATURE REVIEW

In this thesis various literature publications were studied and used to arrive at the ultimate goal of implementing an FGB for laser paint removal. Various aspects of lasers and laser beams must be studied to address each aspect that is relevant such as FGBs, the generation of FGBs in custom laser resonators and the measurement of laser beams. The existing literature that was used in this thesis will be reviewed in this section.

Initially the concept of flattened irradiance beams was studied. This topic has been covered by many authors in the past. The most relevant references to this work have been studied and are summarised in Chapter 3. The work of Shealy and Hoffnagle (1) investigated and summarised the various mathematical methods that could be used to describe the profile and propagation of a flattened irradiance profile beam. They investigated the methods of the Super Gaussian (SG), Flattened Gaussian (FG), Fermi Dirac (FD) and Super Lorentzian (SL) for describing a flattened irradiance profile beam. The SG case was also studied by De Silvestri et al. (2). The instance of the FGB was initially studied by Gori (3). This study was also extended by Amarande in References (4) and (5). The work of Gori (3) and Amarande in References (4) and (5) was studied in great detail in the background theory of this thesis. Gori explored the mathematical description of the beam profile and propagation of FGBs for the case of circular symmetry in the beam. The case of rectangular symmetry in the beam was explored by Amarande.

To be able to obtain a flattened irradiance profile beam a suitable beam shaping technique must be employed. The work of Dickey and Holswade (6) on laser beam shaping methods in general was studied. Furthermore the work of Zeitner et al. (7) with regards to laser beam shaping internal and external to the laser resonator was reviewed. In succession to this method of shaping the laser beam internally in the laser resonator using a Graded Phase Mirror (GPM) was studied in great detail. This method was presented by Bélanger et al. in References (8), (9), (10) and also by Leger et al. (11). The physical implementation of GPM mirrors custom resonators was presented further by Bélanger et al. in References (12) and (13). The work of Fox and Li (14) on resonant modes in a maser interferometer was also studied. During the design of the custom laser resonator the work of Mathews (15) and Solms (16) was studied for numerical methods to solve the Kirchoff-Fresnel diffraction integral for the propagation of the beam.

The work of various authors was studied for the purposes of the laser beam characterisation. Rypma presented a general approach to characterising laser beams and making laser beam measurements in (17). The practicalities of measuring laser beam propagation were also presented by Roundy (18), Spiricon Inc. (19), (20), Forbes (21) and the International Organisation for Standardisation (22).

Throughout the text general References such as Siegman (23) and Svelto (24) were also used as a required. The main significant References have been covered in this overview. There are, however, References that contributed to a lesser extent and they will be mentioned in the manuscript where necessary.

3 BACKGROUND THEORY

3.1 Flattened irradiance profile beams

In the application of a laser beam in real life it is often desired to have a laser beam with a flattened irradiance profile as opposed to the distributed irradiance profile in a Gaussian beam. Figure 3-1 shows the Gaussian profile and the desired flattened profile for a laser beam in a laser paint removal application. A flattened irradiance profile beam can be created by the technique of laser beam shaping. Laser beam shaping to produce a flattened irradiance profile can be used in applications such as isotope separation, materials processing, medical applications, lithography, laser printing and laboratory research. In many of these applications it is desired that the target area must be uniformly illuminated with the laser beam, hence the requirement of a flattened irradiance profile. A flattened irradiance profile laser beam is a laser beam of which the irradiance of the beam has a constant value over a fairly large variance in the beam radius. Figure 3-1 illustrates this property in the flattened beam.

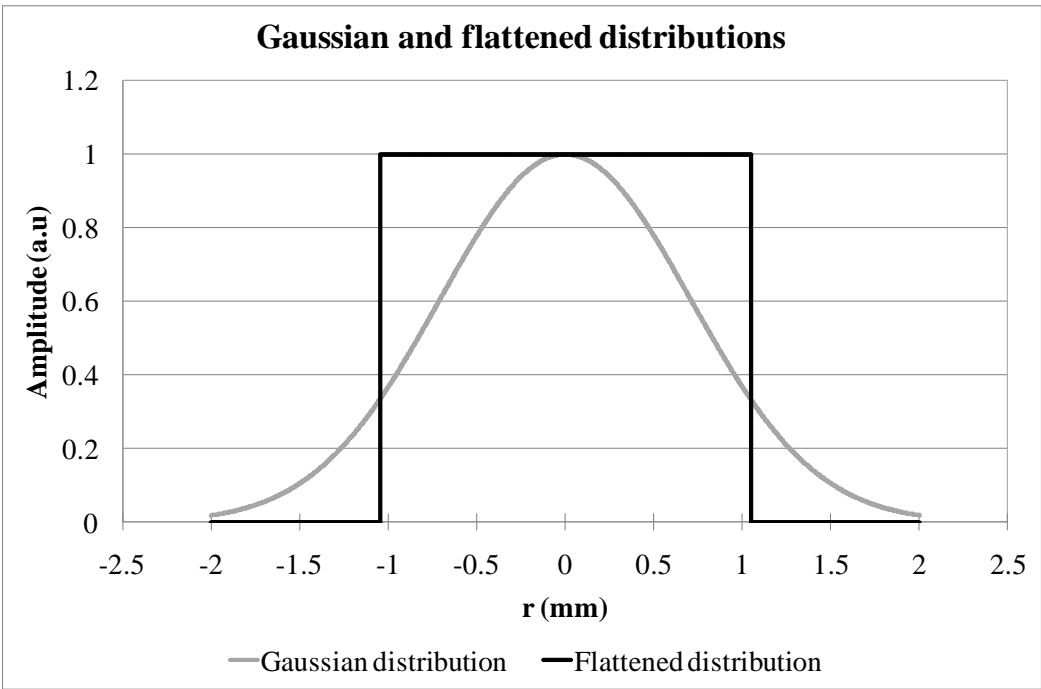


Figure 3-1 – Gaussian irradiance distribution and desired flattened irradiance distribution

Various analytical functions to describe flattened irradiance laser beams have been studied in the past and reported by various authors according to Shealy and Hoffnagle (1). These functions describe a uniform central region in the beam that then makes a transition to a null

region at the outer edges of the laser beam. An SGB has been created by De Silvestri et al. (2) to create the flattened irradiance beam. Further Gori (3) has introduced the FGB with the desired flat top transverse shape. Hoffnagle and Jefferson (25) used the FD distributions for the definition of the flattened beam. The use of the SL was introduced by Li in References (26) and (27). All the above-mentioned functions contain parameters that define the shape and the width of the flattened irradiance beam. The width parameters will influence the beam diameter and the shape parameter has reference to the size of the uniform area and the transition to the null area.

In the work of Shealy et al. (1) they performed a comparative study where a flattened beam was defined through the methods of SGB, FGB, FD and SL. In each case the beam parameters were chosen in such a way that the resulting flattened beam had the same flattened profile as the others. For each method of defining the flattened beam they calculated the effect of diffraction on the propagating beam using Kirchhoff diffraction theory and the Fresnel approximation using the chosen beam parameters. They also proceeded to calculate the M^2 parameter for each of the methods using the chosen beam parameters.

The study of Shealy et al. (1) showed the various analytical methods of defining the flattened beam had little influence on the diffraction calculation. The differences between the results were negligible and if the beams were to be measured in an experimental set-up the differences would be smaller than the experimental error. The Fresnel-Kirchhoff diffraction theory study also showed that if there is a gradual roll-off from the uniform central region of the beam to the null region of the beam it increases the distance over which the beam can be propagated where there will be limited deviation in the uniform irradiance beam.

In conclusion the beam parameters of the flattened irradiance beam must be chosen in such a way that one can get a sufficiently large area of uniform irradiance and still have a gradual transition to the null region to allow for good propagation parameters. The choice of analytical method to define the flattened beam does not make a significant impact on the beam and propagation of the beam.

3.1.1 Flattened Gaussian beams with circular symmetry

There are various analytical ways which were mentioned in the previous section to define a profile with a flattened irradiance profile for a laser beam. In the work of Gori (3), the

Flattened Gaussian (FG) profile is introduced for defining the profile of the flattened irradiance profile beam.

Gori (3) states that the evaluation of the propagated beam that has been defined for example by an SG or other method can be problematic. For a transverse field distribution of a light beam shaped according to some profile, the evaluation of the propagated field in the paraxial approximation in general has to be performed by numerical integration. This results in a non-trivial procedure to determine the effects of a given profile on the propagation. For this reason the FG profile is introduced which resembles a flattened Gaussian whose central region has been flattened. The flattened area of the FG profile is controlled by an integer parameter N . For increasing values of N the FG profile approaches the rectangle function. A laser beam that is axially symmetric of which the radial field profile is FG across a certain plane at $z = 0$ is said to be an FGB. A convenient way to obtain FGBs is by the use of N suitably weighted Laguerre-Gauss beams. This then allows that the field can be evaluated across any plane $z \neq 0$ in an exact and simplistic way using the well known propagation law for Laguerre-Gauss beams.

The FG profile approach by Gori (3) starts from a circularly symmetric Gaussian function stated in Equation 3-1.

$$F(r) = \exp(-r^2) \quad 3-1$$

The goal is to flatten the shape of the Gaussian profile through the multiplication of a suitable correction function. The limiting case is firstly considered. If the Gaussian profile was to be changed into a constant of one, the correcting factor would be $\exp(r^2)$. This factor can be expanded into a series of powers of r^2 . Hence the formula can be written down as shown in Equation 3-2.

$$F_{\infty}(r) = \exp(-r^2) \sum_{n=0}^{\infty} \frac{r^{2n}}{n!} = 1 \quad 3-2$$

Equation 3-2 expresses the function $F_{\infty}(r)$ as a Gaussian factor multiplied by a power series expansion. If the series is truncated, an approximation of the original function can be obtained. The approximation can be fairly accurate near the origin but will become more inaccurate as one moves away from the origin. The approximating function can be defined as

a function of order N as shown in Equation 3-3. In the limit $N \rightarrow \infty$ we get the function defined in Equation 3-2.

$$F_N(r) = \exp(-r^2) \sum_{n=0}^N \frac{r^{2n}}{n!}, \quad N = 0, 1, \dots \quad 3-3$$

The behaviour of the function F_N as a function of r can now be examined. The functions $\exp(-r^2)(r^{2n})/(n!)$ which are summed in the summation are non-negative and tend to zero as $r \rightarrow \infty$. It can therefore be expected that $F_N(r)$ will be close to one for a specific interval and with a smooth transition to zero with increasing r . This is shown in Figure 3-2 where a few curves of the function $F_N(r)$ are plotted for a few values of the parameter N .

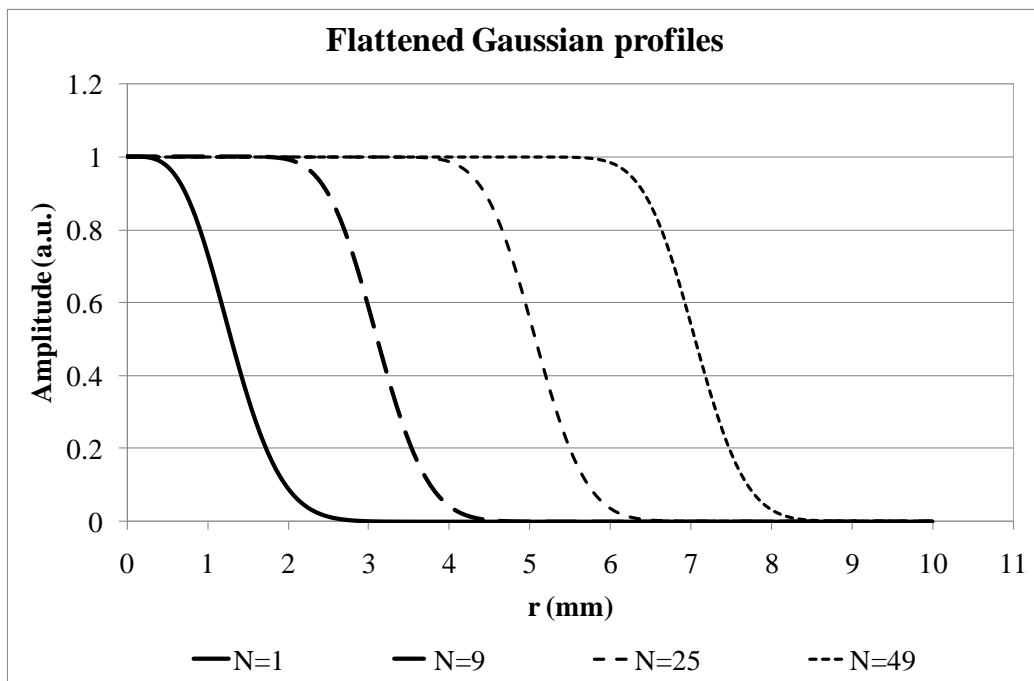


Figure 3-2 - FG profiles plotted versus r for various values of N

The defined function F_N can now be used to approximate the function $\text{rect}(r-0.5)$. This can be achieved by rescaling the function $F_N(r)$ with another factor. To be able to find the scaling factor an estimate of the width of the function F_N is required. It can be shown that the function $\exp(-r^2)$ has a maximum value at the point $r = \sqrt{n}$. Because of the fact that the outermost contribution to the sum in Equation 3-3 comes from the N^{th} term it can be estimated that the width of F_N is \sqrt{N} . The rescaled function can then be redefined as in Equation 3-4.

$$G_N(r) = \exp(-Nr^2) \sum_{n=0}^N \frac{N^n r^{2n}}{n!}, \quad N = 1, 2, \dots \quad 3-4$$

In Equation 3-4 the instance where $N=0$, which in the case of Equation 3-3 yields the pure Gaussian profile, has been excluded. The function $G_N(r)$ can now be plotted for a few values of N and this is shown in Figure 3-3. From the figure one can see that the function $G_N(r)$ approaches the $rect(r-0.5)$ function for increasing N . Both Equation 3-3 and Equation 3-4 can be used to describe FG profiles.

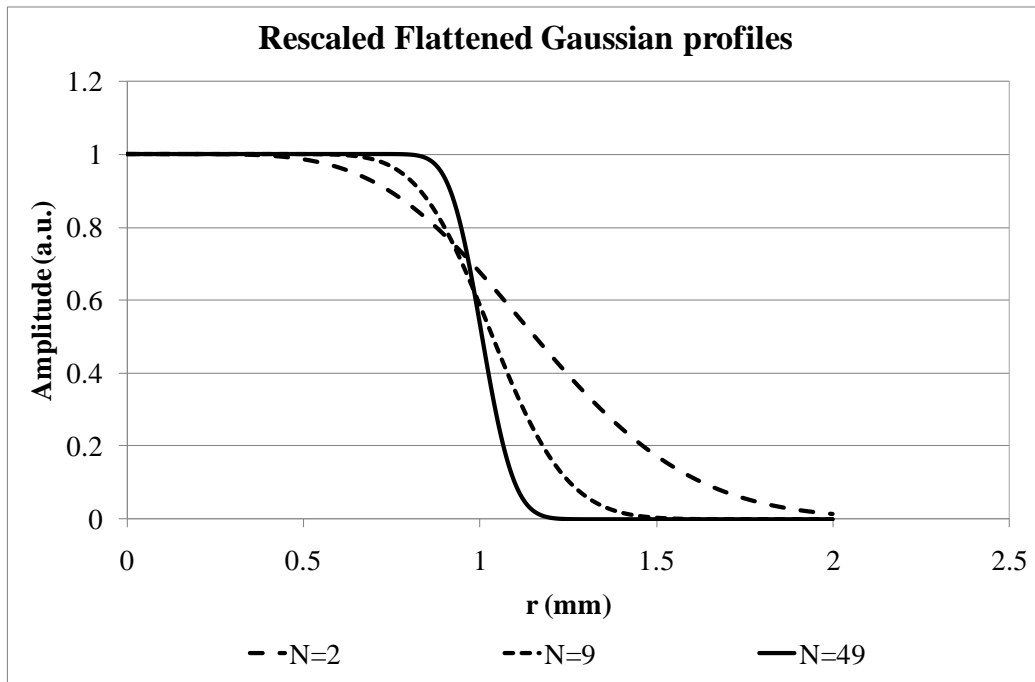


Figure 3-3 - Rescaled FG profiles plotted versus r for various values of N

3.1.2 Propagation of Flattened Gaussian beams with circular symmetry

Gori (3) continues to develop the concept by studying the FGB and the propagation of the FGB. This is done by assuming circular symmetry for the beam and introducing the Laguerre-Gauss beams and viewing the FGB as a superposition of the Laguerre-Gauss beams.

An FGB of order N is a beam of which the radial distribution at the plane $z=0$ is shaped according to the N^{th} FG profile as defined in Equation 3-3 and Equation 3-4. To be able to compare the FGB with the conventional Gaussian beam it would be useful to introduce the spot size parameter w_0 . The field distribution as written in Equation 3-3 can now be rewritten at $z=0$ to include the spot size parameter and is shown in Equation 3-5.

$$V_N(r, 0) = A \exp\left(\frac{-r^2}{w_0^2}\right) \sum_{m=0}^N \frac{1}{m!} \left(\frac{r}{w_0}\right)^{2m}, \quad N = 0, 1, \dots \quad 3-5$$

A constant, A , has also been introduced to the equation. In the special case of $N=0$ the equation yields the distribution of the conventional TEM₀₀ beam with a spot size of w_0 . From paragraph 3.1.1 and Figure 3-2 it is evident that the effective width of the beam increases as the value of the N parameter increases. It would be more ideal if the width of a beam would remain almost constant with only the flatness of the profile changing as an appropriate parameter is varied. If Equation 3-4 is used and similarly the parameters for the spot size are introduced this goal could be achieved. Equation 3-6 then shows the introduction of the parameters into Equation 3-4.

$$U_N(r, 0) = A \exp\left(\frac{-Nr^2}{w_0^2}\right) \sum_{m=0}^N \frac{1}{m!} \left(\frac{Nr^2}{w_0^2}\right)^m, \quad N = 1, 2, \dots \quad 3-6$$

Both of the newly introduced Equation 3-5 and Equation 3-6 can now be used to describe an FGB. Equation 3-5 includes the special instance of $N=0$ for the ordinary Gaussian beam. Equation 3-6 excludes this case and only refers to $N>0$. For this thesis the interest is primarily in beams with a flattened irradiance profile and Equation 3-6 will be best suited for this.

The representation of a laser beam with a flattened profile by the FGB method presents an important advantage. The propagation of the FGB can be studied in a simplistic manner tracing the FGB back to a finite superposition of Laguerre-Gauss beams. Due to the fact that Laguerre-Gauss functions depend on two polar coordinates and this section is concerned with circularly symmetric beams the Laguerre-Gauss functions can be applied here.

To derive this, the formula from Gori (3) which is shown here in Equation 3-7 can be used.

$$x^{2m} = \frac{m!}{2^m} \sum_{n=0}^m (-1)^n \binom{m}{n} L_n(2x^2), \quad m = 0, 1, \dots \quad 3-7$$

The term $\binom{m}{n}$ denotes a binomial coefficient and L_n is the n^{th} Laguerre polynomial. Equation 3-7 can now be inserted into Equation 3-6 which yields Equation 3-8.

$$U_N(r, 0) = A \exp\left(\frac{-Nr^2}{w_0^2}\right) \sum_{m=0}^N \frac{1}{2^m} \sum_{n=0}^m (-1)^n \times \binom{m}{n} L_n\left(\frac{2Nr^2}{w_0^2}\right), \quad 3-8$$

$$N = 1, 2, \dots$$

The terms in the double sum can be rearranged and written as in Equation 3-9 with the new variable c_n defined in Equation 3-10.

$$U_N(r, 0) = A \sum_{n=0}^N c_n L_n\left(\frac{2Nr^2}{w_0^2}\right) \exp\left(\frac{-Nr^2}{w_0^2}\right), \quad N = 1, 2, \dots \quad 3-9$$

$$c_n = (-1)^n \sum_{m=n}^N \binom{m}{n} \frac{1}{2^m}, \quad N = 1, 2, \dots \quad 3-10$$

The circularly symmetric Laguerre-Gauss beam of order h , $\psi_h(r, z)$, has the spatial distribution shown in Equation 3-11 according to Gori (3).

$$\psi_h(r, z) = \sqrt{\frac{2}{\pi}} \frac{1}{W(z)} \exp\{i[kz - (2h + 1)\phi(z)]\} \times L_h\left(\frac{2r^2}{W^2(z)}\right) \exp\left[\left(\frac{ik}{2R(z)} - \frac{1}{W^2(z)}\right)r^2\right] \quad 3-11$$

In Equation 3-11 k is the wave number $\left(\frac{2\pi}{\lambda}\right)$ with λ the wavelength. The Rayleigh distance is defined by Equation 3-12 where W_0 denotes the spot size at the waist of the beam. The parameters $W(z)$, $R(z)$ and $\Phi(z)$ depend on z and are defined in Equation 3-13, Equation 3-14 and Equation 3-15.

$$z_R = kW_0^2/2 \quad 3-12$$

$$W(z) = W_0 \sqrt{1 + \left(\frac{z}{z_R}\right)^2} \quad 3-13$$

$$R(z) = z + \frac{z_R^2}{z} \quad 3-14$$

$$\phi(z) = \tan^{-1}\left(\frac{z}{z_R}\right) \quad 3-15$$

From Equation 3-11 the ψ_n 's are orthonormal in the sense that for two typical indices n and m we obtain Equation 3-16 where the asterisk in the equation shows the complex conjugate and δ_{nm} is the Kronecker symbol where $\delta_{nm}=1$ for $n=m$ and otherwise $\delta_{nm}=0$.

$$\int_0^{2x} \int_0^\infty \psi_n(r, z) \psi_m^*(r, z) r dr dz = \delta_{nm} \quad 3-16$$

By comparing Equation 3-9 and Equation 3-11 it can be seen that the field distribution produced at the plane $z=0$ by a FGB of order N is a superposition of N circularly symmetric Laguerre-Gauss beams taken at the waist of the beams which have a spot size as defined in Equation 3-17.

$$W_{0N} = \frac{w_0}{\sqrt{N}} \quad 3-17$$

In order to find the propagated field at any distance z , one has to replace the waist expression of the Laguerre-Gauss beams with their expression at $z \neq 0$ using the Equation 3-11. Doing this yields the Equation 3-18 where the parameters $W_N(z)$, $R_N(z)$ and $\Phi_N(z)$ can be obtained from Equation 3-12, Equation 3-13, Equation 3-14 and Equation 3-15 once the parameter W_0 is replaced with the parameter W_{0N} that is given by Equation 3-17.

$$U_N(r, z) = A \frac{W_{0N}}{W_N(z)} \exp\{i[kz - \phi_N(z)]\} \times \exp\left[\left(\frac{ik}{2R_N(z)} - \frac{1}{W_N^2(z)}\right)r^2\right] \times \sum_{n=0}^N c_n L_n\left(\frac{2r^2}{W_N^2(z)}\right) \exp[-2in\Phi_N(z)] \quad 3-18$$

The results that have been obtained can now be used in an example. The following values are assumed for some of the parameters that characterise the FGB: $w_0 = 1\text{mm}$; $\lambda = 628\text{nm}$. By using Equation 3-17 the waist spot size of the Laguerre-Gauss beam to be used can be calculated for any value of N . Equation 3-12, Equation 3-13, Equation 3-14 and Equation 3-15 can then be used to calculate the parameters $W_N(z)$, $R_N(z)$ and $\Phi_N(z)$, for a given value of z , that can then in turn be inserted into Equation 3-18.

For the example two arbitrary values of N are chosen to illustrate the behaviour of FGBs in free space propagation. The result of the case for $N=4$ is shown in Figure 3-4 and for $N=25$ in Figure 3-5. Figure 3-4 and Figure 3-5 show three dimensional plots of the intensity distribution across the diameter of the beam for each beam as the beam propagates through free space. The intensity distribution at various values of z was calculated to be able to plot the three dimensional propagation of the beam.

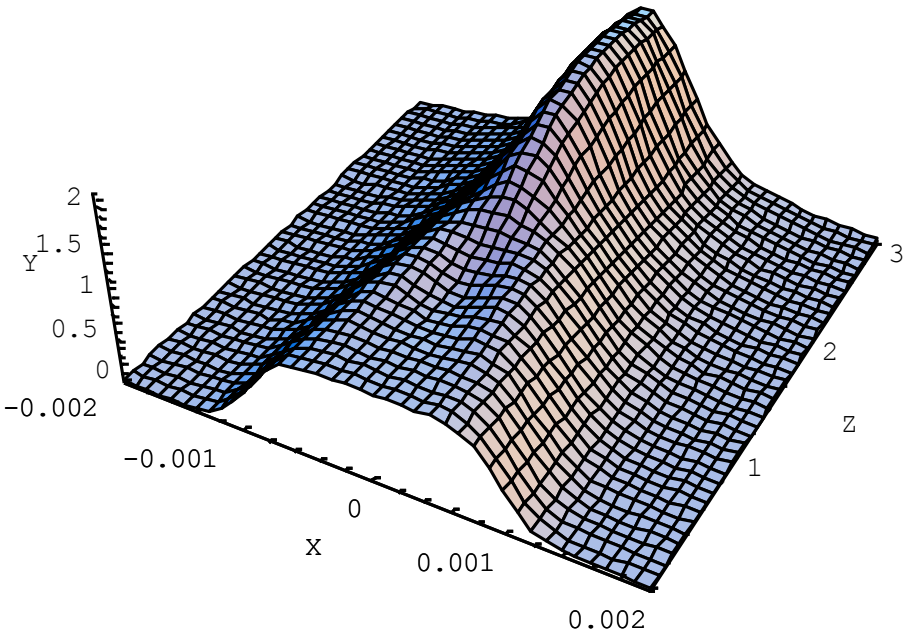


Figure 3-4 - Three dimensional plots of the intensity distribution for $N=4$

In Figure 3-4 and Figure 3-5 the diameter of the beams and the propagation distance is measured in metres. For each curve the maximum value has been normalised to one. For the case of the $N=25$ FGB one can see that the beam is more flattened than for $N=4$ case. By looking at the two plots one can see that there are diffraction rings in the near field of the propagation and that these diffraction rings are more pronounced in the $N=25$ case than in the $N=4$ case. Thus for a beam with a greater flatness the propagation of the beam is not ideal to maintain its shape over a long distance.

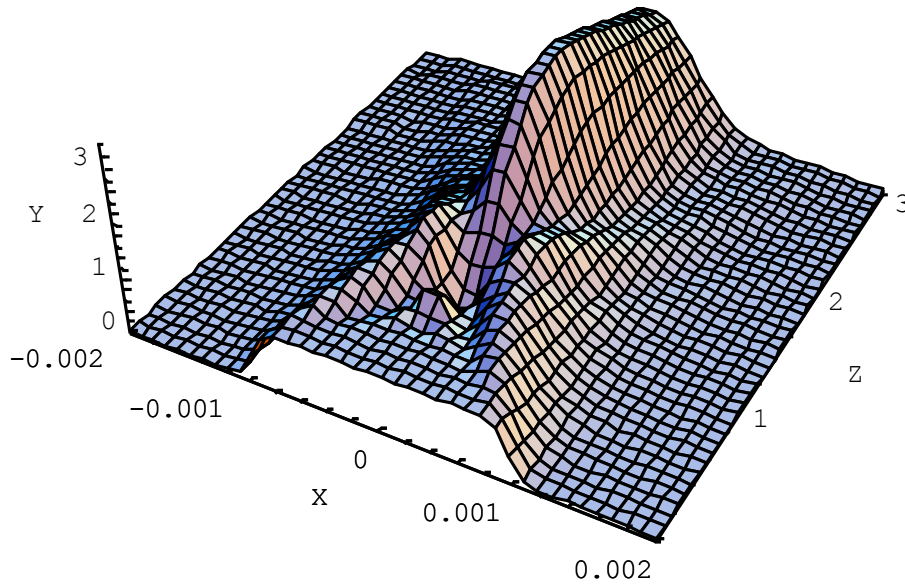


Figure 3-5 - Three dimensional plots of the intensity distribution for $N=25$

3.1.3 Flattened Gaussian beams with rectangular symmetry

Amarande extended the characterisation of the FGB in References (4) and (5), as defined by Gori (3) and shown in this thesis as Equation 3-3. The purpose of extending the characterisation is to introduce the definition of cartesian coordinates to describe the FGB as opposed to the cylindrical coordinates that were used by Gori (3). This is done because there are already existing results about beam characterisation that were performed using cartesian coordinates as opposed to cylindrical coordinates. To introduce the FGB Gori (3) used a superposition of N suitably weighted Laguerre-Gauss beams as described in paragraph 3.1.2 of this thesis. Amarande further presented a procedure for approximating SGBs by FGBs in (5).

In the characterisation of Amarande (4) the geometry was restricted to the bi-dimensional case of (x, z) to simplify matters. By multiplying the two distributions that are flattened independently along the x-axis and y-axis one can readily obtain the three dimensional FGB. The cross section of this FGB will then be a rectangle.

The characterisation of the FGB is started by writing down the field distribution $U_N(x, z)$ at the point where $z = 0$ in the form as shown in Equation 3-19. In Equation 3-19 the parameter A is a constant and the parameter w_0 is the spot size which allows for comparison of the beam with conventional Gaussian beams.

$$U_N(x, 0) = A \exp\left(-\frac{x^2}{w_0^2}\right) \sum_{k=0}^N \frac{\left(\frac{x}{w_0}\right)^{2k}}{k!}, \quad N = 0, 1, \dots \quad 3-19$$

The term x^{2k} can then be expressed as shown in Equation 3-20 by starting from a decomposition relation in Hermite-Gauss functions as shown in Morse and Feshbach (28).

$$x^{2k} = \frac{(2k)!}{2^{3k}} \sum_{n=0}^k \frac{1}{(k-n)!(2n)!} H_{2n}(\sqrt{2}x) \quad 3-20$$

From the equation one can observe that only even Hermite polynomials, H_{2n} , are involved in the function as described in Equation 3-21.

$$U_N(x, 0) = A \exp\left(-\frac{x^2}{w_0^2}\right) \sum_{n=0}^N c'_n H_{2n}\left(\frac{\sqrt{2}x}{w_0}\right), \quad N = 0, 1, \dots \quad 3-21$$

where

$$c'_n = \frac{1}{(2n)!} \sum_{k=n}^N \frac{1}{2^{3k}} \frac{(2k)!}{k!(k-n)!} \quad 3-22$$

According to Siegman (23) the Hermite-Gauss beam of order n , described by $\psi_n(x, z)$, has the spatial distribution as defined in Equation 3-23. The Rayleigh distance is defined by Equation 3-27 where w_0 denotes the spot size at the waist of the beam. The parameters $w(z)$, $R(z)$ and $\Phi(z)$ depend on z and are defined in Equation 3-24, Equation 3-25 and Equation 3-26.

$$\begin{aligned} \psi_n(x, z) = & \left(\frac{2}{\pi w^2(z)}\right)^{\frac{1}{4}} (2^n n!)^{-\frac{1}{2}} H_n\left(\frac{\sqrt{2}x}{w(z)}\right) \\ & \times \exp\left[-\frac{x^2}{w^2(z)} - i\frac{kx^2}{2R(z)} - ikz + i\left(n + \frac{1}{2}\right)\phi(z)\right] \end{aligned} \quad 3-23$$

$$w(z) = w_0 \sqrt{1 + \left(\frac{z}{z_R}\right)^2} \quad 3-24$$

$$R(z) = z + \frac{z_R^2}{z} \quad 3-25$$

$$\phi(z) = \tan^{-1} \left(\frac{z}{z_R} \right) \quad 3-26$$

$$z_R = \frac{\pi w_0^2}{\lambda} \quad 3-27$$

The amplitude at $z=0$ for the FGB represented in cartesian coordinates is shown in Equation 3-28. The propagation formula is then further defined by Equation 3-29 where the term c_n in Equation 3-29 is defined by Equation 3-30.

$$U_N(x, 0) = \sum_{n=0}^N c_n \psi_{2n}(x, 0), \quad N = 0, 1, \dots \quad 3-28$$

$$U_N(x, z) = \sum_{n=0}^N c_n \psi_{2n}(x, z), \quad N = 0, 1, \dots \quad 3-29$$

$$c_n = A \left(\frac{\pi}{2} \right)^{\frac{1}{4}} \frac{2^n}{[(2n)!]^{\frac{1}{2}}} \sum_{k=n}^N \frac{1}{2^{3k} k!} \frac{(2k)!}{(k-n)!} \quad 3-30$$

The graph in Figure 3-6 shows various plots of the field distribution at $z=0$ for selected values of N . The graph in Figure 3-7 shows the propagation of the beam according to Equation 3-29 for the instance where $N=4$ and the graph in Figure 3-8 shows the propagation for the instance of $N=25$.

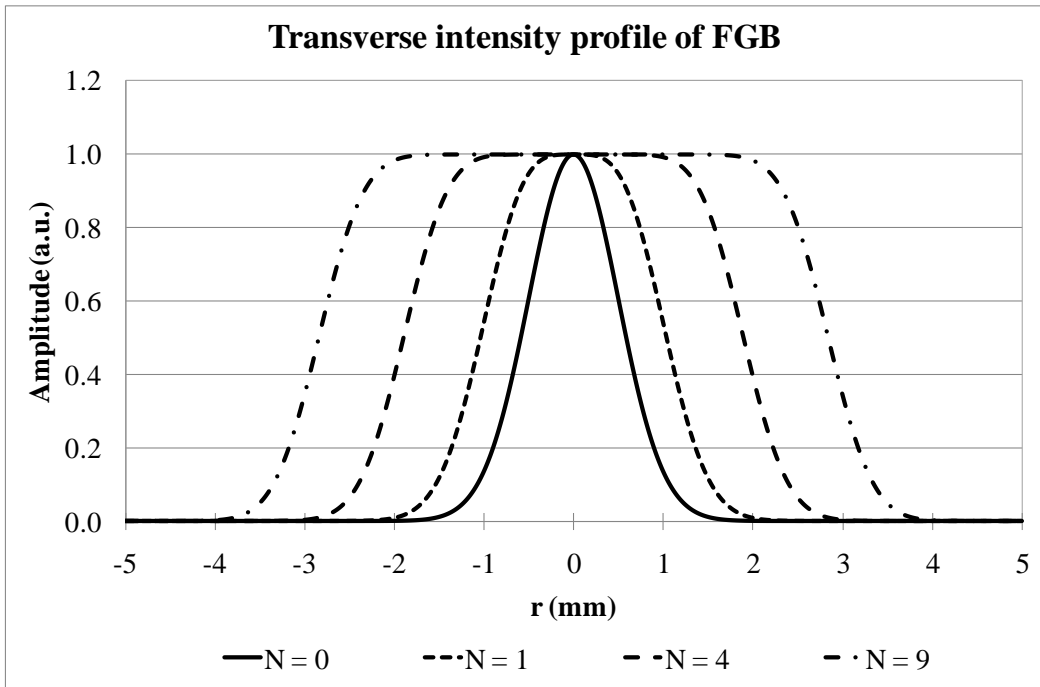


Figure 3-6 – Transverse field distributions for $N = 0, 1, 4$ and 9

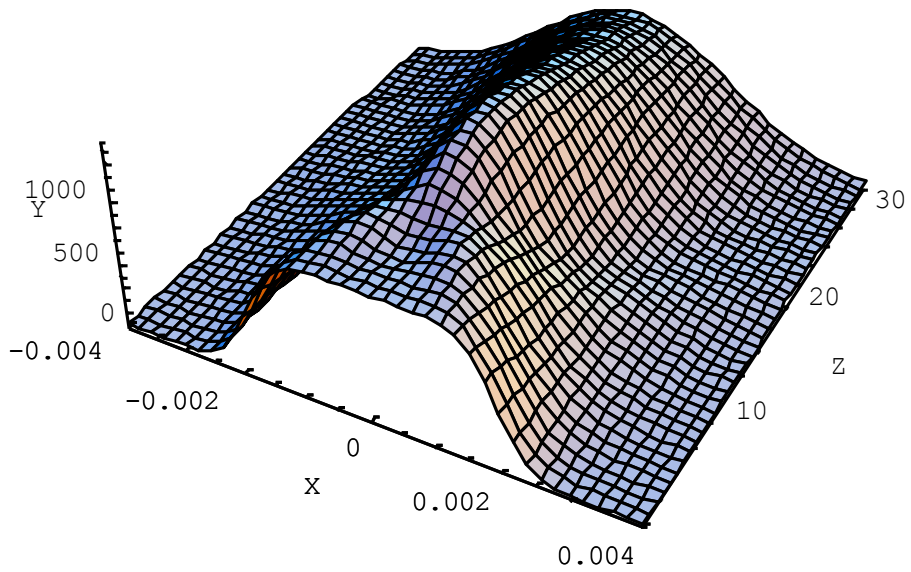


Figure 3-7 – Three dimensional propagation plot for an $N=4$ FGB

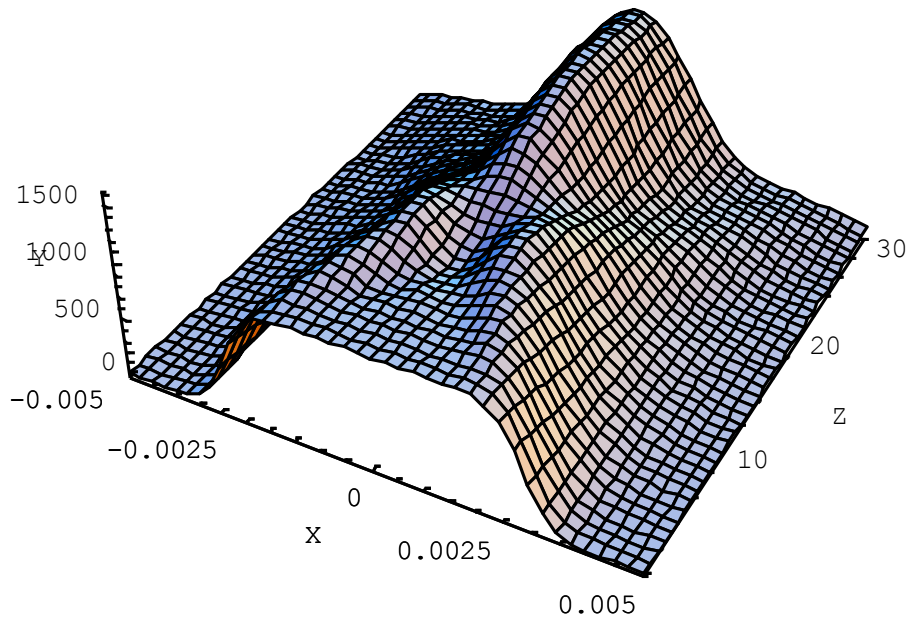


Figure 3-8 - Three dimensional propagation plot for an $N=25$ FGB

3.2 Beam shaping methods

In Section 3.1 the theory on FGBs has been extensively explored and developed. The practical question now remains of how one generates an FGB in a laser or changes the laser beam from a Gaussian beam to an FGB. The study in this thesis will therefore now enter the field of laser beam shaping.

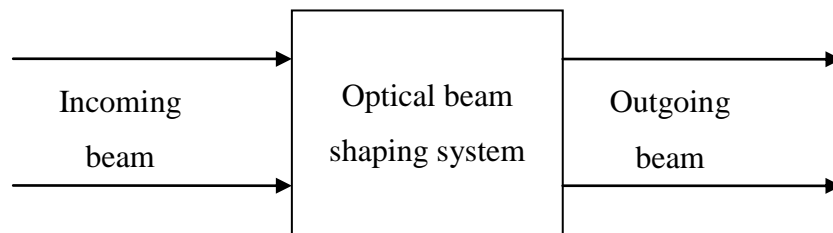


Figure 3-9 - Beam shaping system diagram

Laser beam shaping has been dealt with extensively in past literature. Dickey and Holswade (6) attempted to compile a collective reference work on laser beam shaping and its various aspects. Dickey and Holswade (6) define laser beam shaping as the process whereby the irradiance and phase of a beam is redistributed. The irradiance distribution of the beam

defines the beam shape. They further diagrammatically show a beam shaping system as shown in Figure 3-9. In this scenario the laser beam will enter an optical system and the optical system will transform the beam into another state to generate the desired output beam.

Laser beam shaping techniques can be grouped into two basic types according to Dickey and Holswade (6). The two groups of techniques are field mappers and beam integrators. The technique of field mapping only works with beams for which the field distribution is known. Single mode beams are an example of such beams for which the field distribution is known. This technique is also very sensitive to the alignment of the beam as well as the dimensions of the beam. Beam integrators will work in the scenarios where the field distribution is not known such as multimode beams. Beam integrators will also work for coherent beams. Beam integrators are not as sensitive to the alignment of the beam or to the dimensions of the beam. Interference effects do, however, present problems in beam integrators and specifically for the case of coherent beams. The categorisation of the techniques into field mappers and beam integrators is not coupled to the method that is used to design the beam shaping optics. The methods of design for the beam shaping optics could be either diffraction theory or geometrical optics.

Furthermore there exists various physical ways that beam shaping can be implemented in an optical system. These methods and some of their advantages and disadvantages are summarised by Hoffnagle et al. (25). These methods include: filters with radially varying absorption profiles, refractive methods, reflective methods and diffractive elements such as holograms and binary optics. The use of an absorptive method has the drawback that it has a relatively moderate efficiency, it is sensitive to manufacturing tolerances in the element and is only suitable for low laser power levels. Reflective optics have the drawback that the optics must be used off axis to prevent beam obscuration. This fact leads to complicated asymmetric surfaces that are difficult to manufacture. Reflective optics do, however, have the advantages that they have high efficiency values and can handle high laser power levels. Diffractive elements have the drawbacks that they are inherently wavelength sensitive. Furthermore holograms in general tend to have low efficiency values and paired holograms or phase plates are subject to tight alignment tolerances so that spatial frequency modulation can be avoided. Refractive optics on the other hand have relatively high efficiency and can be implemented in a coaxial optical arrangement which minimises alignment problems.

Laser beam shaping can be applied in two ways to the laser beam. The beam shaping can either be done externally to the laser resonator or done internally to the laser resonator. The topic of internal and external laser beam shaping is discussed by Zeitner et al. (7). In the case of external laser beam shaping, the Gaussian fundamental mode can be shaped by an external optic element to shape the beam to the required intensity profile. External beam shaping has the advantage that the laser can be used for various tasks by inserting different beam shaping optics in the beam path for the various applications. The beam shaping of the laser beam external to the laser resonator poses some distinct disadvantages. The beam shaping requires an optical system that introduces some amount of light outside the window of interest and therefore reduces the light efficiency. This is generally referred to as stray light. The optical losses in the system are caused by the inherent design requirements of the external beam shaping optic elements. These losses cannot be eliminated, even under ideal optic manufacturing conditions. As proposed by Zeitner et al. (7) the stray light can be eliminated by generating the desired beam profile inside the laser resonator. The beam shaping of the laser beam internal to the laser resonator is also ideal in situations where the laser will only be used in a single dedicated application. Another advantage to shaping the beam internally in the laser resonator is that one could expect the shaped beam to have a higher output power as opposed to shaping the beam externally. The adjustment of the beam shaping optics to the laser beam in the case of external beam shaping is also critical. This is just as critical inside the laser resonator but a good mechanical design for the resonator, for the optics positioning and the optics adjustment will greatly eliminate this problem. Beam shaping internal to the laser resonator has been treated by various authors and will be discussed in the next section.

3.3 Laser beam shaping internal to the laser resonator

Laser beam shaping internal to the laser resonator has been treated in depth by Bélanger and Paré (8) (9) as well as by Leger et al. (11). In these References diffractive optical elements or graded phase mirrors have been used to shape the laser beam internally to the resonator.

Bélanger (10) analysed the propagation of a general optical beam in an optical system. The analysis was performed by generalising the *ABCD* propagation law for an optical system by introducing a generalised complex radius of curvature for the general optical beam. Bélanger proved in the paper that it was possible to define a generalised complex radius of curvature Q for a general optical beam. The generalised complex radius of curvature Q was found to obey the same propagation rule as the complex radius of curvature of a Gaussian beam that is

propagating in the same arbitrary $ABCD$ optical system. Furthermore the real radius of curvature R is related to the mean radius of curvature of the phase front of the generalised optical beam. The real beam size W is further related to the second order moment of the intensity. This generalisation for a general optical beam can be applied to the study of laser beam shaping internal to the laser resonator.

Bélangier and Paré (8) presented a geometrical analysis of resonators with graded-phase mirrors. The analysis used the generalised $ABCD$ propagation law for an optical beam and the results that were obtained in (10). A geometrical analysis was performed on the resonator that is shown in Figure 3-10. The resonator is an empty symmetrical resonator formed by two identical graded phase mirrors. $\Phi_0(x)$ is the difference between a reference plane and the actual reflection surface. The goal was to determine the real beam size and the macroscopic radius of curvature on the mirrors. The symmetry of the resonator implied that the beam waist is located in the middle of the resonator with a certain complex radius of curvature at this point. If the beam is propagated through free-space according to the free-space propagation law the complex radius of curvature in front of the mirror is obtained. The purpose of the graded-phase mirror $\Phi_0(x)$ is then to transform the phase $\Phi_1(x)$ of the incident beam to $\Phi_2(x)$ without changing the amplitude $\Psi_2(x)$ of the reflected beam. This relationship is shown in Equation 3-31.

$$\phi_2(x) = \phi_1(x) - 2\phi_0(x) \quad 3-31$$

From the analysis it is evident that the real beam size is not changed. The analysis does, however, show that the real radius of curvature is changed during the reflection. This change depends on the phase of the mirror $\Phi_0(x)$ and the incoming field distribution $\Psi_1^2(x)$ if the phase mirror is not spherical. It is also shown (8) that in the case of a spherical mirror the real radius of curvature of the reflected beam is independent on the field distribution $\Psi_1^2(x)$ of the incoming beam. Bélangier and Paré then postulated that the use of a graded phase mirror inside the resonator will favour the discrimination of the modes that do not have a field distribution that is similar to $\Psi_1(x)$. This will then potentially result into a resonator that is highly discriminating.

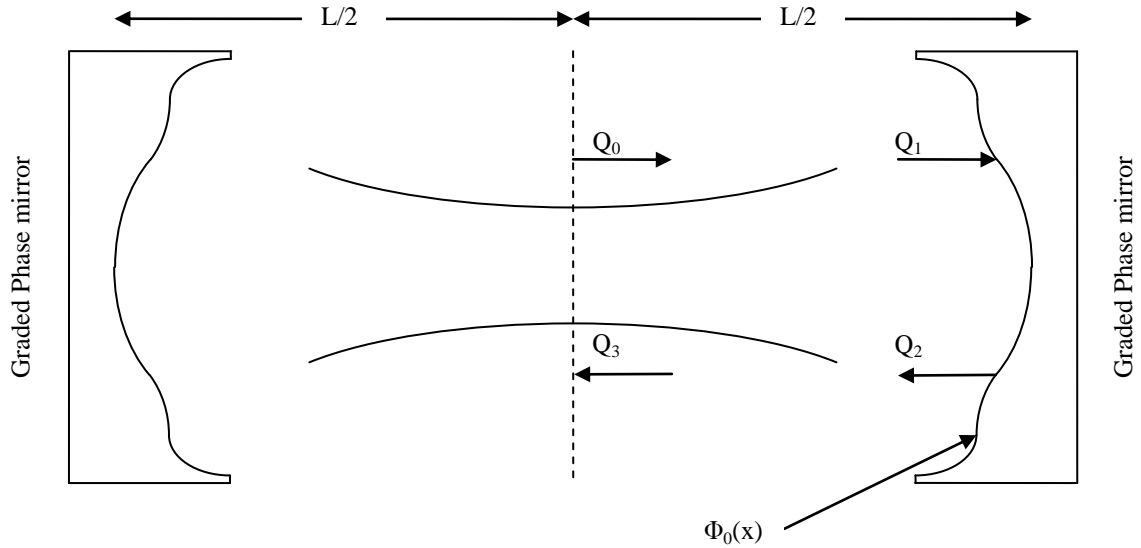


Figure 3-10 - Symmetrical resonator with Graded Phase Mirrors

From Figure 3-10 it can be seen that after reflection from the mirror the complex radius of curvature Q_2 is transformed to the complex radius of curvature Q_3 in the middle of the resonator. For a mode to be an eigenmode of the resonator the beam must reproduce itself within the resonator. Therefore Q_3 must be equal to Q_0 . Bélanger and Paré then further show that for a spherical resonator the spherical mirror matches the wave front of the eigenmode. It is also shown that for the case of the non-spherical mirror the non-spherical mirror matches the wave front of the eigenmode in the resonator. An important result from the paper is shown in Equation 3-32 where the relationship between the phase of the eigenmode $\Phi_1(x)$ and the phase of the mirror $\Phi_0(x)$ is given.

$$\int_{-\infty}^{\infty} x \left(\frac{d\phi_1}{dx} \right) \psi_1^2(x) dx = \int_{-\infty}^{\infty} x \left(\frac{d\phi_0}{dx} \right) \psi_1^2(x) dx \quad 3-32$$

From Equation 3-32 it is evident that the derivatives of the phase are the same or that the phase of the eigenmode is equal to the phase of the mirror apart from a constant, as shown in Equation 3-33.

$$\phi_0(x) = \phi_1(x) - \phi_1(0) \quad 3-33$$

According to Equation 3-31 and Equation 3-33 the incoming beam $u_1(x)$ and the reflected beam $u_2(x)$ are the phase conjugate replicas of each other [$u_2(x) = u_1^*(x)$]. It is then postulated that an optical resonator formed with graded phase mirrors will have an eigenmode with a wave front that matches the phase of each graded phase mirror. The working of the resonator

appears to be similar to a phase conjugate resonator as described in (29). The mirror in the phase conjugate resonator can, however, only phase conjugate a specific beam distribution. The eigenmode that is phase conjugated will have a low loss and will be a stable mode of the resonator. The other eigenmodes of the resonator are potentially not phase conjugated and will be unstable with a high loss. This then gives an indication to the possible large mode discrimination that can be expected in graded phase mirror resonators.

The analysis presented in (8) leads to a methodology to design the graded phase mirror. Firstly the desired eigenmode Ψ_0 of the resonator is specified. For example as shown in Figure 3-11 the distribution at the output coupler is specified. The specified beam at the output coupler is then propagated over the distance $L/2$ to the graded phase mirror using the paraxial diffraction integral. At this point the phase $\Phi_I(x)$ of the beam is extracted from the calculated beam and used to determine the phase of the graded phase mirror according to Equation 3-33.

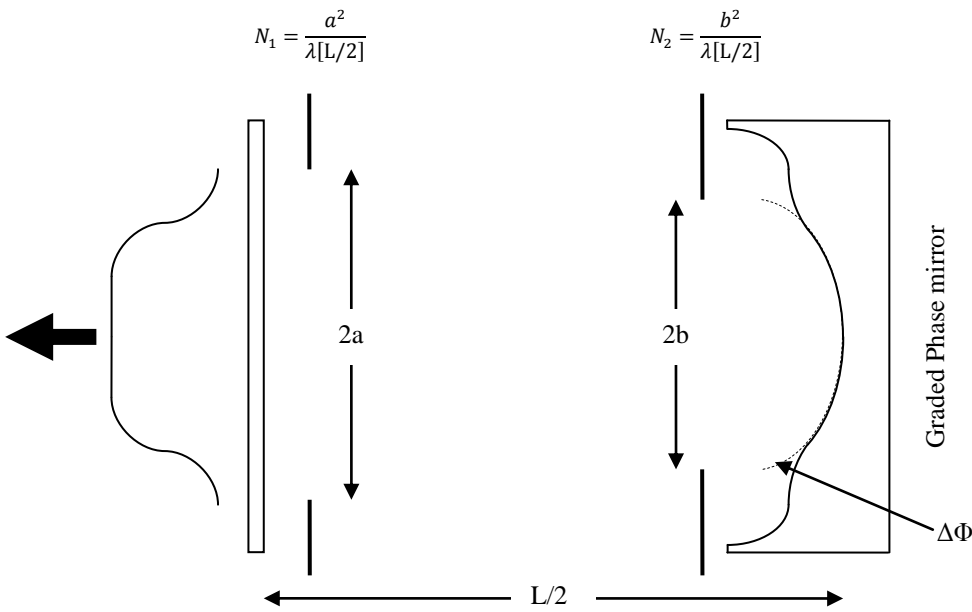


Figure 3-11 - Grade Phase Mirror resonator

Bélanger and Paré further proceeded in (8) to test the concept of the graded phase mirror resonator by performing a Fox and Li (14) analysis on the resonator. This was done by specifying a super-Gaussian distribution at the output coupler and performing the design of the graded phase mirror as described above. The test was performed on a resonator similar to the one in Figure 3-11. The centre of the mirror approaches the profile of a spherical mirror while at some distance from the axis the shape of the mirror changes significantly from the

spherical mirror shape. From Figure 3-11 it can be seen that there is an aperture in front of the graded phase mirror in the resonator. If the Fresnel number of the aperture is small enough the resonator will approach the configuration of a semi-confocal resonator. A Fox and Li analysis was performed on the resonator for the first two eigenmodes of the graded phase mirror resonator. During this analysis the Fresnel number of the aperture in front of the graded phase mirror was varied. The analysis showed that for a small Fresnel number the resonator behaved similarly to a spherical mirror resonator. As the size of the aperture is increased the lowest order mode widens rapidly and is transformed to the expected super-Gaussian as the aperture size increases. The eigenvalue of the eigenmode is still similar to that of the semi-confocal resonator which indicates a low loss for the fundamental mode at the large Fresnel number for the aperture. The second mode has an eigenvalue that becomes significantly lower than the corresponding mode in a semi-confocal resonator when the aperture diameter is increased. This then indicates a large loss for this mode in comparison with the similar mode in the semi-confocal resonator case. These results indicate that there is a large discrimination factor for modes in the graded phase mirror resonator with the additional advantage of the larger size of the fundamental mode. This also shows that graded phase mirror resonators might significantly increase the monomode energy extraction of a laser system.

Bélangier and Paré (8) in principle showed that the fundamental mode of a graded phase mirror resonator behaves similar to the eigenmode of a stable resonator. This implies that the wave front of the fundamental mode matches the mirror surface exactly. They proceeded to define a formal design procedure for the graded phase mirror where the integral equation for graded phase mirror resonators is solved (9). The symmetrical resonator as shown in Figure 3-10 is once again used for the design. The function $\Phi_0(x)$ gives the phase profile of the graded phase mirror where $\Phi_0(x)$ is the difference between the reference plane and the graded phase mirror surface. For the purpose of the analysis only a one-dimensional strip resonator is considered. The results can, however, be extended to the two-dimensional case. The integral equation for the resonator is shown in Equation 3-34

$$\gamma\psi(x) = \left(\frac{i}{\lambda L}\right)^{1/2} \int_{-\infty}^{\infty} \psi(s) \cdot \exp\left[-\frac{i2\pi}{\lambda} \left(\frac{(x-s)^2}{2L} - \phi_0(x) - \phi_0(s)\right)\right] ds \quad 3-34$$

In the equation Ψ is the field distribution over the surface of the mirror and γ is the eigenvalue containing information on the fractional loss and the resonance frequency of the cavity. In their preliminary analysis B elanger and Par e (8) showed that under the condition that the real-geometrical parameter $G^2 > 1$, the resonator can have at least one eigenmode that behaves similar to the stable mode of a spherical resonator. They proceeded to show that such a mode is indeed an exact solution to the integral equation (9). At the waist of the beam the eigenmode has a planar wave front and is completely described by a real amplitude function $\Psi_0(x)$ where the complex conjugate for $\Psi_0(x)$ is given by Equation 3-35.

$$\psi_0(x) = \psi_0^*(x) \quad 3-35$$

As shown in Figure 3-10 the graded phase mirrors are located at a distance $(L/2)$ from the beam waist. The complex beam distribution at the distance $(L/2)$ resulting from the beam waist distribution can be calculated using the Kirchoff-Fresnel diffraction integral as shown in Equation 3-36.

$$u(s, L/2) = \left(\frac{2i}{\lambda L}\right)^{1/2} \int_{-\infty}^{\infty} \psi_0(x_0) \cdot \exp\left[-\frac{i2\pi}{\lambda L}(x_0 - s)^2\right] dx_0 \quad 3-36$$

A solution to the diffraction integral (Equation 3-34) can be written as shown in Equation 3-37 where C is a constant. The solution merely implies that the GPM must match the wavefront of the beam that is being propagated, $\Psi_0(x)$.

$$\psi(s) \cdot \exp\left[i\frac{2\pi}{\lambda}\phi_0(s)\right] = Cu^*(s, L/2) \quad 3-37$$

This can be demonstrated by inserting Equation 3-37 into Equation 3-34 as shown in Equation 3-38.

$$\begin{aligned} \gamma\psi(s) = & \left(\frac{\sqrt{2}}{\lambda L}\right) C \exp\left[\frac{i2\pi}{\lambda}\phi_0(x)\right] \int_{-\infty}^{\infty} \int_{-\infty}^{\infty} \psi_0(x_0) \\ & \cdot \exp\left[-\frac{i\pi}{\lambda L}((x - s)^2 - 2(x_0 - s)^2)\right] dx_0 ds \end{aligned} \quad 3-38$$

By integrating over the variable "s" in the equation the result that is shown in Equation 3-39 can be obtained. The result can also be written in the form as shown in Equation 3-40.

$$\gamma\psi(s) = C \left(\frac{2i}{\lambda L}\right)^{1/2} \exp\left[\frac{i2\pi}{\lambda}\phi_0(x)\right] \int_{-\infty}^{\infty} \psi_0(x_0) \cdot \exp\left[-\frac{i2\pi}{\lambda L}((x_0 - x)^2)\right] dx_0 \quad 3-39$$

$$\gamma\psi(s) = C \exp\left[\frac{i2\pi}{\lambda}\phi_0(x)\right] u(x, L/2) \quad 3-40$$

From the result in Equation 3-37 and the result of the integral equation in Equation 3-40 it is concluded that $\Psi(x)$ is real and hence $\Psi^*(x) = \Psi(x)$. This implies that the wavefront of the eigenmode at this plane matches the GPM. It can also be concluded that $\gamma = C/C^*$ and this can also be written as a pure phase factor $\gamma = e^{i\alpha}$ so that $|\gamma| = 1$. This all implies that the eigenmode is of a stable type and that it has no loss. From Equation 3-37 the mode distribution on the mirror is as shown in Equation 3-41.

$$\psi(x) = |C| |u(x, L/2)| \quad 3-41$$

Furthermore the phase profile of the mirror can be related to the phase of $u^*(x, L/2)$ as shown in Equation 3-42.

$$\frac{2\pi}{\lambda}\phi_0(x) = \text{phase}[u^*(x, L/2)] \quad 3-42$$

Equation 3-42 is the main result of Reference (9). The equation provides a direct method for the design of GPMs. For the practical design of a GPM the resonator as shown in Figure 3-11 can be considered where the output coupler is a plane mirror. Firstly the desired output amplitude distribution $\Psi_0(x)$ is specified. Following this the distribution is propagated over the distance $(L/2)$ using Equation 3-36. At this point the phase of the complex distribution is extracted and the phase profile of the GPM is determined according to Equation 3-42.

In References (8) and (9) the analysis was limited to one transverse dimension only. Paré and Bélanger (30) proceeded to analyse the case for circular geometry as well. Here they present the mathematical model of the custom laser resonator in terms of coupled integral equations. The design is once again performed by specifying the desired output mode for the laser and propagating this over the length of the resonator to the position of the GPM. The profile of the GPM is then made according to the wavefront of the propagated field at that point. A specific super-Gaussian output was then selected and the accompanying resonator and GPM was

designed and analysed. Following this design a diffraction analysis was performed which showed the high modal selectivity of the resonator. The desired fundamental mode could be obtained with an acceptable mirror width and the diffraction losses in the resonator also discriminated against the higher order modes. Sensitivity to various perturbations in the resonator such as thermal lensing, gain saturation and perturbations to the mirror profile were also investigated. Intra-cavity medium perturbations such as thermal lensing and gain saturation will influence the propagation of the beam so that the incident wavefront on the GPM will not be perfectly reversed at reflection on the GPM if these perturbations were not taken into account during the GPM design. Furthermore the physical GPM cannot be manufactured exactly to specified design shape. Small defects in the mirror shape are unavoidable. From the simplistic analysis that was performed it was determined that the influence of these perturbations could be limited and controlled to minimise their impact on the working of the resonator.

3.4 Implementations of laser beam shaping

The theory and design method for custom resonators and GPMs that were developed by Bélanger et al. in References (8), (9) and (10) was taken further when the authors implemented this method on a TEA CO₂ laser in Reference (12). For their TEA CO₂ laser they designed three different resonators where the beams were super-Gaussian beams of orders 2, 4 and 6. For the conventional Gaussian beam the GPM for the super-Gaussian beam of order 2 was a spherical mirror. This resonator was used as the reference in their test and used for comparison to the other two super-Gaussian beam resonators. The test resonator that was used is shown in Figure 3-12. The resonator had an aperture at the GPM and an aperture at the output coupler. The size of the apertures could be varied to test the mode discrimination of the resonator.

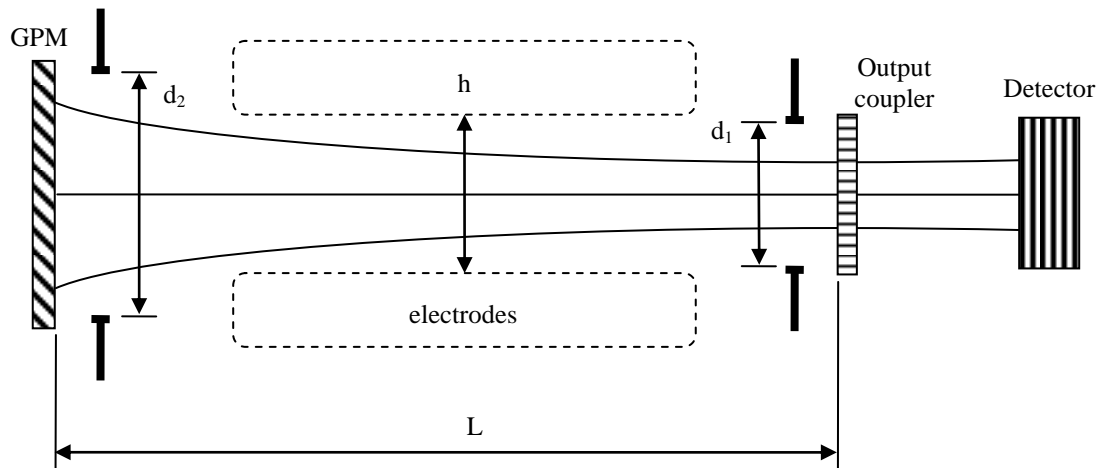


Figure 3-12 - Resonator of test TEA CO₂ laser by Bélanger et al. (12)

Firstly the conventional Gaussian beam resonator was analysed and characterised. An analysis of the eigenvalues of the first eigenmodes of the spherical mirror resonator was performed for increasing values of the aperture d_1 diameter. The results showed how the eigenvalues for each of the modes started at 0 and increased to 1 as the aperture diameter increased. Following this the output energy of the laser was measured for increasing values of the aperture diameter. The output energy showed an almost linear increase in energy as the aperture diameter was increased. This observation agreed well with the eigenmode analysis that showed how the various modes start to contribute to the output as the aperture diameter increases with no “suppression” of the higher order modes. Burn patterns of the laser beam were also taken for increasing values of the aperture diameter. The results show that the beam has a TEM₀₀ distribution while the diameter is smaller than 9mm. At the diameter of 9mm the TEM₀₁ mode is present and the beam has a doughnut shaped mode. As the aperture increases, higher order modes start to contribute towards the beam making it a multimode beam. At the large aperture diameters the higher order modes are of the Gaussian-Hermite type. This is due to the rectangular geometry of the gain volume and also due to the Brewster windows in their resonator.

Secondly the resonators for the super-Gaussian beam orders of 4 and 6 were analysed and characterised similarly to the conventional Gaussian resonator. Analyses of the eigenvalues of the first eigenmodes of the resonators were performed for increasing values of the aperture d_1 diameter. For the super-Gaussian beams of order 4 and 6 the eigenvalue analysis yielded significantly different results as opposed to the conventional Gaussian beam. The lowest order

mode in the resonators for the super-Gaussian beams of order 4 and 6 behaved similarly to the lowest order mode of the resonator of the conventional Gaussian beam. The higher order eigenvalues were significantly different and exhibited mode crossing that is typical of an unstable resonator according to (23). The eigenvalues of the higher order modes did not converge to 1 for either of the resonators with the higher order super-Gaussian beam. The output energy of the laser was once again measured for increasing values of the aperture diameter. For both of the higher order super-Gaussian beams the laser output energy increased linearly. At an aperture diameter of 8mm the output energy reached a plateau. At this point the higher order super-Gaussian beams were still monomode according to the eigenvalue analysis. In the case of the conventional Gaussian beam the energy kept increasing at this point due to the resonator becoming multimode at this point. For the higher order super-Gaussian beams the output energy reached the energy plateau between the aperture diameters of 8mm and 11mm. For diameters larger than 11mm the output energy increased again. This agreed with the eigenvalue analysis that showed that the next order mode in the resonator reaches a loss of 10% at the aperture diameter of 11mm. At the point of the aperture diameter of 11mm the resonator became multimode. The burn patterns for the higher order super-Gaussian beams also showed monomode results below an aperture diameter of 11mm and multimode results beyond this. This implementation in Reference (12) proved the modal discrimination of the resonators using GPMs on a practical level.

Practical implementations of GPMs in laser resonators were continued by Bélanger et al. in Reference (13). Graded Phase mirrors were implemented in the resonator of a low power Continuous Wave (CW)-CO₂ laser. Due to gain saturation the CW-CO₂ laser behaves differently in terms of modal behaviour and output power. A similar strategy was followed to test the GPM on this laser. GPMs for super-Gaussian beams of orders 2, 4 and 6 were developed for the laser. The first mirror was once again spherical and produced the conventional Gaussian beam which served as a basis for comparison. The output power of the laser was recorded for increasing aperture size for each GPM on the CW-CO₂ laser. Output power for the conventional Gaussian beam increased almost linearly with increasing aperture diameter. In the case of the higher order super-Gaussian beams the output power increased and reached a plateau around an aperture diameter of 8mm and stayed constant for increasing aperture size until approximately 11mm. For aperture values larger than 11mm the output power of the laser increased again. The results showed that the GPMs in the resonator yielded good modal discrimination between fundamental and higher order modes. The results also

showed a significant increase in the monomode output power of the laser for the super-Gaussian beams of order 4 and 6 versus the conventional Gaussian beam power output. The theoretical simulations for the implementation of the GPMs in the CW-CO₂ laser also agreed very well with the measured results.

3.5 Stability analysis

In Reference (14) the authors Fox and Li theoretically investigated the diffraction of electromagnetic waves in Fabry-Perot interferometers while the interferometers were implemented as resonators in optical masers. They employed a numerical method to determine the electromagnetic field across the surface of the mirrors of the interferometer where an arbitrary wave was reflected back and forth between the mirrors. The results showed that after many reflections a steady state was reached where the relative field distribution did not vary from one pass to another through the interferometer. The amplitude of the field also decayed exponentially from the centre to the outer edges of the mirrors. The steady state field distribution that was obtained can be viewed as a normal mode of the interferometer. Within the interferometer there are various normal modes that could exist depending on the initial wave distribution. The lowest order mode in the interferometer has the lowest diffraction losses. This mode also has a high intensity in the middle of the mirror and low intensities at the edges of the mirror. This mode then has a diffraction loss that is much lower than the diffraction loss of a uniform plane wave. In the Reference the field distributions and diffraction losses for various mirror geometries and modes were analysed.

In the instance of an oscillating maser or laser the lowest order mode should dominate in the resonator if the resonator design and mirror spacing is correct. This technique can be employed to theoretically test a resonator design to determine what the lowest order mode in the resonator will be. The following paragraphs will outline the theory behind this resonant mode analysis as outlined by Fox and Li (14).

In a laser resonator a wave departing from one of the mirrors and travelling towards the other mirror will be amplified as it travels through the gain medium of the resonator. While propagating in the resonator the wave will be attenuated due to inhomogeneous regions in the gain medium. At the point where the wave arrives at the second mirror the wave will be further attenuated due to reflection losses and further losses will also occur around the edges of the mirror. For laser oscillation to exist the total attenuation due to density scattering,

diffractive spill over and reflection losses must be less than the amplification that was obtained while the wave propagated through the gain medium. Therefore diffraction losses are expected to be important when determining the start oscillation condition, and also in determining the distribution of energy in the resonator during oscillation. The study of Fox and Li (14) investigated the effects of diffraction on the electromagnetic field within a Fabry-Perot interferometer.

In the analysis the propagating wave which was reflected back and forth between two parallel plane mirrors was considered. An arbitrary initial field distribution at the first mirror was assumed. Following this the field that was produced at the second mirror due to the first pass through the resonator was calculated. The process was then repeated to produce the wave at the first mirror due to the reflection from the second mirror during the second pass in the resonator. This process of calculating the field was repeated for successive passes through the resonator. From performing this analysis it can be determined whether the relative field distribution converges to a steady state value, whether the steady state solution is unique and what losses are associated with these solutions.

The scalar formulation of Huygens' principal was used to compute the electromagnetic field at the one mirror in terms of the integral of the field at the other mirror. The Fresnel field, u_p , caused by an illuminated aperture A is given by the surface integral shown in Equation 3-43.

$$u_p = \frac{j k}{4\pi} \int_A u_a \frac{e^{-j k R}}{R} (1 + \cos\theta) dS \quad 3-43$$

In Equation 3-43 u_a is the aperture field, R is the distance between a point on the aperture and the observation point, θ is the angle which R makes with the unit normal to the aperture and k is the propagation constant of the medium. For the analysis it is assumed that a starting wave distribution of u_p is initiated at one of the mirrors of the resonator. This wave is then allowed to reflect back and forth inside the resonator. After a number of passes q through the resonator the field at a given mirror due to the reflection from the other mirror is given by Equation 3-43 where u_p is replaced by u_{q+1} , which is the field distribution at the mirror under consideration. The variable u_a is replaced by u_q which is the reflected field distribution from the opposite mirror that results into the field distribution u_{q+1} .

It is plausible that after many passes in the resonator the field distribution at the mirrors will not change significantly from reflection to reflection and hence converge to a steady state solution. In the steady state the field distribution on the mirrors are identical apart from a complex constant as shown in Equation 3-44. In Equation 3-44 the variable v is a distribution function which does not change from reflection to reflection. The variable γ is a complex constant that is independent of the position coordinates.

$$u_q = \left(\frac{1}{\gamma}\right)^q v \quad 3-44$$

Equation 3-44 can now be inserted into the Equation 3-43 so that the integral equation can be simplified to the Equation 3-45 with the variable K defined in Equation 3-46.

$$u_p = \gamma \int_A K v dS \quad 3-45$$

$$K = \left(\frac{j k}{4\pi R}\right) (1 + \cos\theta) e^{-j k R} \quad 3-46$$

The distribution function v , which satisfies Equation 3-45 can be viewed as a normal mode of the resonator defined at the surface of a mirror. The logarithm of the variable γ quantifies the losses and the phase shift that the wave experiences during each pass in the resonator. This value can be considered to be a propagation constant that is associated with the normal mode. The integral Equation 3-45 can now be solved using a numerical method that successively approximates the equation. This numerical method of solution is analogous to the real process of launching an initial field distribution and letting it propagate back and forth between the mirrors.

In their study, Fox and Li calculated numerical solutions for various geometric configurations of the interferometer. They specifically studied the case of rectangular plane mirrors, circular plane mirrors and confocal spherical or paraboloidal mirrors. For the implementation of the GPM in a custom resonator, the resonator will consist of a circular plane mirror that will form the output coupler and the GPM that will contain the special surface. The custom resonator is therefore a combination of a plane mirror and a paraboloidal mirror. During the numerical implementation in (14), where the spherical or paraboloidal mirrors were discussed, a generalised approach for solving the problem was devised. A method to solve the problem for

implementations that involve mirrors with an arbitrary curvature was devised. In the adapted method the field at each mirror was computed using the equation for the circular plane mirrors. At each mirror a phase distribution matching the curvature of the mirror was added to the field before it was used in the following pass through the resonator. As mentioned in Section 3.3 and in Reference (9) a one dimensional strip resonator was considered in the design. Due to this fact the rectangular plane mirror solution for infinite strip mirrors as outlined in (14) was implemented. A similar approach can be taken to introduce a mirror with an arbitrary curvature. In the implementation, the field at each mirror can be computed using the equation for the rectangular plane mirrors. At each mirror a phase distribution matching the curvature of the mirror will be added to the field before it is used in the following pass. This method will be used to introduce the GPM in the resonator.

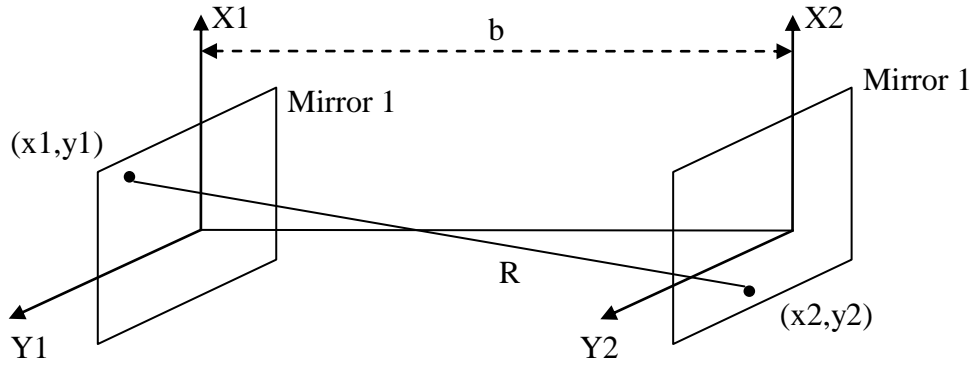


Figure 3-13 - Geometry for rectangular plane mirrors

The theory for the case of rectangular plane mirrors will be discussed here briefly. The geometry for the case of the rectangular plane mirrors is shown in Figure 3-13. It is shown in Reference (14) that the solutions to the integral equation for rectangular plane mirrors as shown in Figure 3-13 can be given by Equations 3-47 and 3-48.

$$u_{q+1}(x_2) = \frac{e^{j(\pi/4)}}{2\sqrt{\lambda}} \int_{-a}^a u_q(x_1) \frac{e^{-jk\rho}}{\sqrt{\rho}} \left(1 + \frac{b}{\rho}\right) dx_1 \quad 3-47$$

$$\rho = \sqrt{b^2 + (x_1 - x_2)^2} \quad 3-48$$

4 METHODOLOGY

4.1 Design of the laser resonator with internal beam shaping

In Chapter 3 significant attention was given to studying the fundamentals of FGBs and the shaping of the laser beam internal to the laser resonator. The theory on FG profiles and the propagation as an FGB was studied and presented. The generation of SGBs in custom laser resonators was also studied and presented. In this section the background theory is used and implemented in a design for a custom laser resonator. It is desired to have a laser resonator that naturally yields an FGB. The FGB is desired for the previously mentioned application, laser based paint removal.

The method to design a custom laser resonator implementing a DOE as presented by Bélanger and Paré in (8) and (9), and also presented in Section 3.3 will be used to design a custom resonator for the application in this section. The steps of designing a custom laser resonator according to (8) and (9) can be summarised as follows:

1. Specify the profile of the laser beam that is desired at the output coupler of the resonator. This is also referred to as the eigenmode, Ψ_0 , of the resonator.
2. The chosen profile is then propagated along the length of the resonator up to the position of the mirror using the Kirchhoff-Fresnel diffraction integral.
3. At the position of the mirror the phase, $\Phi_I(x)$, of the beam is extracted.
4. The phase of the beam, $\Phi_I(x)$, can then be related to the phase profile of the mirror through Equation 3-42. The phase profile of the mirror is then determined and the mirror can be manufactured according to this design.

In the second step of the design procedure the beam is propagated using the Kirchhoff-Fresnel diffraction integral. In Section 4.1.1 the propagation of an FGB using an analytical method is studied and the results presented. Following this the resonator design and DOE design are performed in Section 4.1.2. The stability of the eigenmode in the resonator is analysed in Section 4.1.3.

4.1.1 Propagating the FGB

The propagation of the FGB with circular symmetry was presented in Section 3.1.2 as summarised from Reference (3). Gori (3) propagated the FGB by tracing the FGB back to a finite superposition of Laguerre-Gauss beams. This method of propagating the FGB can be

viewed as an analytical method to propagate the beam. The same principle was extended by Amarande (4), (5) for approximating the propagation of an FGB with rectangular symmetry. In the rectangular symmetry case the FGB was traced back to a finite superposition of Hermite-Gauss beams. For the purpose of this study the beam will be restricted to circular symmetry.

The design procedure as outlined by Bélanger and Paré requires propagating the beam using the Kirchhoff-Fresnel diffraction integral as given in Equation 3-36. The field to be propagated, $\Psi_0(x_0)$, must be specified and inserted into the equation. The beam can then be calculated at any given distance using the equation. To solve the Kirchhoff-Fresnel diffraction integral it will be necessary to use a numerical integration method. The Trapezium rule numerical integration method as outlined in References (15) and (16) was chosen for the numerical solution of the Kirchhoff-Fresnel diffraction integral. The numerical implementation was done using MATLAB[®].

To test the results of the numerical propagation method it was compared to the results of the analytical propagation method. The FGB of order $N=25$ as shown by Gori in (3) and also in Figure 3-5 was chosen as the basis for the comparison. The same FG was propagated using the numerical method. The results of the amplitude of the beam for the numerical and analytical methods are presented in Figure 4-1. The graphs in Figure 4-1 are plotted at various distances along the beam propagation path. For each instance the numerical and analytical results are plotted together for comparison. The result of the numerical method is plotted in a solid black line and the result of the analytical method in a solid grey line.

From the results in Figure 4-1 it can be seen that there is a fair agreement between the numerical and analytical methods but that there are some differences in the beam amplitude. Decreasing the step size and increasing the accuracy in the numerical method to obtain more accurate results did not yield any improvements in the results. It is assumed that the analytical method makes an approximation of the beam propagation through the finite superposition of the Laguerre-Gauss beams. The solution of the numerical method is assumed to be more accurate and is the beam propagation method that will be used in Section 4.1.2 to design the custom resonator together with the DOE mirror.

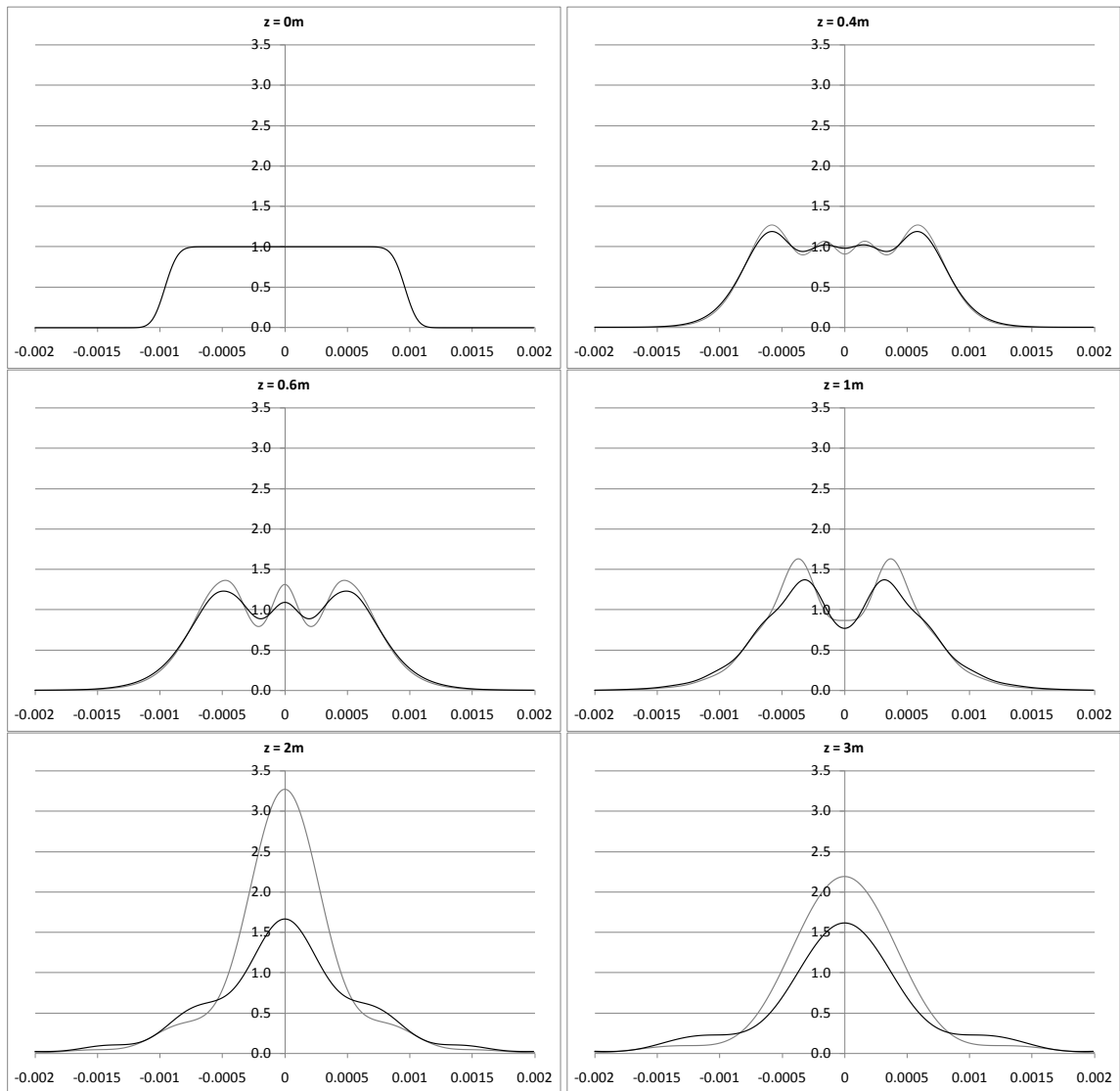


Figure 4-1 – Amplitude of the numerical (black curve) and analytical (grey curve) beam propagation

The results of the phase of the beam for the numerical and analytical methods were also analysed. Figure 4-2 shows the phase of the beam for the numerical and analytical methods. The graphs in Figure 4-2 plot the beam phase numerical and analytical results together at similar distances along the beam propagation path. The difference in phase between numerical and analytical beam propagation is also present as in the case of the amplitude of the beam. The beam phase of the numerical and analytical methods exhibit similar phase profiles, but appear to be inverted with an off set.

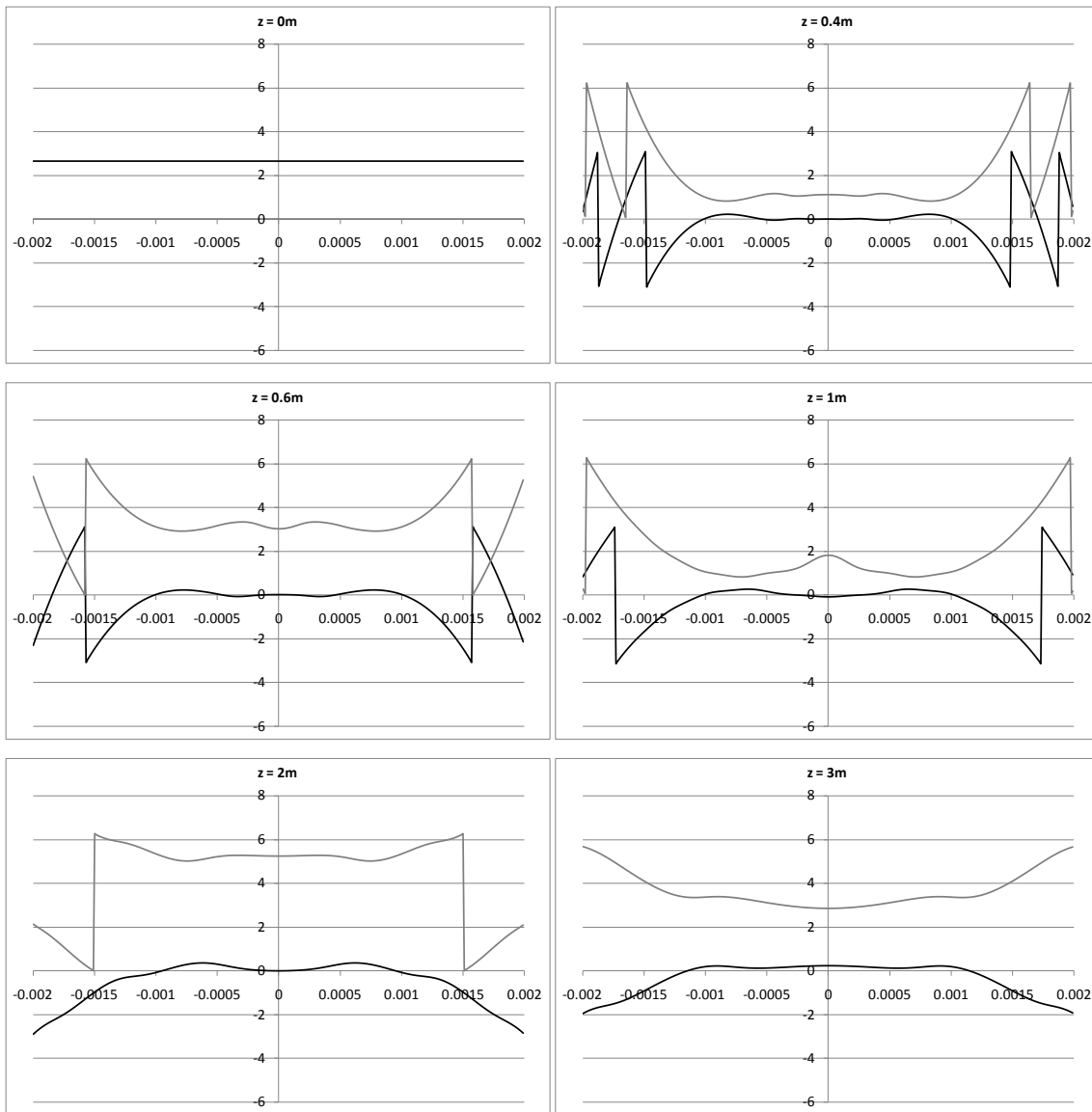


Figure 4-2 - Phase of the numerical (black curve) and analytical (grey curve) beam propagation

4.1.2 Resonator design

The resonator and DOE design for the TEA CO₂ laser was done by Forbes and the design and preliminary results were reported by Du Preez, Forbes and Botha (31). For the implementation of the custom resonator an FGB was chosen as the output of the resonator. Equation 4-1 shows the intensity profile for an SGB. In the equation the parameter x is the radial position in the beam, the parameter w_0 is the beam waist for the SGB and the parameter N is the order parameter of the SGB. The order parameter N adjusts the size of the flat part of the SGB and also the steepness of the edges of the beam. For high values of N the beam intensity profile will approach the flattened distribution as shown in Figure 3-1. For the special case where $N=1$ the intensity profile will be standard Gaussian beam profile. During

the design of the resonator a suitable value for N must be chosen. For a sufficiently large value of N , the SGB in Equation 4-1 approaches an FGB so that $\Psi_{SGB}(x) = \Psi_{FGB}(x)$. It is reported by Forbes (31), (32), (33) that FGBs diverge very rapidly in their intensity during free space propagation. It is therefore imperative to choose the N parameter low enough that the FGB has a fairly good propagation over the length of the cavity with no dramatic change in the beam intensity while on the other hand choosing it high enough so that beam still is an FGB.

$$\psi_{SGB}(x) = A \exp\left(-2\left(\frac{x}{w_0}\right)^{2N}\right) \tag{4-1}$$

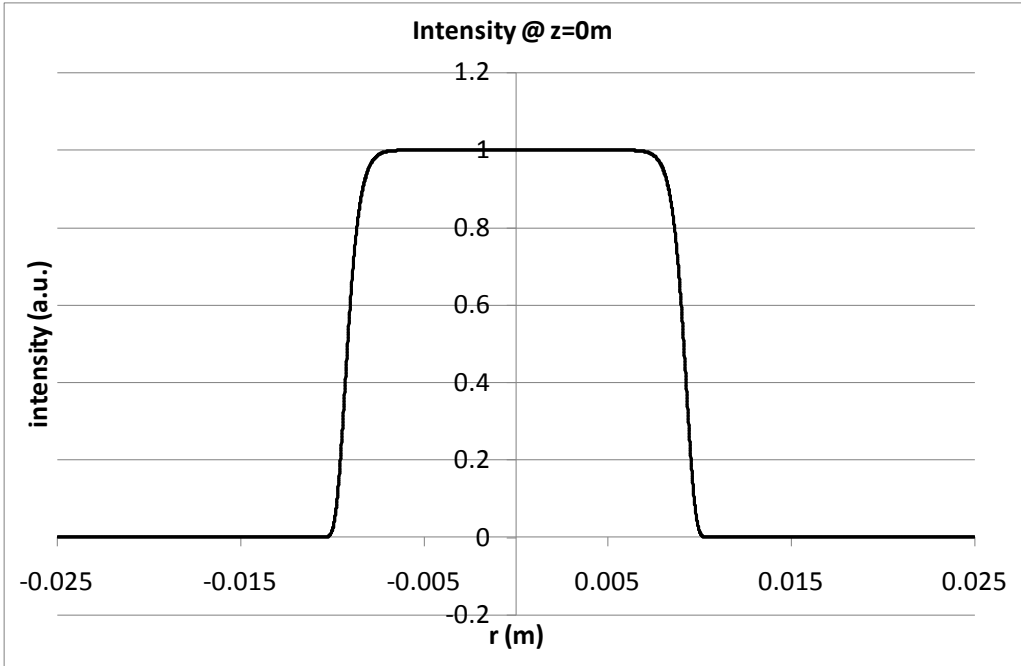


Figure 4-3 - FGB intensity at the output coupler

As previously mentioned the custom resonator with the DOE was implemented on a TEA CO₂ laser. The WH1500 laser used for the implementation of the custom resonator with the DOE was manufactured by SDI Lasers. The WH1500 laser has an average output pulse energy of 5J per pulse and an average output power of 1500W in the multimode beam configuration. The TEA CO₂ laser operates at a wavelength of $\lambda=10.6\mu\text{m}$ and the length of the resonator cavity was 1.772m. To obtain an FGB with a circular symmetry from the resonator the N parameter was chosen to have a value of 10 and the beam waist was specified as $w_0=10\text{mm}$. The graph in Figure 4-3 shows the intensity profile of the FGB that will exit the laser resonator at the output coupler. The phase of the FGB at the output coupler is shown in

Figure 4-4. From the graphs it can be observed that the phase at the output coupler will be flat and the beam will have a flat top intensity profile. This concludes step 1 in the design of the DOE mirror for the custom resonator.

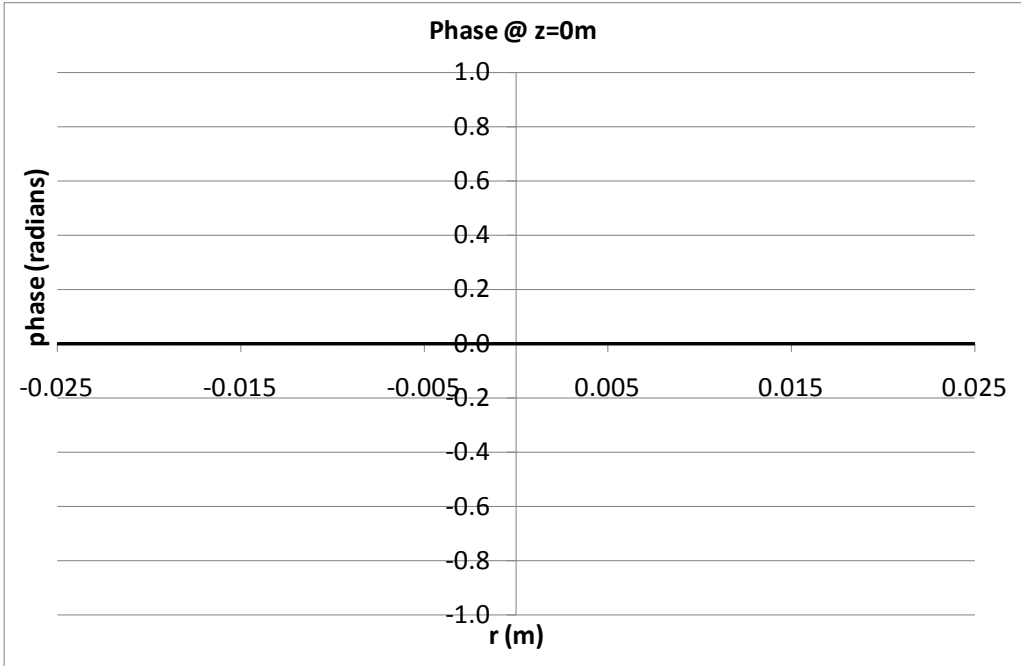


Figure 4-4 - FGB phase at the output coupler

Following this the second step in the design procedure was performed where the above specified FGB was propagated along the length of the resonator up to the position of the mirror. This propagation was performed with a numerical solution to the Kirchhoff-Fresnel diffraction integral as reported in Section 4.1.1. The numerical solution was once again obtained using MATLAB[®]. The graph in Figure 4-5 shows the intensity profile of the FGB and the graph in Figure 4-6 shows the phase of the FGB at the mirror position in the resonator.

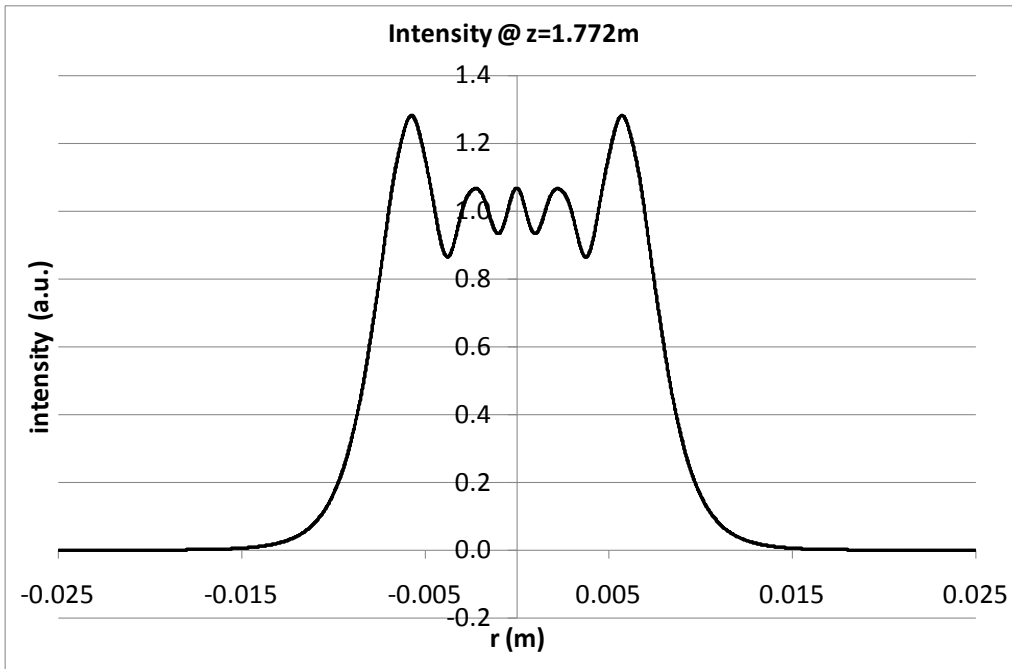


Figure 4-5 - FGB intensity profile at the mirror position

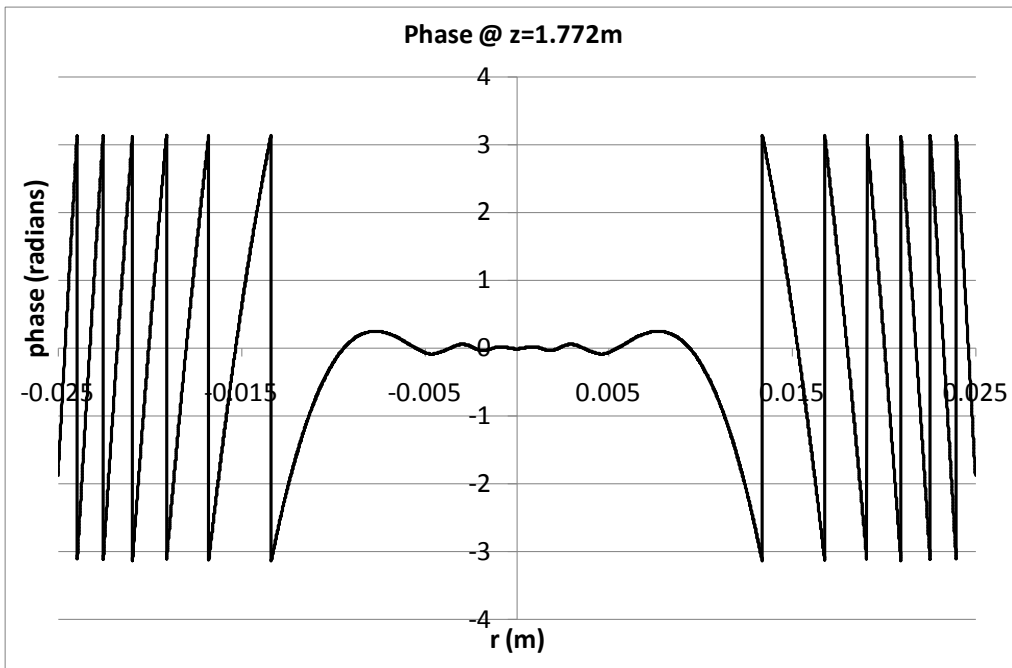


Figure 4-6 - FGB phase at the mirror position

The result of the phase of the beam as shown in Figure 4-6 was then used in step 3 of the design procedure to determine the phase profile of the DOE mirror for the resonator. The profile of the DOE mirror is shown Figure 4-7. For the manufacturing process the surface height of the profile on the mirror was modulated every $10.6\mu\text{m}$ in height. This corresponds to one complete wavelength of $10.6\mu\text{m}$ or a 2π phase shift in the light. The modulated mirror

surface profile is shown in Figure 4-8. Figure 4-8 represents the surface profile of the actual mirror that was manufactured at an optics manufacturer using a diamond turning technique.

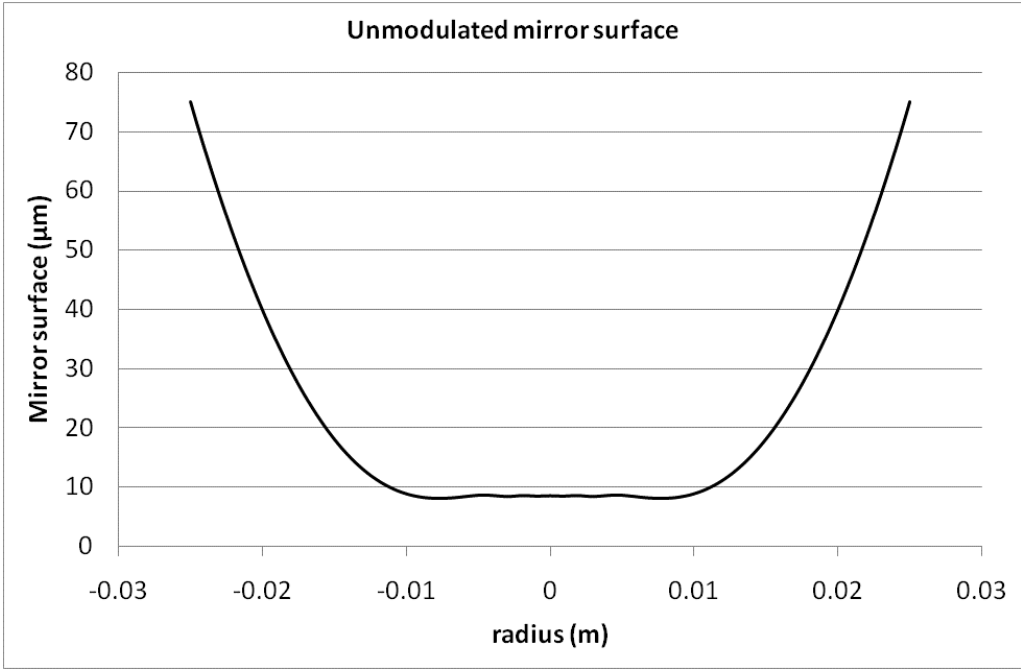


Figure 4-7 - DOE mirror profile

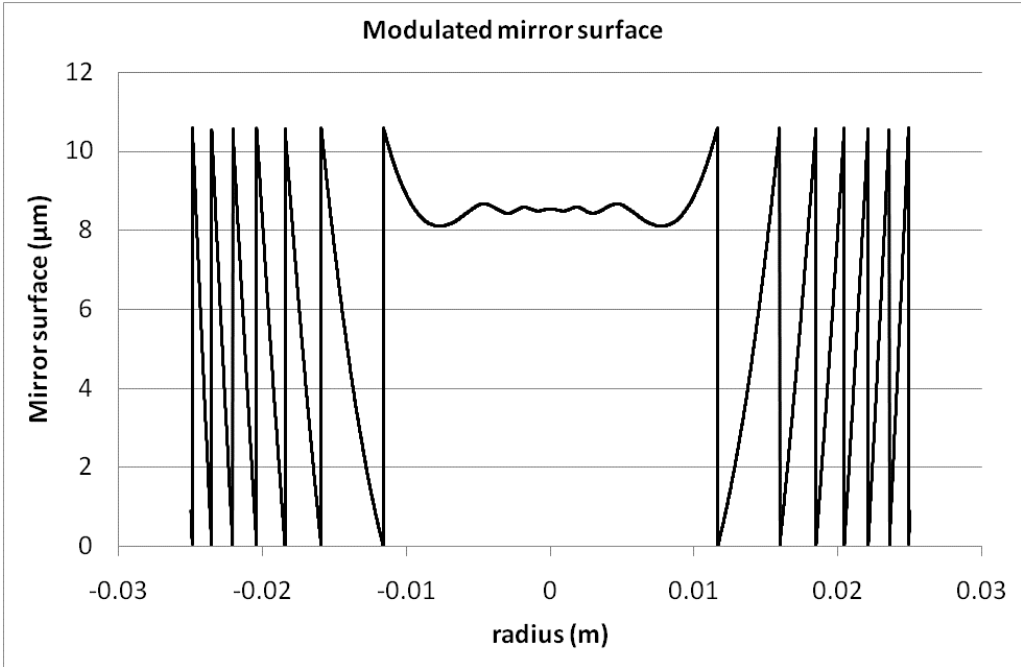


Figure 4-8 - Modulated surface profile of the DOE mirror

4.1.3 Stability analysis

To verify the results of the design a resonator cavity stability analysis was performed using the method of Fox and Li (14) and as outlined in Section 3.5. The implementation was done in MATLAB[®] together with the mirror design of the previous section.

In the implementation a starting field was specified at the output coupler of the resonator. The start field was then propagated to the DOE mirror. At the position of the DOE mirror the phase of the DOE mirror was added to the phase of the beam to introduce the effect of the DOE mirror on to the beam. The beam with the added phase was then propagated back to the output coupler. This process of propagating the beam back and forth was then repeated to simulate the propagation of the beam through the resonator. The propagation of the beam from the output coupler to the mirror and back to the output coupler is defined as a round trip in the resonator.

In the implementation of the simulation an aperture was introduced into the resonator to limit the area of calculation. In the physical implementation of the resonator a diameter 30mm aperture was inserted in the laser for reasons discussed elsewhere in this study. A diameter 30mm aperture was therefore introduced into the simulation resonator. The beam was therefore calculated from -15mm to 15mm for the one dimensional strip resonator. A step size of 5 μ m was used in traversing the beam from -15mm to 15mm during the simulations. This step size was chosen to make the results as accurate as possible while still calculating the beam propagation in a realistic time. A smaller step size would have been more ideal but would have taken significantly longer to compute.

As a first step to performing the stability analysis and to test the simulation program for the stability analysis an FGB was introduced at the output coupler and propagated for 5 round trips in the resonator. The FGB that was introduced was equivalent to the FGB that was used to design the resonator and the DOE mirror. This step was performed to determine whether the resonator will retain the FGB if an FGB was immediately introduced in the resonator. The introduced FGB and the output FGB after 5 round trips are shown in Figure 4-9. The figure shows that the shape of the FGB was changed to some extent in the resonator but is in essence still an FGB. The phase of the output beam is shown in Figure 4-10

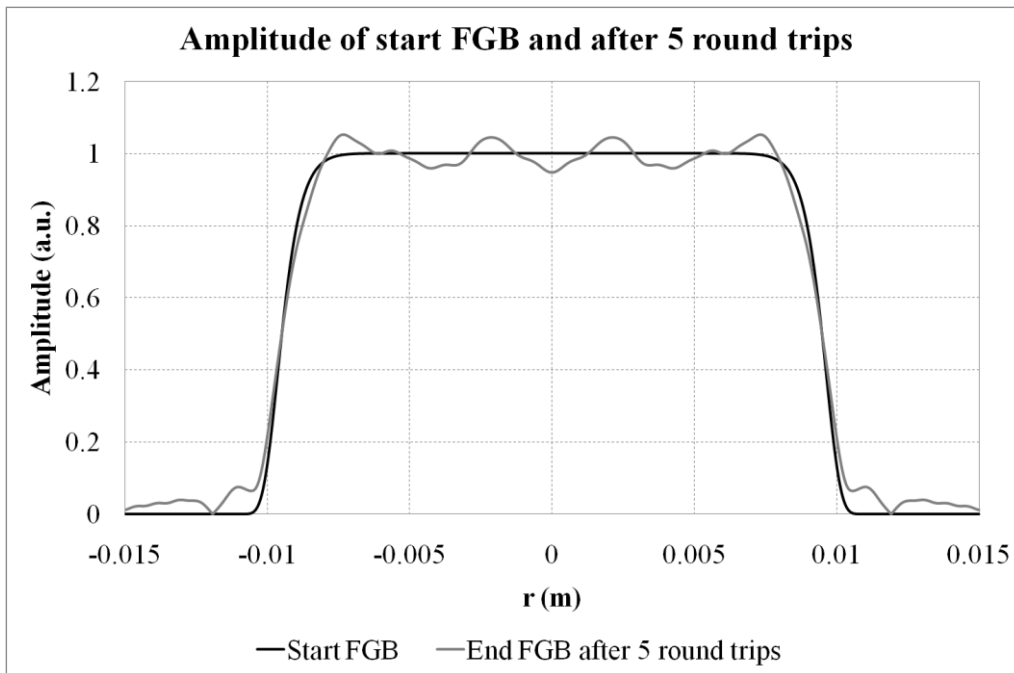


Figure 4-9 – Beam profiles for the case of the introduced FGB and output beam after 5 round trips

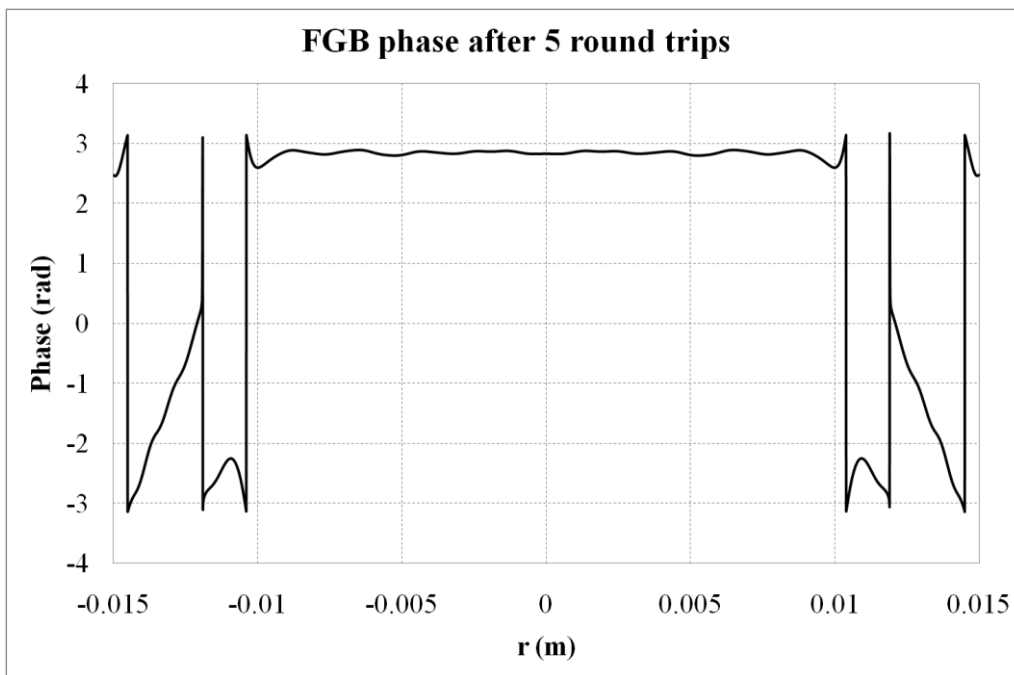


Figure 4-10 - Phase of the FGB after 5 round trips

The density plot of the beam profile at the output coupler after each round trip in the resonator is shown in Figure 4-11. This shows how the input FGB changed shape to the output FGB during the 5 round trips.

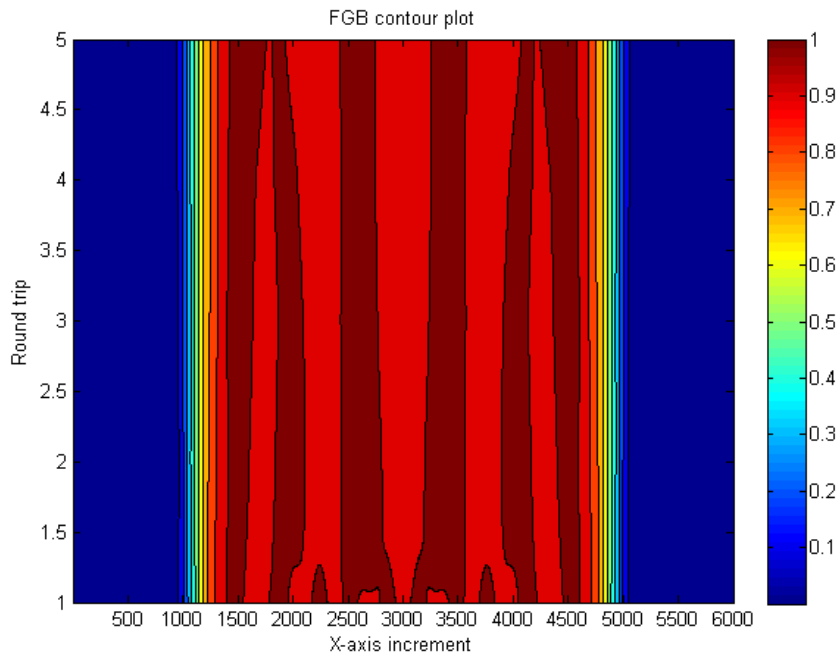


Figure 4-11 - Density plot of the propagation for the introduced FGB and output beam after 5 round trips

Following this the convergence of the custom resonator with the DOE mirror was tested. This was done by introducing a starting field of random noise at the output coupler for propagation through the resonator. The beam was propagated for 250 round trips through the resonator to test the convergence of the mode discrimination of the resonator. The starting field of random noise is shown in Figure 4-12.

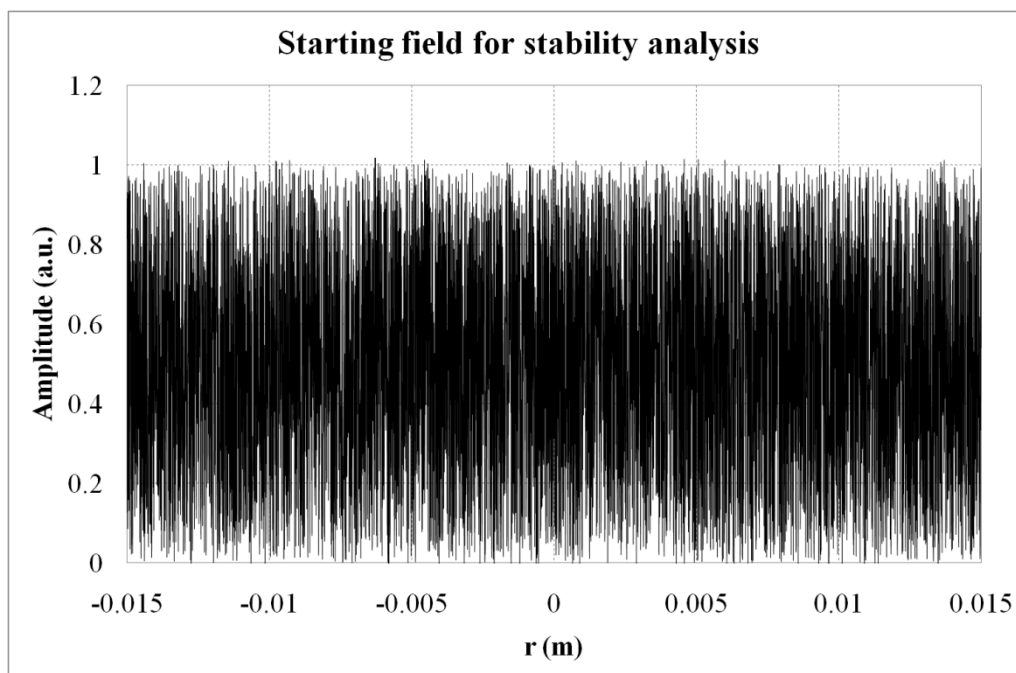


Figure 4-12 - Starting field of random noise

The output beam intensity profile at the output coupler after 250 round trips in the resonator is shown in Figure 4-13 and the phase is shown in Figure 4-14.

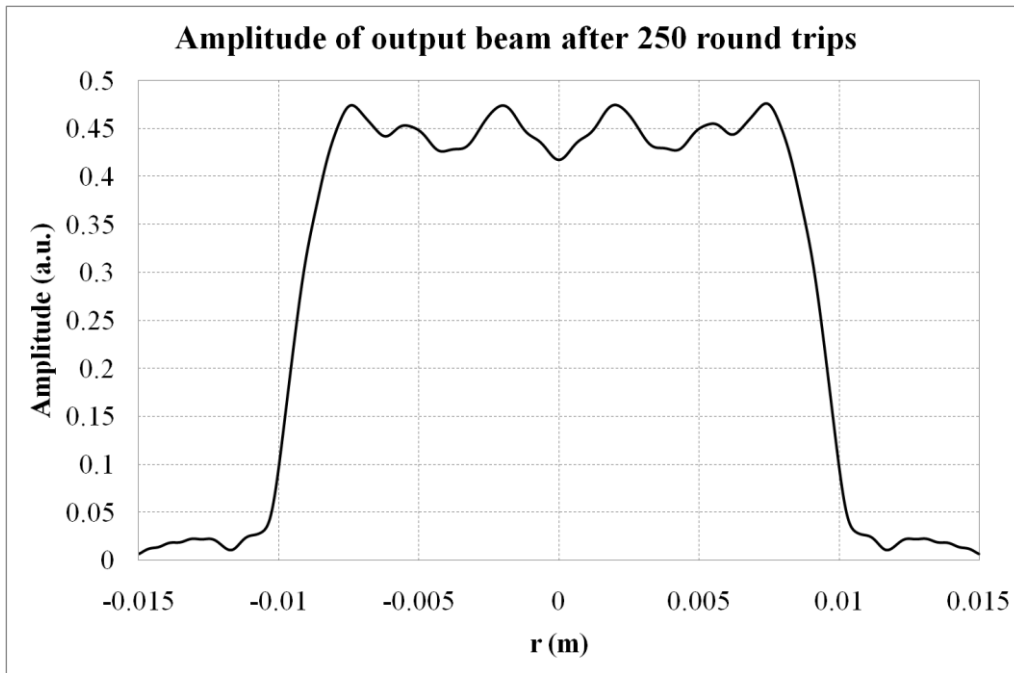


Figure 4-13 - Output beam intensity profile after 250 round trips

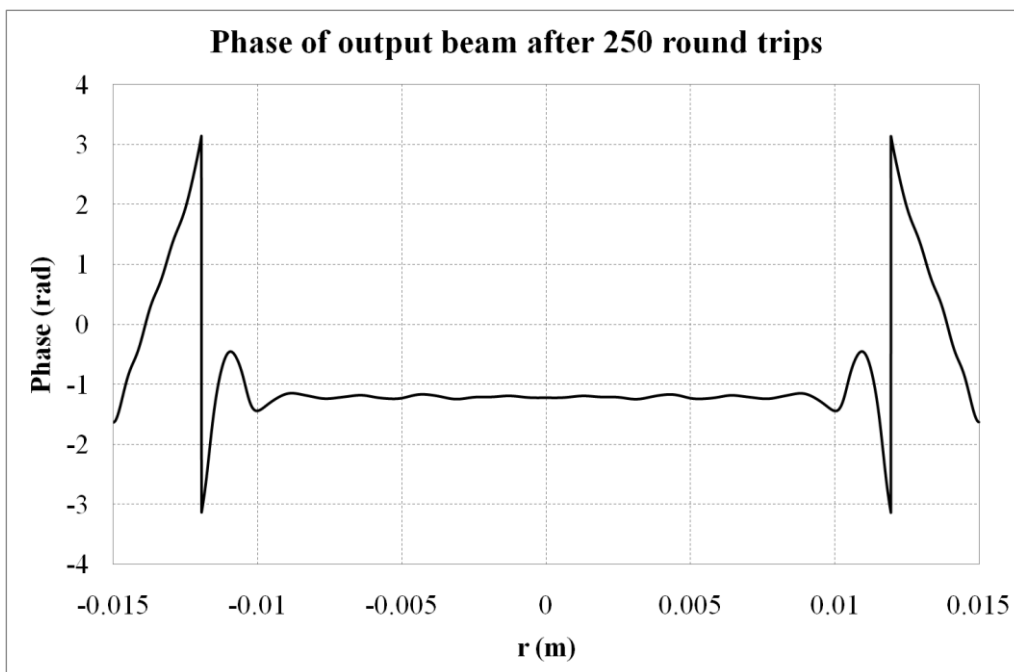


Figure 4-14 - Output beam phase after 250 round trips

The resulting beam profile from the resonator after 250 round trips in the resonator shown in Figure 4-13 is very similar in shape to the beam profile shown in Figure 4-9 where an FGB

was inserted into the resonator and completed 5 round trips. It would be useful to know whether the resonator output has converged to this profile sooner than the 250th round trip in the resonator. According to (31) the losses of the *i*-th round trip can be calculated through Equation 4-2 where γ is the energy contained in the field.

$$Loss = 1 - \frac{\gamma_i}{\gamma_{i-1}} \tag{4-2}$$

A loss analysis for the resonator was performed using Equation 4-2 and the results are plotted in Figure 4-15. It can be seen from the figure that the loss per round trip has decreased significantly by the time that 100 round trips are reached. From approximately 175 round trips the loss per round trip is virtually zero.

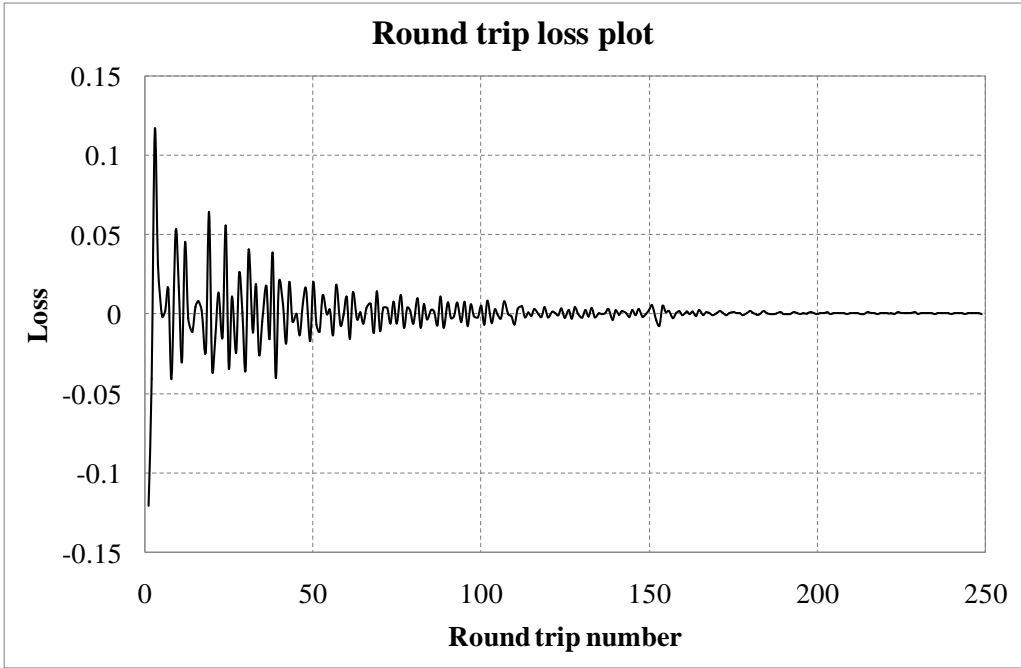


Figure 4-15 - Round trip loss plot for the resonator

Furthermore a density plot of the output beam profile for each round trip was created and is shown in Figure 4-16. In the figure it can clearly be seen how the output beam starts at the noise input field as indicated in Figure 4-12. For the increasing value of the round trips on the y-axis one can see how the output beam converges to a flattened irradiance profile beam. This figure also suggests that a fairly stable condition in the resonator is reached after 100 round trips and that the output is very stable after approximately 175 round trips.

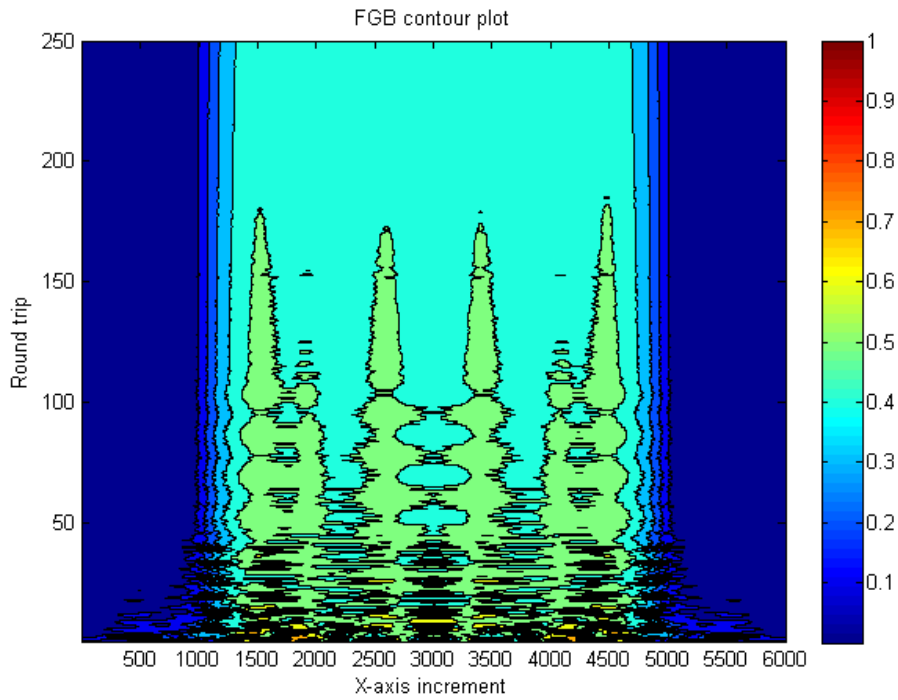


Figure 4-16 - Density plot of the output beam

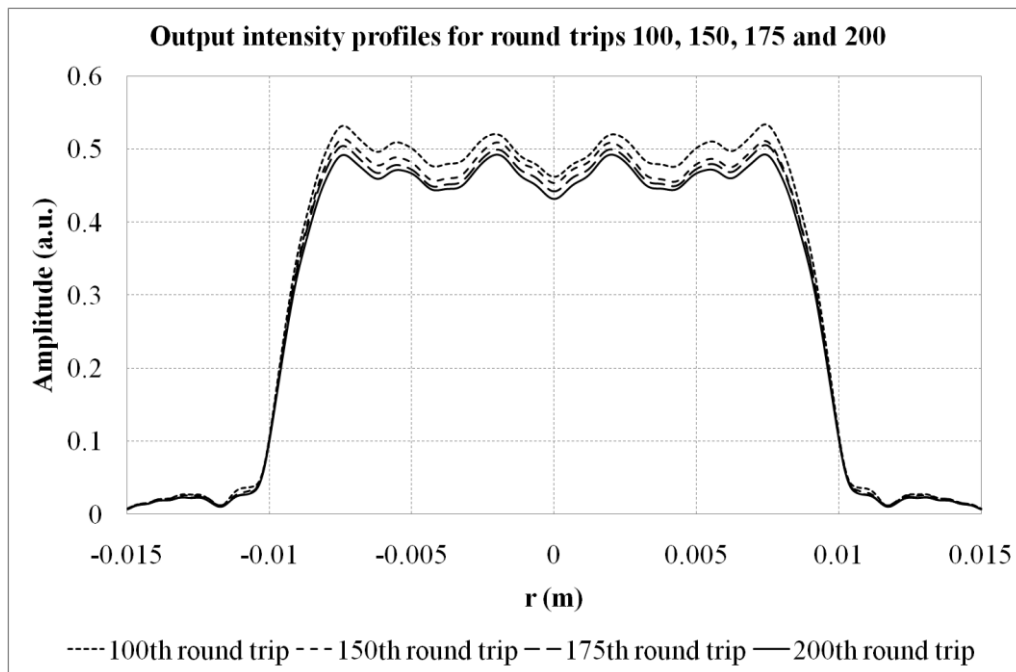


Figure 4-17 - Output intensity profiles after 100, 150, 175 and 200 round trips

Following the loss analysis and the output beam profile contour plot, the output beam shape at various round trip numbers beyond 100 round trips were investigated. The plot in Figure 4-17 shows the beam profile after 100, 150, 175 and 200 round trips in the resonator. From the

figure it can be seen that the profiles are consistent. Only the overall amplitude is decreasing as the round trips increase as there is no gain term in the beam propagation calculation taking the laser gain into account.

4.2 Laser beam characterisation

When the DOE mirror is implemented on the laser resonator there are various laser beam parameters that must be measured to verify the operation of the beam and to correlate the reality with the design. To properly comprehend the implications of the FGB one would have to know the beam parameters of the multimode and TEM₀₀ beams as well. This will allow one to compare the beams and relate them to each other.

The specific beam parameters that are of interest here for the application of the laser in materials processing application is the beam power or energy, the profile of the beam and the propagation parameters such as the M^2 parameter and the divergence of the beam. The following paragraphs will cover the detail of the beam characterisation measurements as they will be performed during the experimental work in the laboratory on the laser.

4.2.1 Pulse energy measurements

The laser pulse energy will simply be determined by measuring the output power of the laser with a suitable power head for the output wavelength of 10.6 μ m. The measured power value will be divided by the repetition rate of the laser to arrive at the energy per pulse. During the measurement the laser will be operated at a given repetition rate and time will be allowed for the output power of the laser to stabilise. At this stabilised output point the laser resonator alignment will be optimised for maximum output power. The stabilised output power value will be used to calculate the laser pulse energy.

4.2.2 Beam profile measurements

The characterisation of laser beams is presented in a summarised method by Rypma (17). According to Rypma (17) the analysis of the laser beam profile can be defined as the measurement, numerical analysis and visual display of the laser beam's spatial energy density distribution or intensity profile. The analysis of the laser beam profile can provide various properties regarding the laser beam. By performing a numerical analysis on the laser beam one can determine the size, shape and position of the beam. One can furthermore determine the mode structure and the uniformity of the beam as well as the beam stability. The beam propagation can also be found by performing the numerical analysis and this will be covered

in the next paragraph. Analysis of the laser beam also provides qualitative properties of the beam. By visually inspecting the beam profile one can assess the alignment of the beam. Viewing the alignment of the beam will allow one to assess the cavity tuning and clipping of the beam etc. Visual inspection will also allow the assessment of the mode structure with the ability to identify hot spots, interference and diffraction effects.

The place on the z-axis that is chosen for the beam profile measurement is very important. In general there are two regions in the propagation of the laser beam and they are called the near field and the far field. The near field part of the beam is the part of the beam immediately after the laser. In the near field region the beam is dominated by a disordered wave front and the characteristics of the beam are not very stable in this region. At some distance from the laser the far field part of the beam begins. In the far field region the wave front of the beam becomes ordered and the characteristics of the laser beam are stable in this region. For example in the far field region the divergence of the laser beam will be constant. The start of the far field region can be estimated as the point on the z-axis calculated by the formula in Equation 4-3. In the equation the parameter d is the beam width or diameter and λ is the wavelength of the laser beam. For the FGB with a diameter of 20mm the far field will start at approximately 38m from the output coupler and for the multimode beam with a width of 30mm the far field will be beyond 9m in the propagation path.

$$Z_f \approx d^2 / \lambda \quad 4-3$$

To measure the laser beam profile in the far field would be the ideal region to do so. To measure the beam profile in the far field will, however, be impractical and sometimes impossible to do as the suitable position in far field might be very far away from the output coupler of the laser. An optical sampling technique can be employed to transform the beam into the far field in a short distance for the laser beam profile measurement in the far field. This is commonly done by using a focussing lens or mirror to create the far field at the optical focal plane of the element. A suitable method to measure the laser beam profile can then be introduced at the focal plane of the optical element.

The beam profile can be measured using a variety of different methods. Qualitative profile measurement methods such as mode burns on film, paper and Plexiglass can be employed.

Imaging fluorescence or phosphorescent conversion techniques will also yield qualitative beam profile measurements. The beam profile can also be measured using quantitative measurement techniques. The method of a mechanically scanned aperture such as a knife-edge, slit, circular and pinhole apertures could be employed to determine the laser beam profile. One can also utilize two dimensional linear detector arrays for measuring the beam. Finally a camera based device could be used to measure the laser beam profile.

During the execution of the experimental work in this study two methods will be used to view the laser beam profile. Firstly qualitative measurements of the beam during the alignment and set up will be made with thermal paper. Finally a pyroelectric camera will be employed for quantitative beam measurements. The beam measurements in this study will be obtained with a LBA-PC-PIII pyroelectric Pyrocam III camera from Spiricon Laser Beam Diagnostics. Further on in this text the camera will simply be referred to as the Pyrocam III. A picture of the Pyrocam III is shown in Figure 4-18.

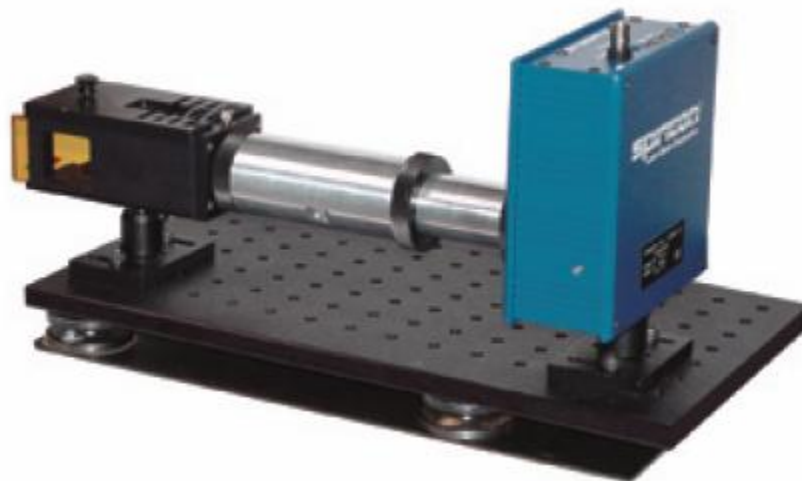


Figure 4-18 - Spiricon Pyrocam III

The pyroelectric camera has the advantage that it can measure a two-dimensional mapping of the energy distribution that provides the data that can be used for quantitative analysis of the beam. The camera also has the advantage that it can capture single laser pulses and short term events. The camera does, however, have some drawbacks to it. The camera has a high sensitivity and a low damage threshold. The beam must therefore be properly attenuated during the beam measurements. The camera also has a low optical dynamic range which requires special treatment of optical and electronics sources of background noise. The camera

sensor array also usually differs in size from the laser beam that it is to be measured. The beam must therefore be optically manipulated through a telescope or another imaging technique to match the laser beam size to the detector size.

For the purpose of this thesis it is required to measure the far field image of the beam as well as the image of the beam at the output coupler of the laser. For the TEA CO₂ laser that will be used for the experimental work the multimode beam will be rectangular and will be in the order of 30mm by 30mm in size at the output coupler. The FGB beam is expected to be 30mm in diameter at the output coupler. Due to the divergence of each beam it will grow in size as it propagates along the z-axis. The detector array of the Pyrocam III contains 15,376 elements in a 124 x 124 element array. The pixel size of each element is 85μm x 85μm and the elements are spaced in a grid of 100μm x 100μm. The active area of the detector array is therefore 12.4mm x 12.4mm in size. One therefore has to employ a suitable technique to manipulate the beam so that it fits onto the detector array.

The beam can be imaged onto the detector array of the Pyrocam III by inserting a lens in the beam path between the laser and the camera. The far field image of the beam can then be measured at the focal plane of the lens and the image at the output coupler at a calculated specific distance from the lens. Figure 4-19 shows the imaging of the laser beam onto the array detector. The object height is designated by y_o and in this case the image of the laser beam at the output coupler of the laser will be the object. The image height is designated by y_i and in this case the image will be the projection of the beam onto the array detector. The lens must then be placed at the distance S_o from the output coupler. The array detector must then be either placed at the focal plane of the lens or at the distance S_i from the lens for the measurements that must be made with the Pyrocam III. Equation 4-4 and Equation 4-5 must be used to calculate the distances based on the choice of a suitable lens for the measurements.

$$\frac{1}{f} = \frac{1}{S_o} + \frac{1}{S_i} \quad 4-4$$

$$M_T = \frac{y_i}{y_o} = -\frac{S_i}{S_o} \quad 4-5$$

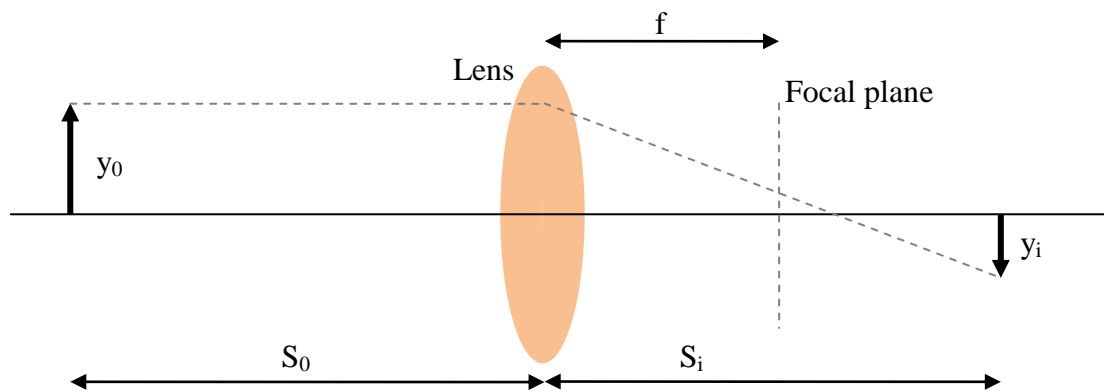


Figure 4-19 - Imaging of the beam

4.2.3 Beam propagation measurements

Apart from measuring the laser beam profile for analysis of the energy density distribution etc, it will also be useful to get other information from the measurements. Specifically the beam propagation factor also known as the M^2 parameter and the divergence of the beam would be useful in designing the optical beam delivery system for a materials processing application.

According to Roundy (18) the beam propagation factor or M^2 parameter is the parameter that quantitatively compares the propagation characteristics of the real beam being measured to characteristics of a pure TEM₀₀ Gaussian beam. This comparison allows one to predict the focused spot size, the irradiance of the focused spot, the Raleigh range of the beam and the far field divergence of the beam for a given input beam width and lens focal length. Knowing these parameters of the multimode beam allows one to predict its propagation and to design a beam delivery system for the beam.

The practical implications of the M^2 parameter are worth mentioning and will be briefly described here. According to (18) and (19) the M^2 parameter is commonly used to determine the size of a focused spot when a focussing lens is inserted into the beam. Figure 4-20 shows the focused spot size for two beams with input beam waists D_{00} and D_0 to the lens. The beam with the D_{00} input waist has a M^2 value of 1 and the beam with the D_0 input waist has a M^2 value that is larger than one. The focal spot diameter can be determined through Equation 4-6 where λ is the wavelength, f is the focal length of the lens and D_0 is the width of the waist of the input multimode beam at the focal length of the lens.

$$d_0 = \frac{M^2 4\lambda f}{\pi D_0} \quad 4-6$$

Equation 4-6 shows that the focused spot size of the beam d_0 is M^2 times larger than the spot size for a TEM₀₀ Gaussian beam with the same input diameter D_0 . For example if $M^2 = 2$ for a beam, the focused spot size of the beam is twice as large as the focused spot size that could be obtained with a TEM₀₀ beam. The irradiance of the beam which is proportional to the square of the beam width will only be one fourth for the multimode beam of the achieved irradiance for the TEM₀₀ Gaussian beam.

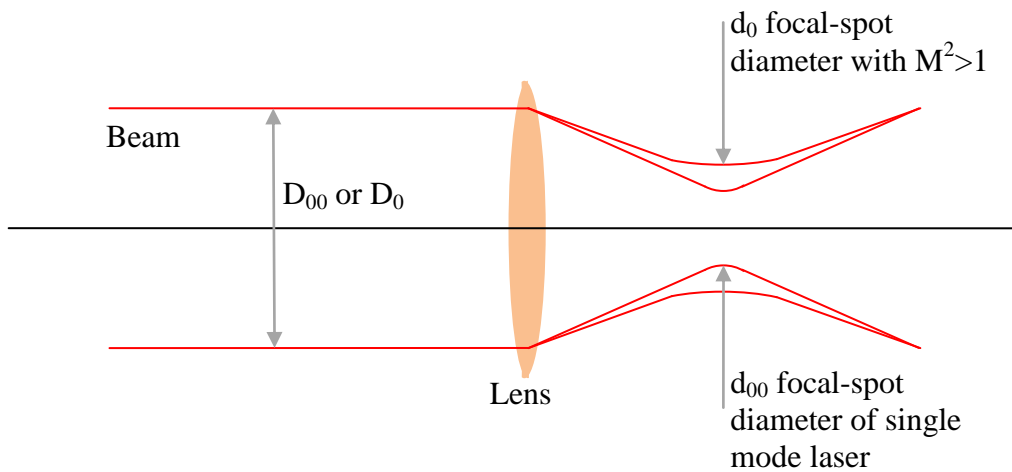


Figure 4-20 - Focus of two beams with different M^2 values

The method of measuring the M^2 parameter is quite cumbersome and must be executed with great accuracy to get accurate and meaningful results. The measurement can unfortunately not be done through a single measurement or calculation. In the ISO standard ISO 11146 (22) a methodology for measuring the M^2 has been defined that provides reliable measurement of the M^2 parameter. The method is also described by Roundy (18). To perform the measurement one must use a lens with a known focal length and insert it in the path of the laser beam. A series of beam width measurements must then be made through the focused waist of the laser beam as shown in Figure 4-21. It is important to make sure that the beam width is measured in the focus at the smallest beam position and also at the focal plane of the lens. These are not necessarily the same places in the beam path. It is also important to measure the beam width beyond the focus to obtain the divergence. The accuracy of the measurement is increased if

one takes a series of beam width measurements at various positions and then performs a curve fit to the measured data to be able to calculate the M^2 parameter. It is also important to note that the Second Moment (D4 σ -width) method of obtaining the beam size must be used to ensure the accuracy of the measurements. According to Rypma (17) the D4 σ -width of the laser beam is the beam size determined on the Second Order Spatial Moment of the beam Energy Intensity Density distribution. The D4 σ -width can only be determined directly from data from a camera or pin-hole based beam intensity profile measurement. In the case of a Gaussian beam the D4 σ -width will yield similar beam width results as the other $1/e^2$ methods.

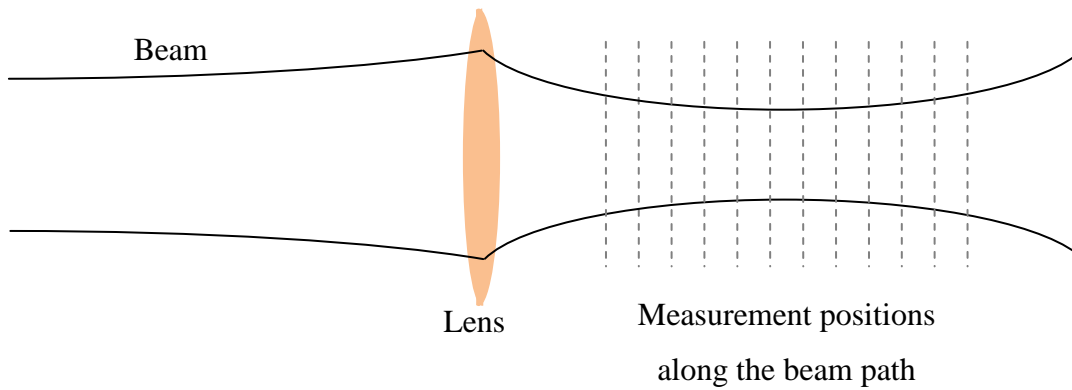


Figure 4-21 - Beam width measurements in focus area

The mathematics for the curve fit to the measured data can be done as follow. Consider Equation 4-7 which describes the spot size ω for propagation of a Gaussian beam along the z -axis. Through some manipulation Equation 4-8 can be rewritten into a second order polynomial form as shown in Equation 4-8.

$$\omega^2(z) = \omega_0^2 \left(1 + \left(\frac{z - z_0}{z_R} \right)^2 \right) \quad 4-7$$

$$\omega^2(z) = \left[\frac{\omega_0^2}{z_R^2} \right] z^2 - \left[\frac{2z_0\omega_0^2}{z_R^2} \right] z + \frac{z_0^2\omega_0^2}{z_R^2} + \omega_0^2 \quad 4-8$$

The coefficients of Equation 4-8 can be equated to the generic coefficients of the second order polynomial equation as shown in Equation 4-9, Equation 4-10 and Equation 4-11.

$$a = \frac{\omega_0^2}{z_R^2} \quad 4-9$$

$$b = -\frac{2z_0\omega_0^2}{z_R^2} \quad 4-10$$

$$c = \frac{z_0^2\omega_0^2}{z_R^2} + \omega_0^2 \quad 4-11$$

Through further manipulation of the above mentioned equations, equations for the Rayleigh range, beam waist position and beam waist size can be readily obtained. This is shown in Equation 4-12, Equation 4-13 and Equation 4-14.

$$z_R = \frac{\omega_0}{\sqrt{a}} \quad 4-12$$

$$z_0 = -\frac{b}{2a} \quad 4-13$$

$$\omega_0 = \sqrt{c - \frac{b^2}{4a}} \quad 4-14$$

If the square of the measured beam radius data for the focus region is plotted against the z -axis, a graph is obtained on which a second order polynomial fit can be done. An example of the curve is shown in Figure 4-22. The equation of the polynomial fit will be of the form $y=ax^2+bx+c$. The values of the coefficients a , b and c can then be read from the fitted polynomial equation. The Rayleigh range, beam waist position and beam waist size can then be determined by inserting the obtained coefficient values into Equation 4-12, Equation 4-13 and Equation 4-14 respectively. The M^2 parameter is defined through Equation 4-15 and can hence be calculated from the results of Equation 4-12, Equation 4-13 and Equation 4-14. This method has been suggested and used by Forbes (21) to calculate these parameters.

$$M^2 = \frac{\pi\omega_0^2}{z_R\lambda} \quad 4-15$$

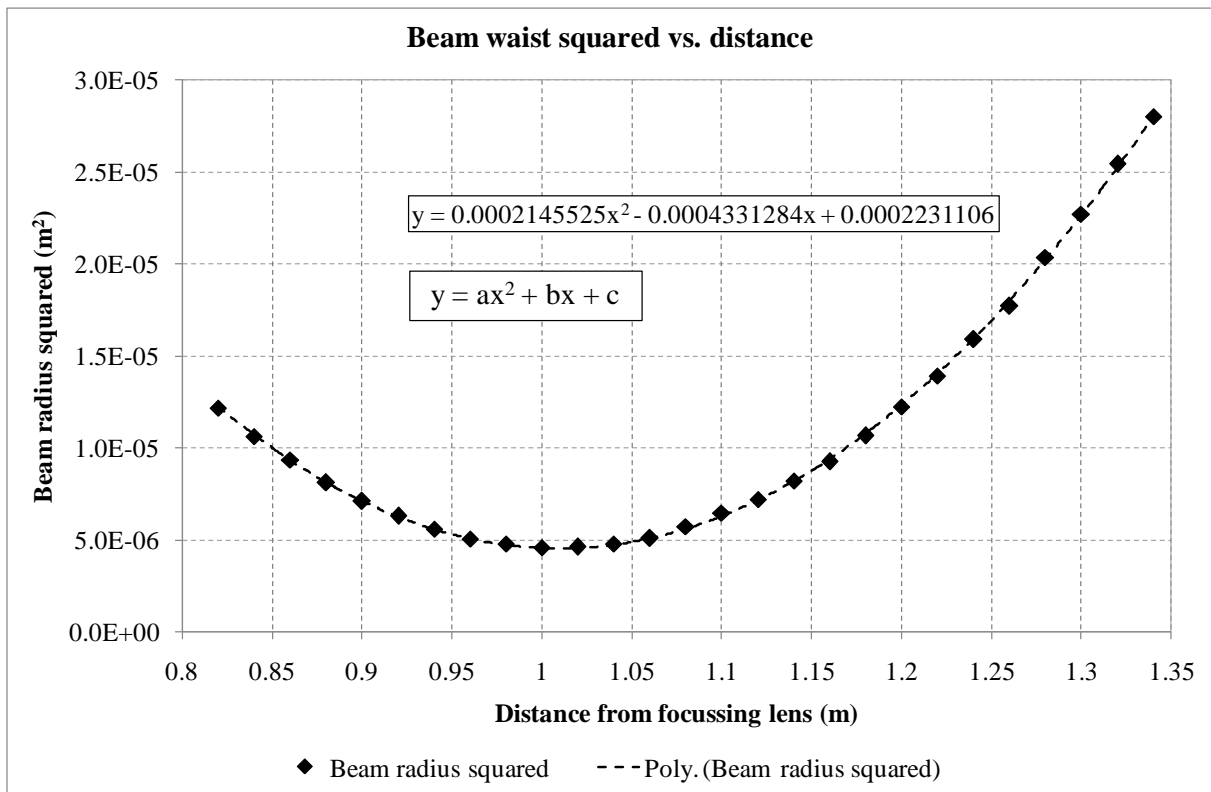


Figure 4-22 - Beam size measurement results

Finally the beam divergence θ must be determined. This can be done by calculating it from the M^2 parameter according to Equation 4-16 as defined by Svelto (24). The beam divergence can also be calculated by using the beam diameter size in the focal plane of the lens and the focal length of the lens according to Equation 4-17. This method is also described by the Pyrocam III manual (20). The method of determining the beam divergence by using equation 4-16 yields the half angle divergence of the laser beam radians. The focal plane method according to Equation 4-17 yields the full angle divergence of the laser beam in radians.

$$\theta_0 = \frac{M^2 \lambda}{\pi \omega_0} \quad 4-16$$

$$\theta_0 = \frac{\omega_{focal\ plane}}{f} \quad 4-17$$

The focal plane method yields the best results for the beam divergence value if the input beam to the lens is collimated. Since the M^2 parameter has been determined as described above by

using many measurements through the focus area of the lens, it is assumed that a more accurate value for the divergence will be obtained if it is calculated using Equation 4-16.

In conclusion Siegman et al. also discussed the subjects of the M^2 parameter and beam width measurement methods such as the Second Moment method as mentioned above in Reference (34). The Reference also explores the topic of other methods of specifying the beam quality apart from the M^2 parameter.

5 RESULTS

The previous chapters explored the topics of FGBs and the design of the laser resonator and the appropriate DOE for the resonator so that the resonator can yield an FGB. The DOE in question was then manufactured according to the design in Chapter 4 by an optics manufacturer using the diamond turning technique. The DOE was received from the manufacturer and installed on the TEA CO₂ laser. This chapter presents the experimental results that were measured in the laboratory for the TEA CO₂ laser. The TEA CO₂ laser was first characterised in terms of its multimode and TEM₀₀ beam propagation properties. Following this the DOE was installed on the resonator and the laser was further characterised for the DOE. The results of the multimode, TEM₀₀ and FGB beam characteristics are summarised and discussed in Section 6.1.3.

The laser with the custom DOE resonator was finally used in a practical paint removal application. The laser based paint removal system and results that were obtained with the system are also presented in this chapter.

5.1 Laser characterisation

The multimode and TEM₀₀ beam propagation properties of the TEA CO₂ laser were first characterised in the laboratory experimental work. This was done to form a basis of comparison for the FGB propagation properties that were to be measured later on. During the characterisation of the beam propagation the beam profile measurements as described in paragraph 4.2.2 and the beam propagation measurements as described in paragraph 4.2.3 were performed. Following the measurements the results were analysed and processed and are finally presented in the following paragraphs of this thesis.

5.1.1 Multimode beam results

The multimode beam was generated by configuring the resonator as shown in Figure 5-1. In this configuration a flat ZnSe output coupler and a concave gold coated copper mirror was used to form a stable long radius hemispherical optical resonator. For this implementation the laser yields a rectangular shaped beam where the higher order modes are present in the beam.

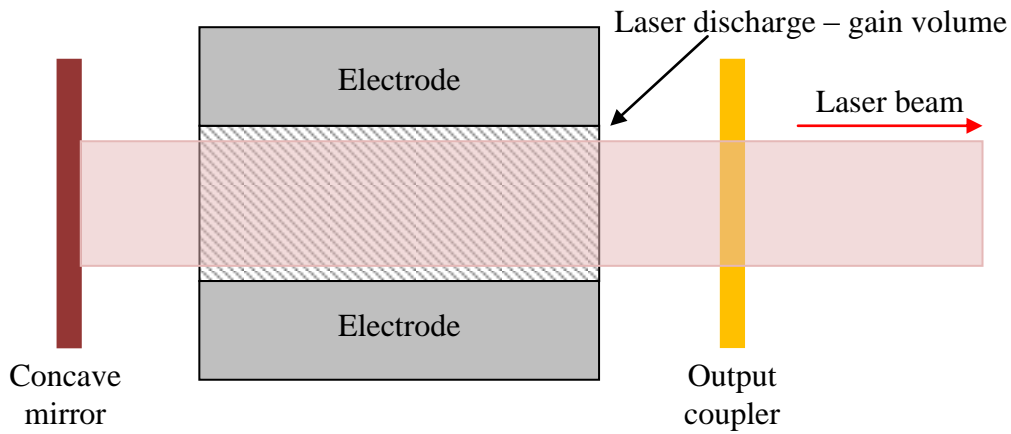


Figure 5-1 – Multimode laser resonator

Figure 5-2 shows the results of the beam propagation measurement that was performed according to paragraph 4.2.3. The figure shows the squared beam radius as measured for each axis vs. the distance from the focussing lens. The fitted curves to the data with the accompanying equations were used to calculate the M^2 parameter and beam divergence.

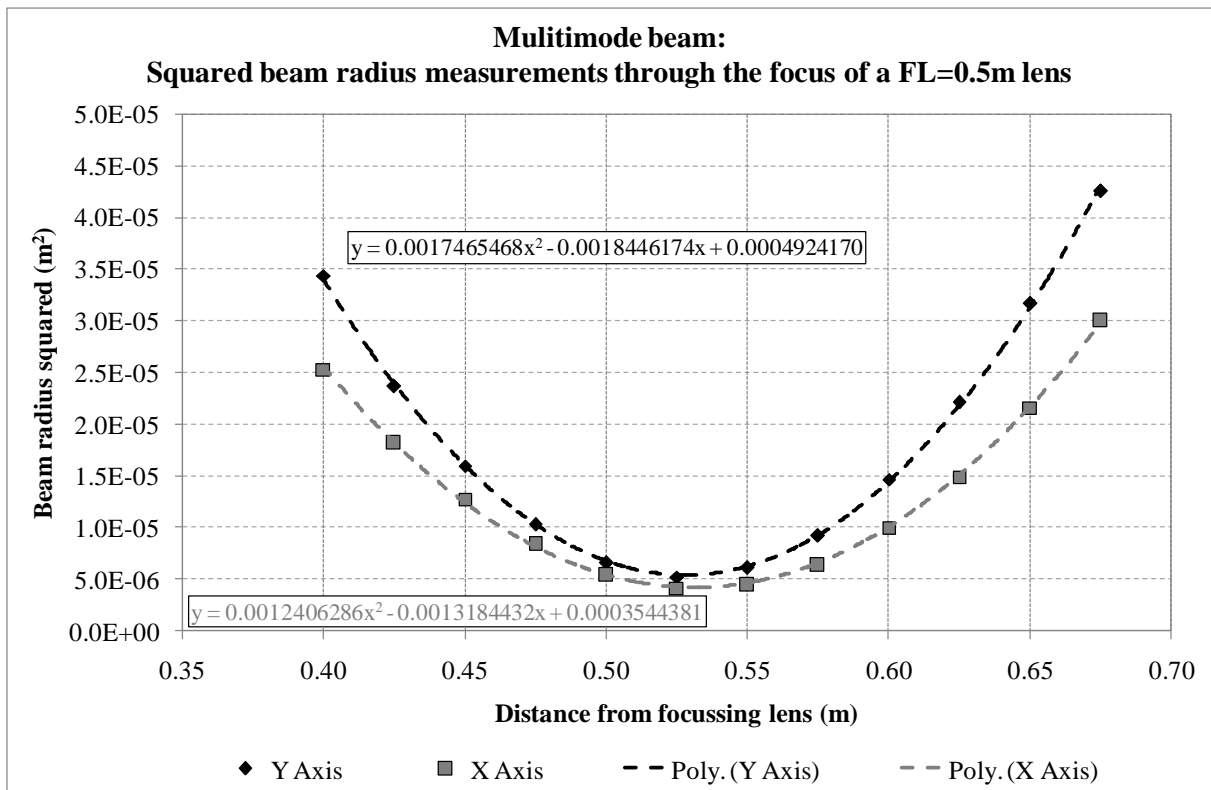


Figure 5-2 – Focused multimode beam size measurements

Table 5-1 summarises the parameters of the beam for the multimode beam. The table presents the calculated M^2 parameters and the beam divergence as well as the pulse energy.

Parameter	X-Axis	Y-Axis
M^2 Parameter	21.3	28.7
Divergence	35.3mrad	41.8mrad
Pulse energy	6.3J	

Table 5-1 – Multimode beam results

Figure 5-3 shows the far field image of the multimode beam. This image was taken with the Pyrocam III at a distance from the lens equal to the focal length of the lens for the beam propagation measurements. These measurements were performed according to the procedure that was outlined in paragraph 4.2.2.

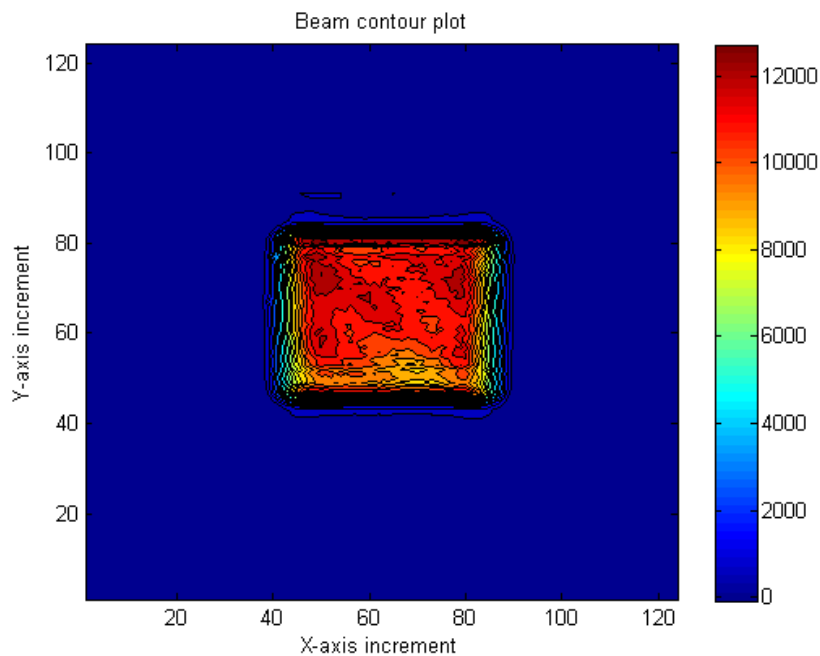


Figure 5-3 - Multimode beam far field image

Figure 5-4 shows the image of the multimode beam as it is at the output coupler of the resonator. This image was taken with the Pyrocam III at a calculated distance from the lens that was used to focus the beam for the beam propagation measurements. At this distance the set-up creates an exact scaled-down image of the beam at the output coupler projected onto the detector. These measurements were performed according to the procedure that was outlined in paragraph 4.2.2. Both of the images in Figure 5-3 and Figure 5-4 represent the image as captured on the detector of the Pyrocam III. With reference to Section 4.2.2 the detector size is 12.4mm x 12.4mm and the images in the figures therefore represent a 12.4mm

x 12.4mm size. As previously mentioned the beam was focused with a lens to fit the beam onto the detector. It should be noted that the image of the beam in Figure 5-4 is inverted if compared to the image in Figure 5-3 due to the fact that the image was taken beyond the focal plane of the lens.

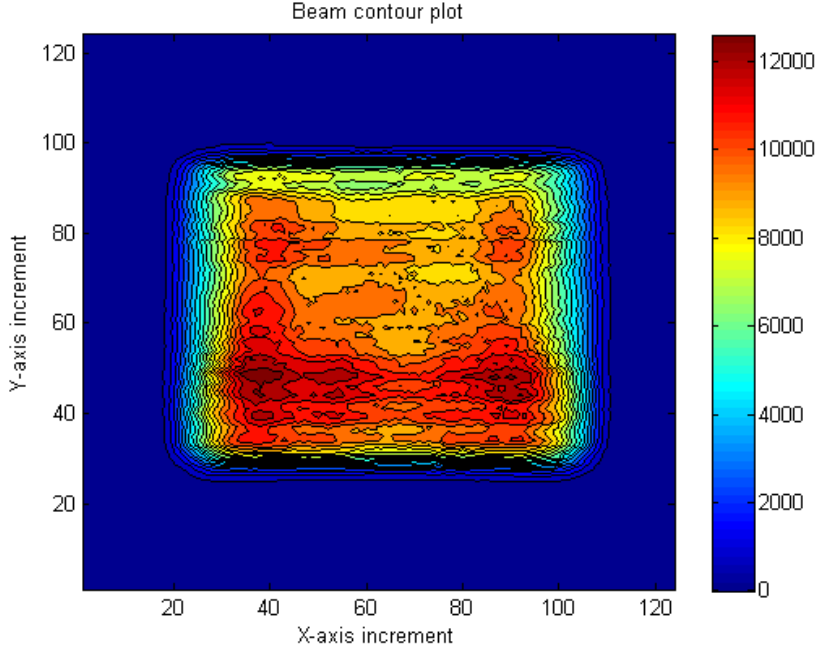


Figure 5-4 - Multimode beam image at the output coupler

5.1.2 TEM₀₀ beam results

The TEM₀₀ beam was generated by configuring the resonator as shown in Figure 5-5. In this configuration a flat output coupler and a concave gold coated copper mirror was used to form a stable long radius hemispherical optical resonator. An aperture was inserted into the resonator at the concave mirror side to select the TEM₀₀ mode. In this configuration the laser yields a circular shaped beam with a Gaussian intensity profile.

Figure 5-6 shows the results of the beam propagation measurement that was performed according to paragraph 4.2.3. The figure shows the squared beam radius as measured for each axis vs. the distance from the focussing lens. The fitted curves to the data with the accompanying equations were used to calculate the M^2 parameter and beam divergence.

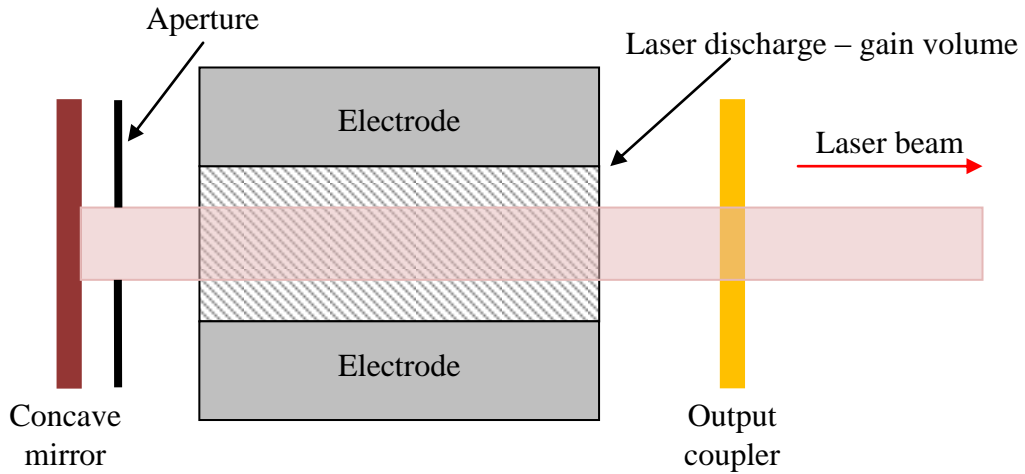


Figure 5-5 – TEM₀₀ mode laser resonator

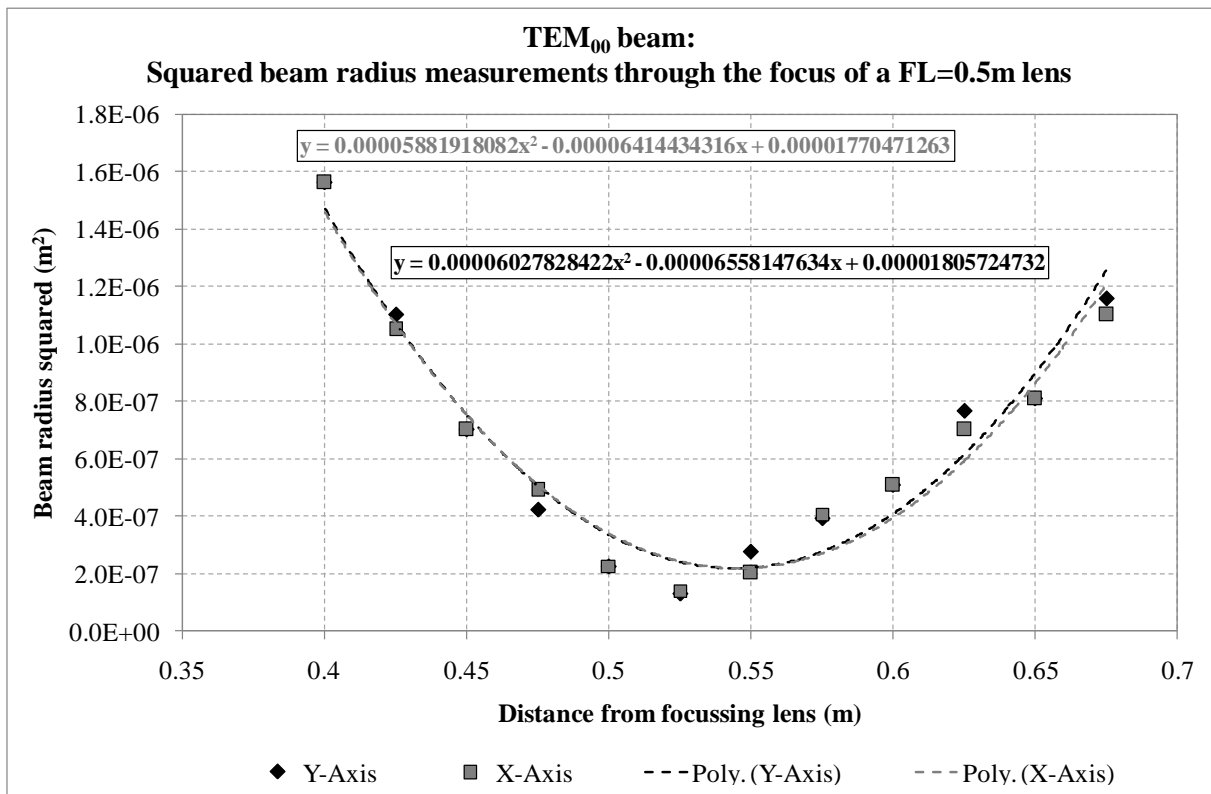


Figure 5-6 - Focused TEM₀₀ beam size measurements

The Table 5-2 summarises the parameters of the beam for the TEM₀₀ beam. The table presents the calculated M^2 parameters and the beam divergence as well as the pulse energy.

Parameter	X-Axis	Y-Axis
M^2 Parameter	1.06	1.08
Divergence	7.7mrad	7.8mrad
Pulse energy	250mJ	

Table 5-2 – TEM₀₀ beam results

Figure 5-7 shows the far field image of the TEM₀₀ beam. This image was taken with the Pyrocam III at a distance from the lens equal to the focal length of the lens for the beam propagation measurements. These measurements were performed according to the procedure that was outlined in paragraph 4.2.2. Figure 5-8 shows the image of the TEM₀₀ beam as it is at the output coupler of the resonator. This image was taken with the Pyrocam III at a calculated distance from the lens that was used to focus the beam for the beam propagation measurements. At this distance the set-up creates an exact scaled-down image of the beam at the output coupler projected onto the detector. These measurements were performed according to the procedure that was outlined in paragraph 4.2.2. The images in Figure 5-7 and Figure 5-8 once again represent a 12.4mm x 12.4mm area. It should be noted that the image of the beam in Figure 5-8 is inverted if compared to the image in Figure 5-7 due to the fact that the image was taken beyond the focal plane of the lens.

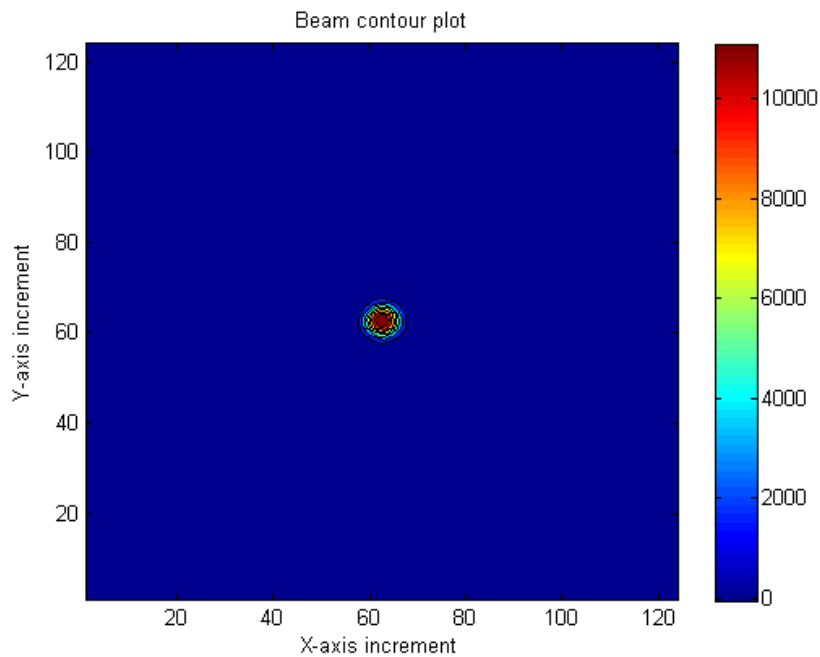


Figure 5-7 – TEM₀₀ beam far field image

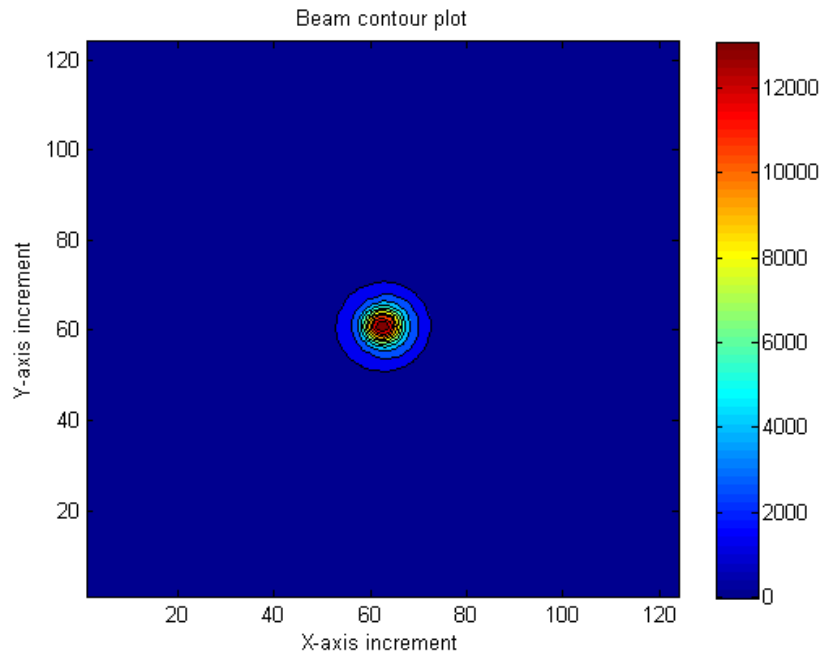


Figure 5-8 - TEM₀₀ beam image at the output coupler

5.2 Installation of DOE in the laser resonator and FGB results

Following the laser characterisation for the multimode and TEM₀₀ cases the DOE was installed onto the laser resonator for the generation of the FGB. The FGB was then characterised similarly to the other beam modes of the laser. Initial experiments with the DOE were performed with an open gain volume in the laser resonator. Due to the results that were obtained in this configuration a decision was made to install a suitable aperture in the laser resonator to limit the available gain volume for the generation of the FGB. The results for both of these cases are presented in the following paragraphs.

5.2.1 FGB results – open gain volume

The FGB was generated by configuring the resonator as shown in Figure 5-9. In this configuration a flat output coupler and DOE gold coated copper mirror were used to form a stable long radius hemispherical optical resonator. In this configuration the laser yields the FGB.

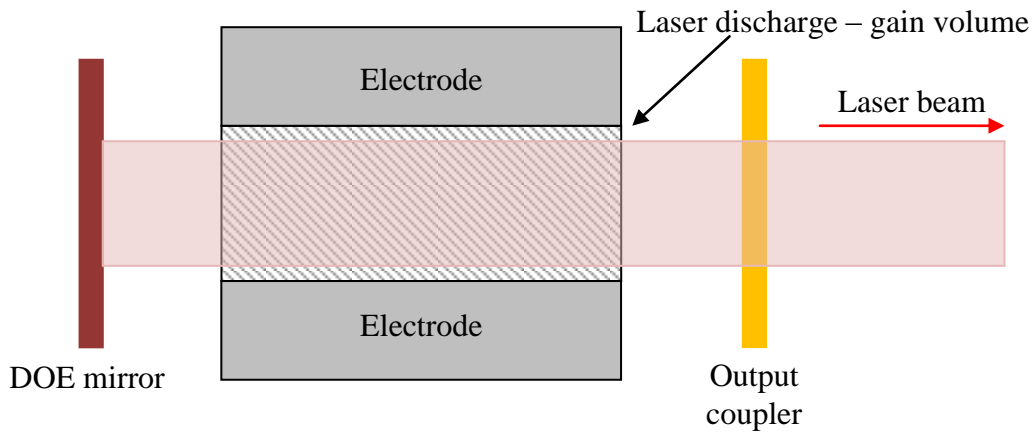


Figure 5-9 – FGB mode laser resonator

Figure 5-10 shows the results of the beam propagation measurement that was performed according to paragraph 4.2.3. The figure shows the squared beam radius as measured for each axis vs. the distance from the focussing lens. The fitted curves to the data with the accompanying equations were used to calculate the M^2 parameter and beam divergence.

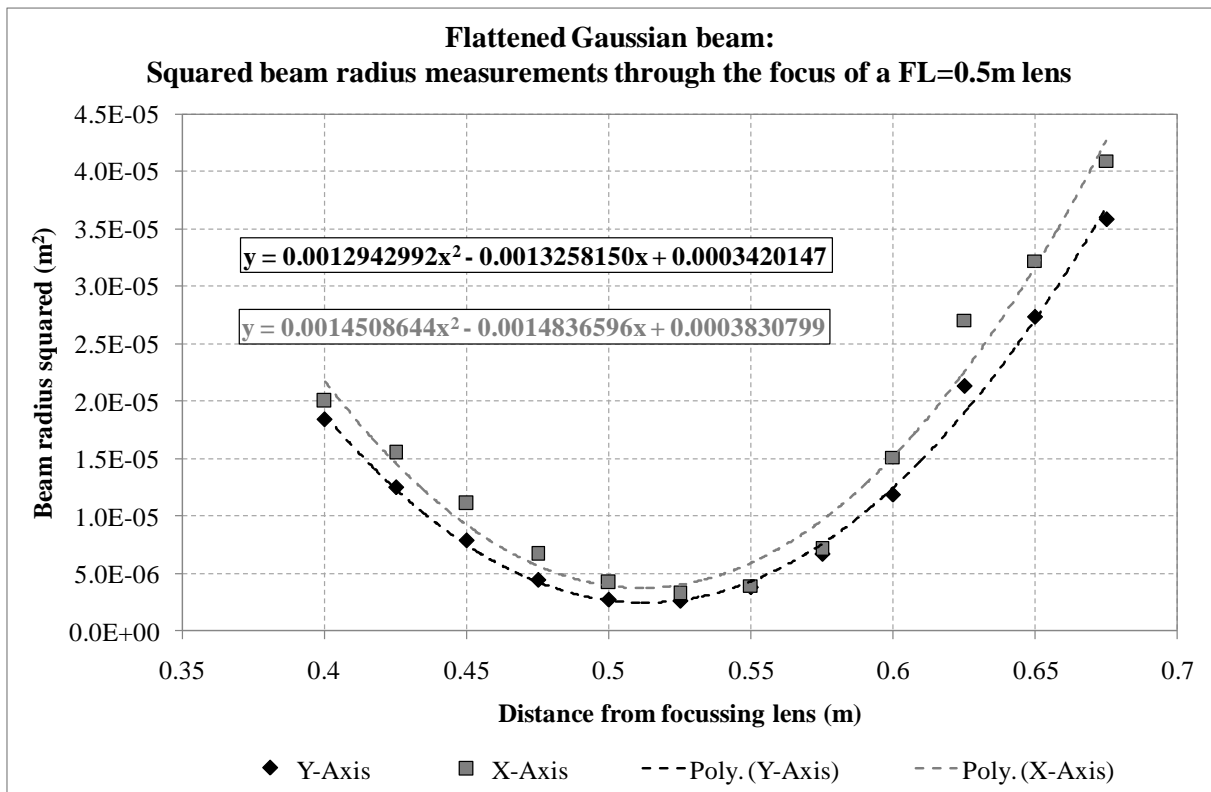


Figure 5-10 – Focused FGB beam size measurements

The Table 5-3 summarises the parameters of the beam for the FGB. The table presents the calculated M^2 parameters and the beam divergence as well as the pulse energy.

Parameter	X-Axis	Y-Axis
M^2 Parameter	22	16.8
Divergence	38.2mrad	35.9mrad
Pulse energy	5.3J	

Table 5-3 – FGB beam results

Figure 5-11 shows the far field image of the FGB beam. The image in Figure 5-12 represents the image of the FGB beam as it is at the output coupler of the laser. The far field image of the beam and the image of the beam as it is at the output coupler were once again obtained by following the procedure as outlined in Section 4.2.2. Once again the image of the beam in Figure 5-12 is inverted if compared to the image in Figure 5-11 due to the fact that the image was taken beyond the focal plane of the lens.

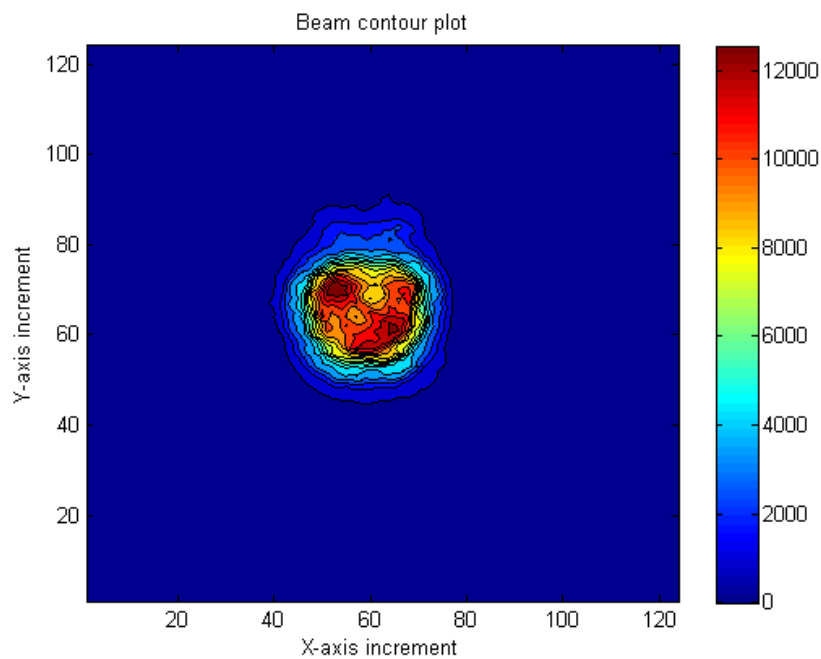


Figure 5-11 – FGB far field image

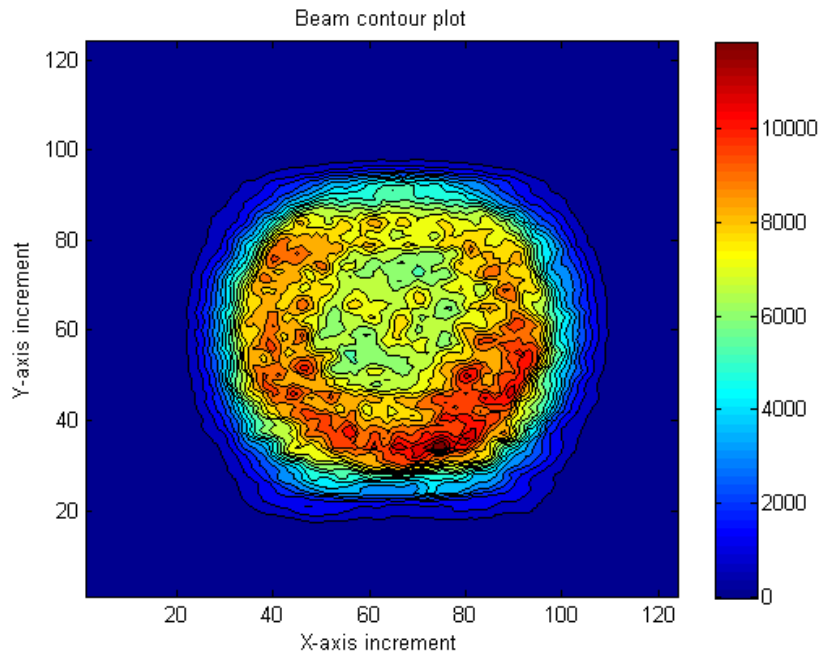


Figure 5-12 – FGB image at the output coupler

5.2.2 FGB results – aperture in gain volume

Following the previous measurements with the FGB an aperture was inserted into the laser resonator. The FGB was now generated by configuring the resonator as shown in Figure 5-13. In this configuration a flat output coupler and DOE gold coated copper mirror was used to form a stable long radius hemispherical optical resonator. A 30mm diameter aperture was inserted into the resonator at the DOE mirror side. In this configuration the laser yields an FGB. The insertion of the aperture in the resonator is similar to the work performed by Bélanger et al. (12), (13).

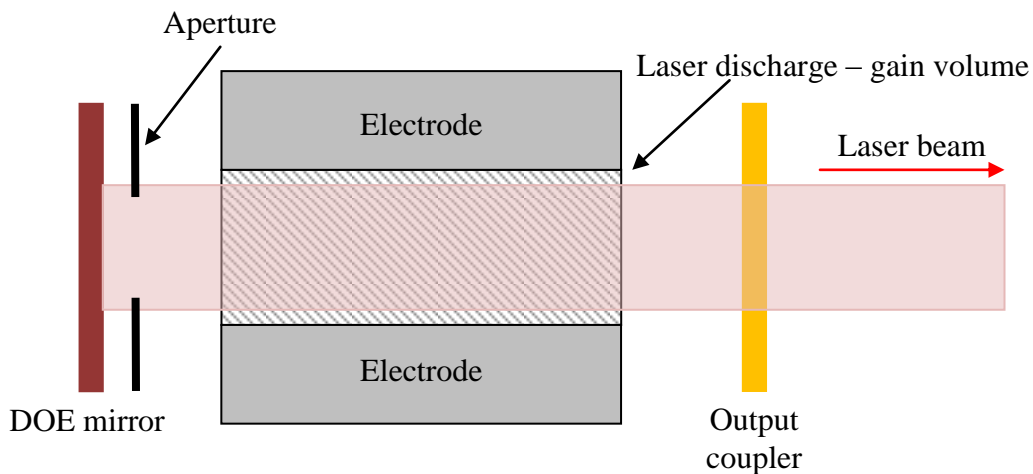


Figure 5-13 – FGB mode laser resonator with aperture

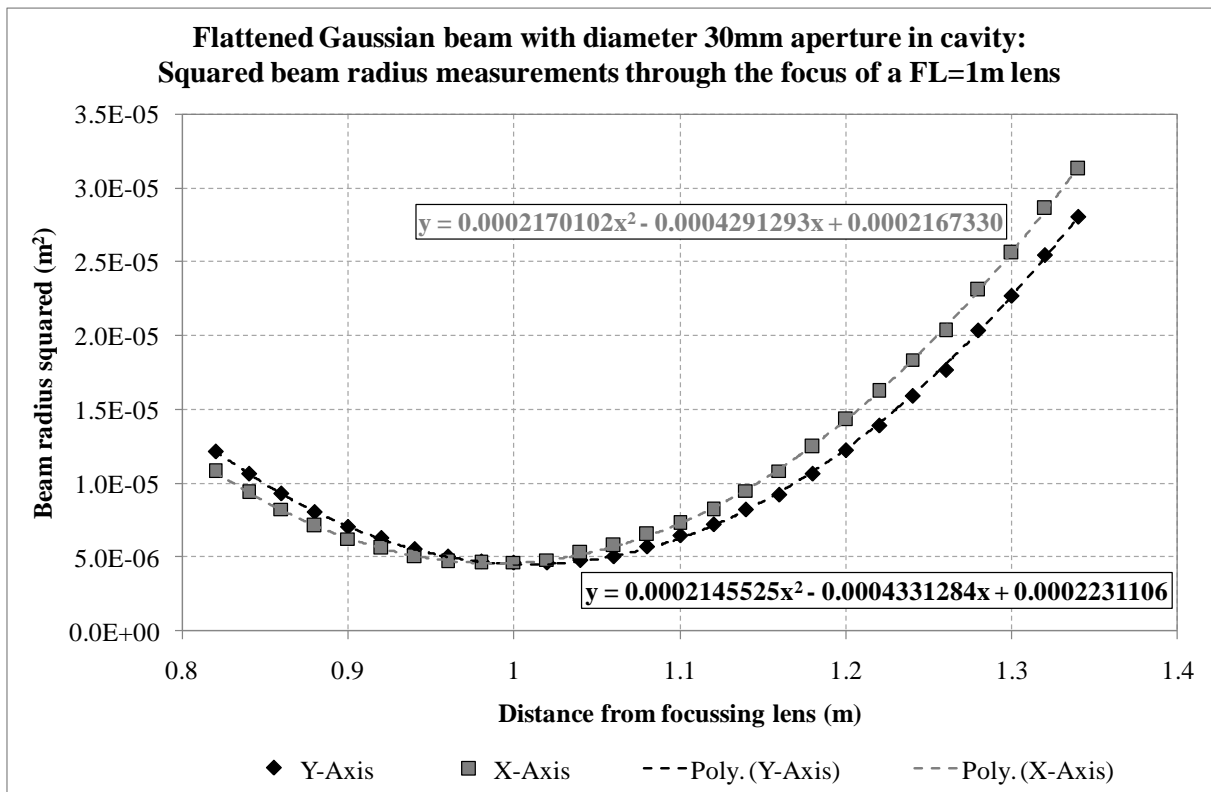


Figure 5-14 - Focused FGB beam size measurements

The beam propagation measurement as outlined in Section 4.2.3 was once again performed and the result is shown in Figure 5-14. From the data the M^2 parameter and beam divergence were determined. The Table 5-4 summarises the parameters of the beam for the aperture FGB. The table shows the determined M^2 parameters and the beam divergence for each axis as well as the laser pulse energy. The M^2 and divergence values for the FGB with an aperture in the gain volume are significantly lower than for the FGB with the open gain volume. This difference will be discussed in Section 6.1.3 where all the results are summarised and discussed.

Parameter	X-Axis	Y-Axis
M^2 Parameter	9.2	9.4
Divergence	7.3mrad	7.4mrad
Pulse energy	4.3J	

Table 5-4 - FGB beam results

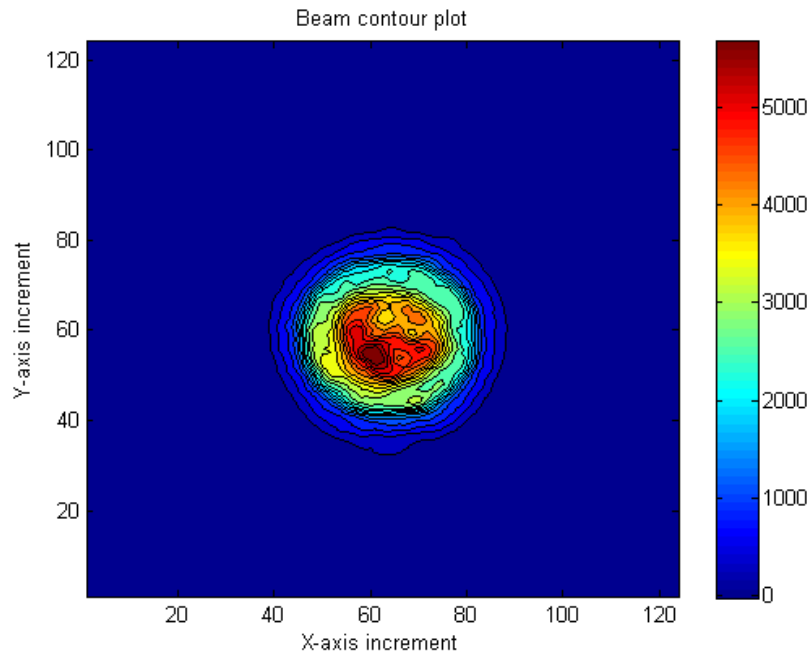


Figure 5-15 – FGB far field image

The image in Figure 5-15 shows the far field image of the FGB beam. The image was acquired using the method described in Section 4.2.2.

The reader is referred to Section 6.1.3 where the various beam characteristics will be summarised and discussed.

5.3 Paint removal results

Following the implementation of the DOE mirror in the laser resonator and the characterisation of the laser beam, the laser was used in a material processing application to test the properties of the beam. The material processing application for the laser is laser based paint removal from an aluminium substrate.

In the application of a TEA CO₂ laser for laser based paint removal it is desirable for the laser to have high pulse energy with good beam propagation properties and a uniform energy distribution profile for the beam. The high pulse energy and uniform energy distribution allow for maximum efficiency in the ablation process whereby the paint is removed from the substrate. The good beam propagation properties allow easy delivery and manipulation of the laser beam to get it to the paint removal target.

The laser beam characterisation that was performed in the previous paragraphs outline the characteristics for each beam of the TEA CO₂ laser. The TEM₀₀ beam has very good beam propagation characteristics which makes it excellent for propagation over long distances. Unfortunately it has low pulse energy and also has a Gaussian distribution in the energy distribution of the beam making it not ideal for uniform ablation. The reader is referred to Section 3.1 and Figure 3-1 where the disadvantages of the TEM₀₀ beam are illustrated. The multimode beam on the other hand has high pulse energy. The multimode beam energy distribution does approach a flat top type profile which is ideal for uniform ablation but the profile is, however, not uniform enough in the region where the flat energy distribution is required. Furthermore the beam propagation of the multimode beam is not ideal at all. The beam has very high divergence and is not suitable for propagation over long distances.

The FGB appears to be the best of both worlds. The FGB has good beam propagation properties making it ideal for propagation over long distances. The FGB furthermore has relatively high pulse energy and a uniform energy distribution in the beam profile. The FGB thus has all round good properties for uniform paint ablation from a substrate. The only downside of the FGB is the fact that the energy distribution of the beam changes shape as the beam propagates. The FGB must therefore be delivered and propagated via an image relay system to deliver it at the target in the desired flat top energy distribution profile.

Figure 5-16 and Figure 5-17 show the practical results of paint removal from an aluminium substrate using the TEA CO₂ laser. Both of the images show aluminium panels that were painted with two layers of primer and a final top coat. The first primer is yellow in colour and is barely visible in the paint removal results. The second primer has a green colour and is visible in the results. The top coat is white and is predominantly visible in the images.

The images shown in Figure 5-16 and Figure 5-17 were generated by holding the aluminium sample plate stationary and applying a given number of laser pulses at each point. The sample plate was then moved to a new position and the applied number of pulses was increased in the new application position. The process was repeated until enough pulses were applied to the substrate to remove all the paint. By looking at the irradiation spots on the aluminium samples the number of laser pulses was increased as the laser beam was moved from the left hand side of the sample to the right hand side. The irradiated areas on the left hand side of the sample show results where some of the top coat has been partially or completely removed. On these

areas the green primer is mostly still intact where the top coat has been completely removed. The irradiation areas in the centre of the sample show how the remnants of the top coat and the green primer are progressively removed. The irradiation areas on the right hand show the results where enough laser pulses have been applied so that all the paint is removed all the way down to the aluminium substrate.

From Figure 5-16 one can see that the multimode beam is effective in removing the paint from the substrate. From the figure it is visible that there are various regions in the multimode beam where the energy varies in intensity. The variation in energy intensity yields non-uniform paint ablation in the region where the beam is applied. The various modes that constitute the multimode beam are also visible in the ablation of the paint from the substrate as horizontal lines across the beam by looking at the figure. Looking at the vertical dimension of the beam there are also another two regions where the energy appears to vary. The vertical regions of higher energy intensity are believed to be due to the profile of the electrodes of the TEA CO₂ laser that enhances the field and hence the energy in these regions.

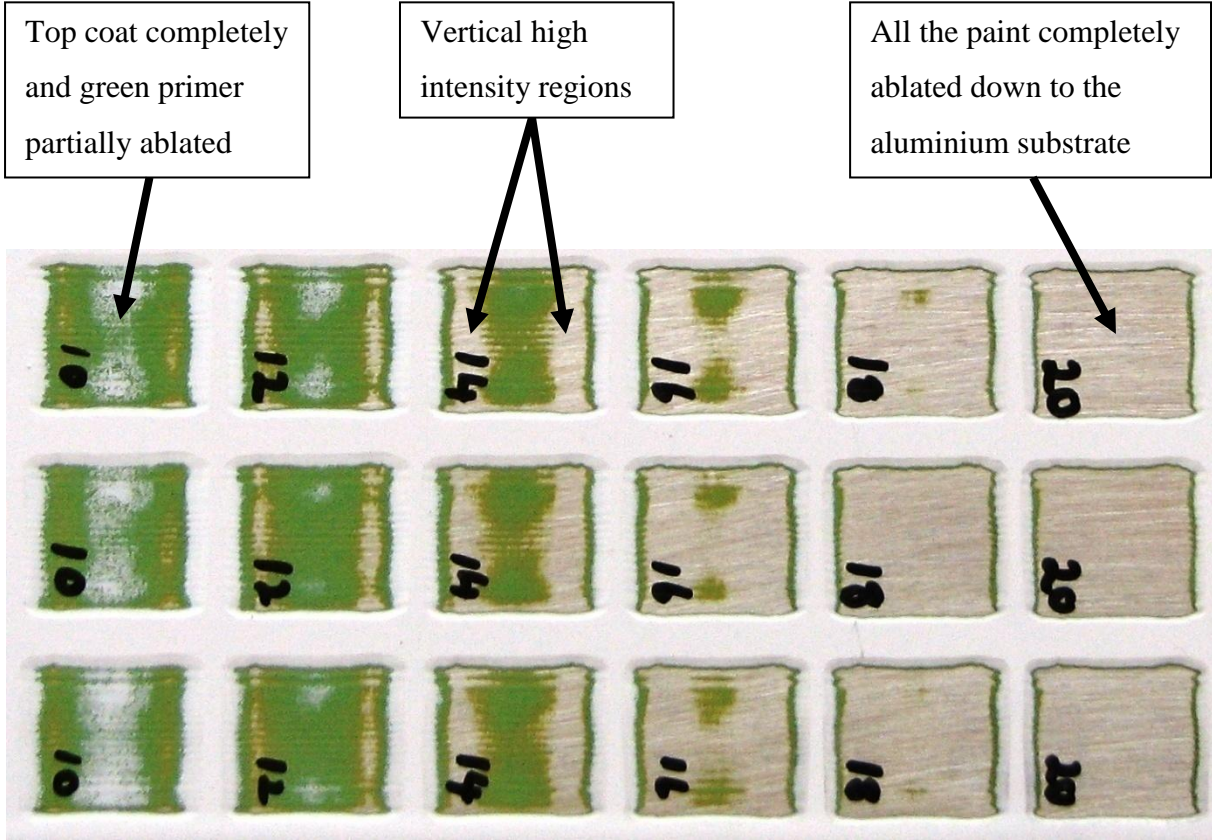


Figure 5-16 – Multimode paint removal results

The results shown in Figure 5-17 were generated in a similar fashion as those in Figure 5-16. In this case the FGB was, however, applied to the painted aluminium substrate. One can see from the figure that the FGB is also effective in removing paint from the substrate. The FGB shows better uniformity than the multimode beam which is evident through the more uniform ablation of the paint. There are still some small non-uniformities but they are not as significant in the multimode case.

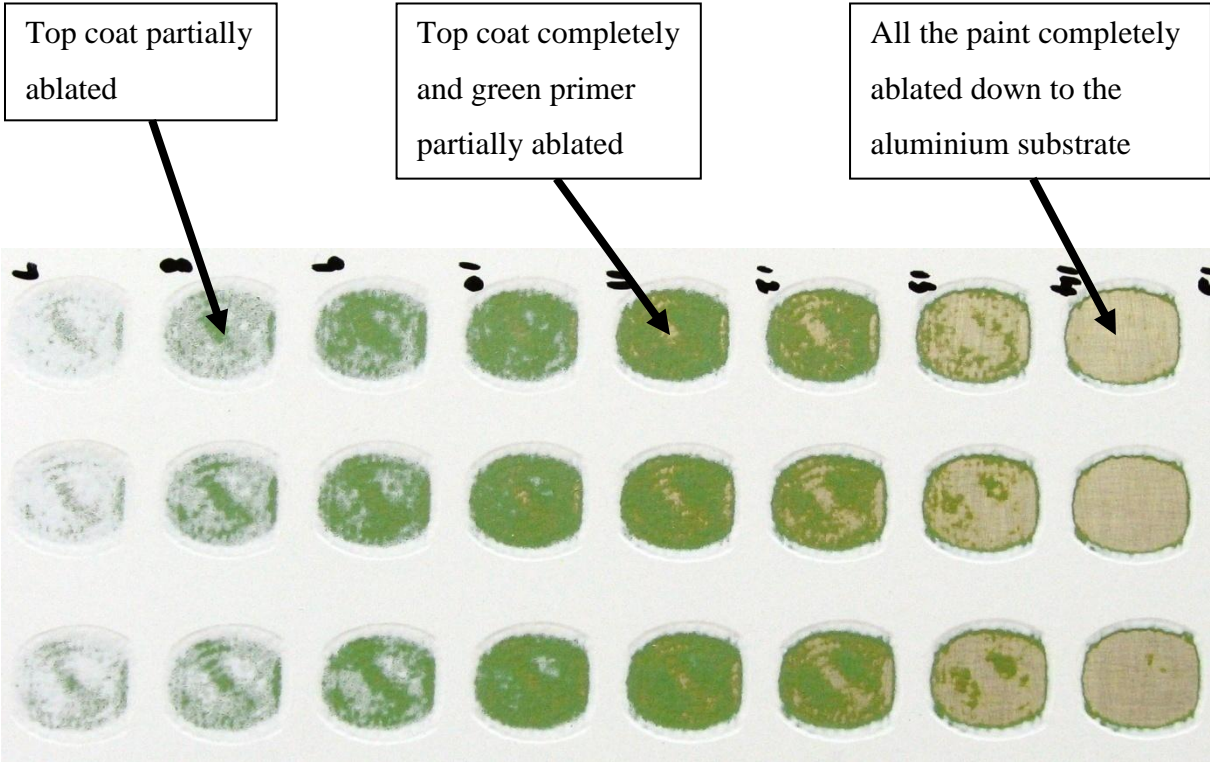


Figure 5-17 – FGB paint removal results

The SDI Lasers WH1500 laser with the FGB was finally integrated into an automated robotic paint removal system. The paint removal system consists of the WH1500 laser, the beam launch assembly, the articulated arm assembly, the paint removal head and the industrial robot arm. The laser beam exits the laser and propagates through the beam launch assembly to the entry point of the articulated arm. The beam continues through the articulated arm and enters the paint removal head. The beam finally propagates through the paint removal head and exits through the nozzle of the head. The surface from which the paint is to be removed is situated in front of the nozzle of the head. The paint removal head is connected to the tool connection point of the industrial robot arm. The industrial robot arm manipulates the paint

removal head over the target surface. The WH1500 laser and the first part of the beam delivery system are shown in Figure 5-18.

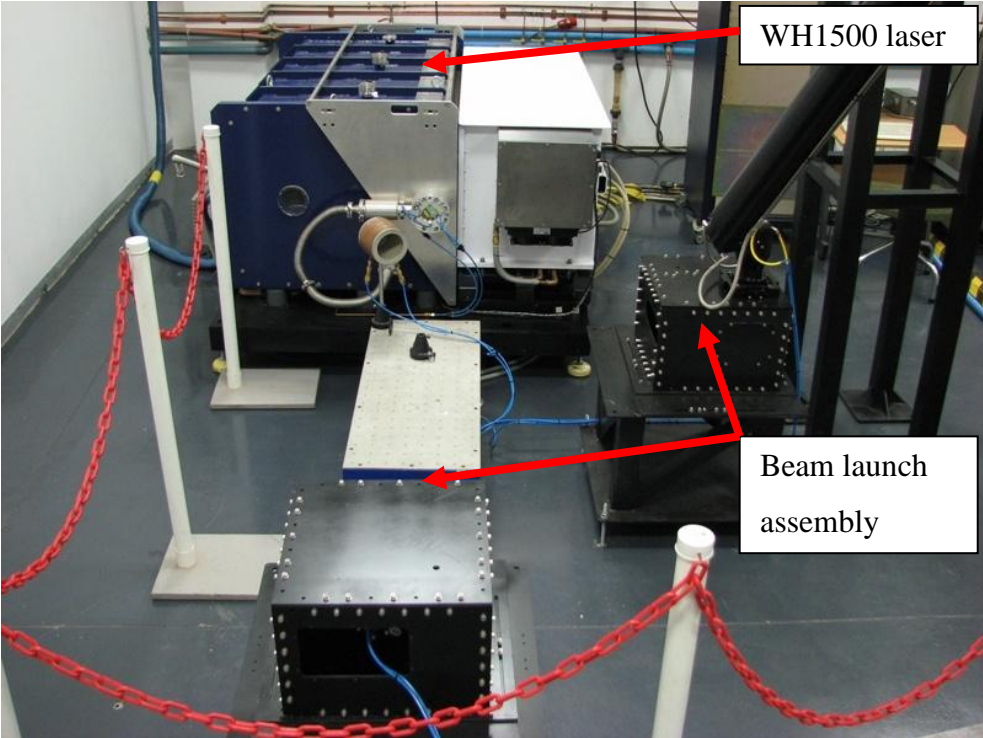


Figure 5-18 - WH1500 TEA CO₂ laser and beam delivery system

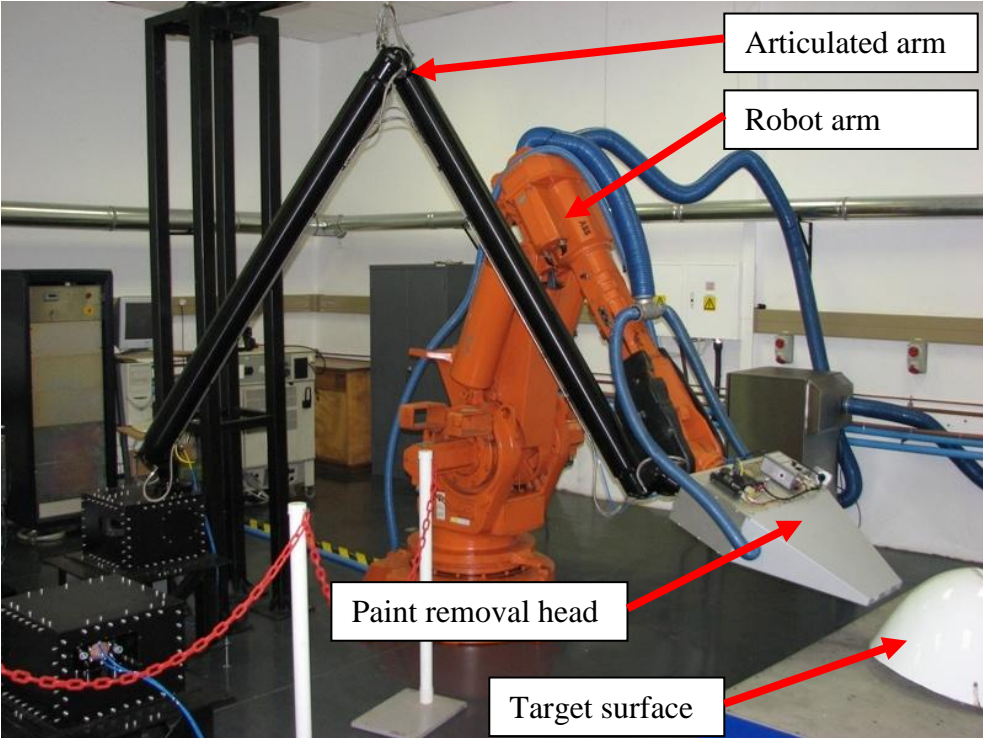


Figure 5-19 - The beam delivery system with the industrial robot arm

The images Figure 5-20 show the paint removal system in operation where paint is being removed from a large aluminium plate that is placed in front of the paint removal head.



Figure 5-20 - Paint removal system in operation

6 CONCLUSIONS, SUMMARY AND RECOMMENDATIONS

6.1 Conclusion

This thesis started off by discussing the application of Gaussian beams in laser materials processing applications. The Gaussian intensity distribution of the beam was identified to be non-ideal in applications where a homogenous energy distribution in the beam is required. The topic of SGBs and FGBs was introduced as these laser beams have more uniform intensity distributions than the Gaussian beam. The purpose of this thesis was to investigate the concept of FGBs and how an FGB could be practically implemented on a TEA CO₂ laser for the purpose of laser-based paint removal. Conclusions will be drawn in the following sections about the theory of FGBs as investigated in this thesis and the methodology for implementing an FGB. The resulting FGB and its properties as implemented on the TEA CO₂ laser will be discussed. Finally the laser based paint removal application will be discussed and a conclusion drawn on the application of flattened irradiance profile beams in materials processing applications.

6.1.1 FGB theory

In Section 3.1 the concept of flattened irradiance profile beams was presented. The flattened irradiance profile beam can be treated mathematically in various ways as described by the referenced authors. For the purpose of this study the FG profile for defining the profile of the flattened irradiance profile beam as introduced by Gori (3) was chosen. The mathematical description of the FG profile as presented in (3) was studied. Furthermore the propagation of the FGB with circular symmetry was analysed using an analytical method. Following this, the work of Amarande (4), (5) was studied where FGBs with rectangular symmetry was mathematically described and propagated using an analytical method. This study of the background theory of FGBs laid the fundamentals for proceeding in designing a laser resonator that naturally yields an FGB.

The topic of laser beam shaping was then introduced. Laser beam shaping techniques can be applied to laser beams externally or internally to the laser resonator. The method of internal beam shaping is preferred in this application. The high envisaged average output power of the laser and elegance of shaping the beam internally to the resonator makes this the only viable option for implementing an FGB. For this purpose the work of Bélanger et al. (8), (9), and (10) involving custom laser resonators with GPM mirrors was studied. The design procedure

for a custom resonator implementing a DOE or GPM as outlined by Bélanger et al. was studied. Finally the method of Fox and Li (14) for determining the steady-state condition in a resonator was studied.

6.1.2 FGB implementation

Following the study of the background theory, the theoretical concepts were put into practice. Section 4.1 outlines the custom laser resonator with the design of the DOE mirror for the resonator. The solution of the Kirchhoff-Fresnel diffraction integral for the numerical propagation of the beam was performed in Section 4.1.1. The numerical solution for the beam propagation was compared to the analytical solution. From the results it can be seen that there is a difference between the numerical and analytical results. It is assumed that the analytical method makes an approximation of the beam propagation through the analytical technique that was used. The results of the numerical propagation are believed to be more accurate and this method was used in propagating the beam during the design of the custom resonator.

The design of the resonator and DOE mirror was performed in Section 4.1.2. This section shows the specified output FGB as well as the beam profile and phase at the DOE mirror. The beam profile and phase at the DOE mirror was used to determine and design the DOE mirror profile. Finally the resulting mirror profile was shown in Figure 4-8. A stability analysis was performed in Section 4.1.3 to determine the steady-state condition of the laser resonator. The stability analysis was performed as a check to confirm that the resonator does produce an FGB. For the analysis of the resonator a starting field of background noise was introduced into the resonator and propagated back and forth between the output coupler and the DOE mirror. The results of the stability analysis showed that the resonator did converge to a steady-state solution where an FGB was formed in the resonator. From the stability analysis it could be seen that a stable mode had formed after approximately 100 round trips. From the results it can be seen that the resulting beam does not look exactly like the beam that was used to design the resonator. This can be attributed to the finite calculation accuracy of the design and simulation. The resulting beam profile from the resonator starting from the noise input field showed good agreement with the profile of the case where the starting field was an FGB. It is therefore concluded that the resonator will converge to a stable mode as determined by the profile of the DOE mirror in the resonator. Experimental testing showed that the laser gain life time for the TEA CO₂ laser is in the order of 4 μ s. This allows for approximately 338 round trips in this laser which will be sufficient time for the stable mode to form.

The methodology of characterising a laser beam was investigated and discussed in Section 4.2. The practicalities of measuring the laser beam profile with an IR camera were treated in Section 4.2.2. The measuring and determining of the laser beam propagation parameters were discussed in Section 4.2.3. In the characterisation of the beam the IR camera was used to measure the beam size at various positions in the beam to determine the propagation parameters such as the M^2 parameter and beam divergence value.

6.1.3 FGB results

The experimental results as obtained from the SDI Lasers WH1500 TEA CO₂ laser was presented in Chapter 5. For the purpose of contrasting the FGB to the multimode and TEM₀₀ beams of the laser, the propagation parameters of the multimode and TEM₀₀ beams were determined first. Following this the FGB results for the scenario of the open gain volume were measured. The result for the FGB in a scenario where an aperture was installed in the gain volume was finally measured.

Parameter:	Multimode		TEM₀₀		FGB		Aperture FGB	
Axis:	X	Y	X	Y	X	Y	X	Y
M^2 Parameter	21.3	28.7	1.06	1.08	22	16.8	9.2	9.4
Divergence (mrad)	35.3	41.8	7.7	7.8	38.2	35.9	7.3	7.4
Pulse energy (J)	6.3		0.25		5.3		4.3	

Table 6-1 - Summary of laser beam parameters

The measured beam propagation results for the various beams of the WH1500 laser are summarised in Table 6-1. The multimode beam yields the highest pulse energy and also has the highest M^2 parameter and beam divergence of all the beams. The high M^2 parameter and beam divergence values do not make the multimode beam suitable for propagation over long distances. The TEM₀₀ beam gave the lowest pulse energy but had the best beam propagation parameters. Both the M^2 parameter and beam divergence values are very low and make the beam excellent for propagation over long distances. The open aperture FGB yielded comparatively high pulse energy but has M^2 parameter and beam divergence values that are only marginally better than those of the multimode beam. The FGB with the aperture gave somewhat lower pulse energy than the open aperture FGB, but on the other hand exhibited vastly improved propagation parameters.

The M^2 parameter and beam divergence values of the multimode and open aperture FGB are virtually the same. This is due to the fact that the DOE mirror is exposed to the entire gain volume of the resonator. The gain volume is larger than the FGB and this gives way to the fact that the DOE mirror partially functions as a phase selective mirror and partially as a conventional spherical mirror in the resonator. Due to the unrestricted gain volume, higher order modes also contribute towards the FGB. The higher order modes result in the unrestricted FGB also having similar propagation parameters to the multimode beam. Therefore the M^2 and beam divergence parameters are very similar.

In the instance where the aperture is installed in the resonator together with the DOE mirror, the DOE mirror is not exposed to the entire gain volume. In this instance the FGB truly has a single mode. The absence of the higher order modes in the beam bring about the improvement in M^2 parameter and beam divergence values that are visible in the results of the FGB with the aperture in the resonator.

Laser beams with high pulse energy and good propagation parameters are desired for materials processing applications. The FGB with the aperture installed in the resonator exhibits these desired properties. The beam has sufficient energy for the materials processing application and has good beam propagation parameters that are suitable for propagation of the beam over long distances.

From Table 6-1 the conclusion can be drawn that the monomode FGB extracted significantly more energy from the cavity than the monomode TEM_{00} beam. In the case where the DOE mirror was exposed to the entire gain volume the output pulse energy was approximately 85% of the multimode pulse energy. For the instance where an aperture was placed between the gain volume and the DOE mirror the output pulse energy was approximately 68% of the multimode pulse energy. In contrast the pulse energy of the TEM_{00} beam was only 4% of the energy of the multimode beam. The high energy extraction and the good beam propagation properties of the monomode FGB make it a lucrative beam option for materials processing.

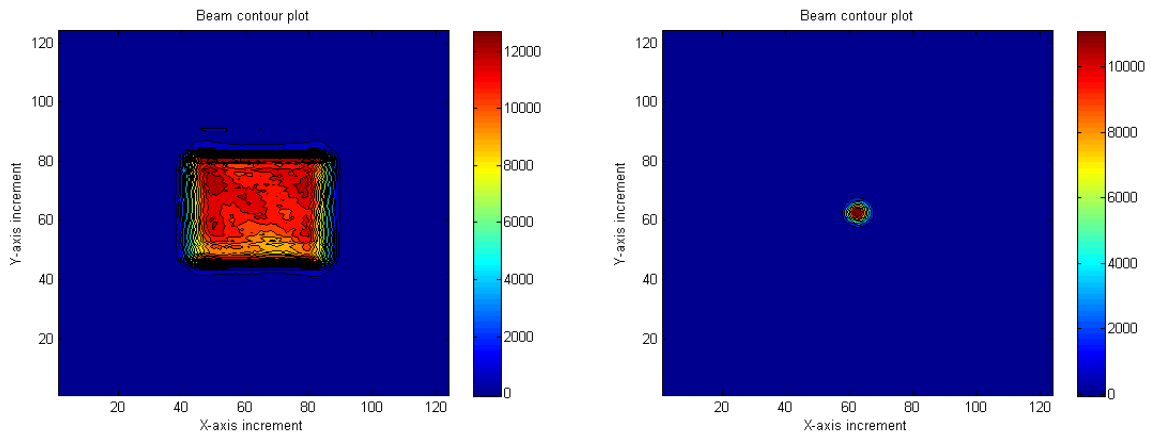


Figure 6-1 - Far field images of the multimode beam (left) and TEM₀₀ beam (right)

For the sake of the discussion here the far field images of the various beams of Section 5.2 are repeated in Figure 6-1 and Figure 6-2. In Figure 6-1 the multimode beam is shown on the left hand side and the TEM₀₀ beam is shown on the right hand side. The WH1500 TEA CO₂ laser has a rectangular gain area. From the image of the multimode beam it can be seen that the multimode beam fills the gain area completely and hence the rectangular shape of the multimode beam. In the horizontal axis of the beam there are various features visible (Figure 6-1). This can mainly be attributed to the diffraction effects of the electrodes in the laser. To obtain the TEM₀₀ beam an aperture was installed in the resonator. The aperture restricted the resonator to use only the amount of gain area that is visible through the opening of the aperture. In order to obtain the monomode TEM₀₀ beam a small aperture must be installed. Most of the gain area is therefore not used in this configuration. This then yields the small beam and low pulse energy. With reference to Figure 6-1 the beam has a Gaussian intensity distribution which is visible despite the fact that the beam was quite small on the detector.

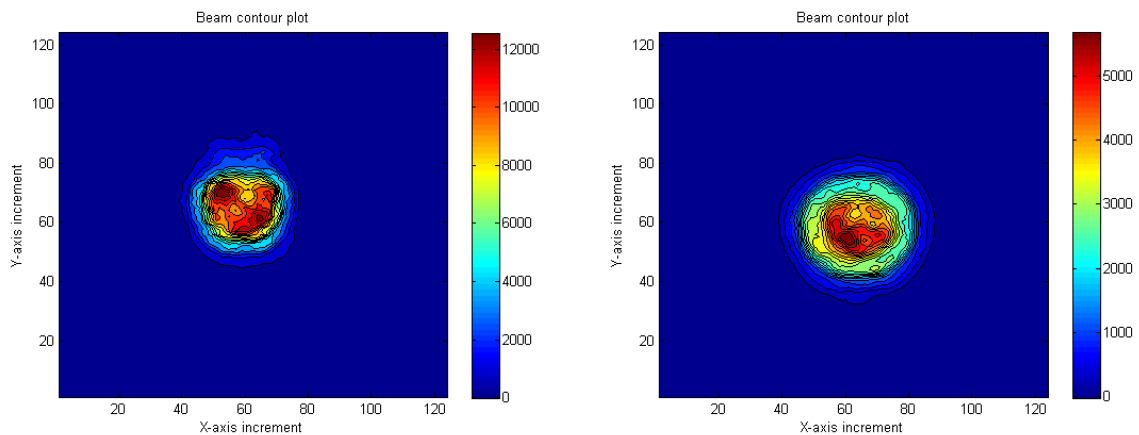


Figure 6-2 - Far field images of the open aperture FGB (left) and apertured FGB (right)

In Figure 6-2 the far field image of the open aperture FGB is shown on the left hand side and the far field image of the FGB with the aperture is shown on the right hand side. In the case of the open aperture FGB the beam tends towards a flattened irradiance profile but some imperfections are visible in the beam. The imperfections can be attributed to the fact that the DOE mirror is exposed to the entire gain area and that higher order modes can also be generated through this. As in the case of the multimode beam there are also some diffraction effects of the electrodes visible in this beam. Furthermore the beam is also not completely circular. The FGB that was generated by inserting an aperture in front of the DOE mirror on the other hand appears to yield a truly monomode beam. The intensity profile truly approximates a flattened irradiance profile. The beam is also circular with no major diffraction effects in the beam.

6.1.4 Paint removal results

The WH1500 laser was finally applied in a materials processing application where paint was removed from an aluminium substrate. For the basis of comparison the laser was applied in the multimode beam case to the substrate and following this in the FGB case to the substrate. The images of the paint removal results are repeated here in Figure 6-3 for the reader’s convenience. The multimode beam paint removal is shown on the left-hand side and the FGB paint removal is shown on the right-hand side. The details of the results and how they were obtained were discussed in Section 5.3 and will not be repeated here.

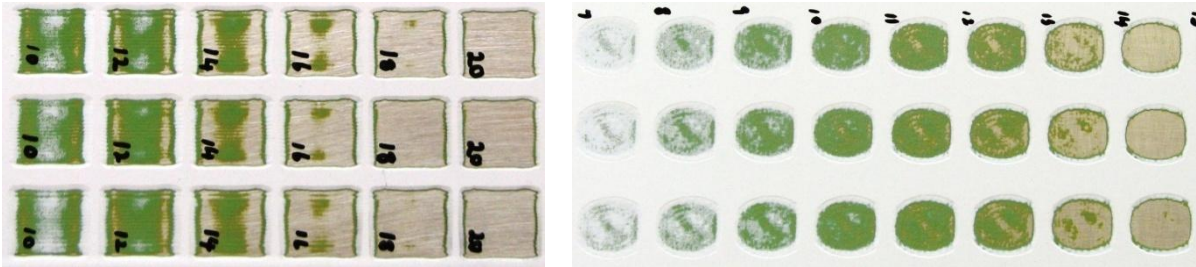


Figure 6-3 - Multimode beam (left) and FGB (right) paint removal results

In conclusion both the multimode and FGB beams are suitable for removing paint from a substrate. The multimode beam varies in energy intensity across the profile of the beam due to the multimode content of the beam. The vertical higher intensity regions which are believed to be due to the profile of the electrodes also contribute towards the energy intensity variations. The variation in energy intensity across the profile of the beam is evident in the

paint removal results that are shown in Figure 6-3. The uneven ablation of the paint from the substrate can clearly be seen. The FGB shows improved uniformity in the energy intensity across the profile of the beam. The improved uniformity of ablation of the paint is evident in the results shown in Figure 6-3. The improved beam propagation of the FGB facilitated that the beam could be propagated over a long distance through the complete beam delivery system to the paint removal head assembly as shown in Figure 5-18 and Figure 5-19. With the multimode beam it would not have been possible to deliver the beam through the envisaged beam delivery system.

The results in Figure 5-16, Figure 5-17 and Figure 6-3 show the paint removal results with the multimode beam and the open aperture FGB beam. The aperture FGB results were not available for inclusion in this thesis. Paint removal tests with the aperture FGB did, however, exhibit further improvements in the uniformity of the energy intensity across the beam profile. Improved uniform paint ablation could be seen as a result of this and the aperture FGB is currently implemented in the paint removal system.

6.2 Summary

This thesis studied the theory of FGBs and the custom laser resonators that are required to shape the beam internally to be an FGB. A custom laser resonator for a TEA CO₂ laser was designed for the purpose of generating an FGB from the laser. The custom resonator was implemented on the laser and the resulting FGB was analysed and compared to the conventional multimode and TEM₀₀ beam scenarios. The resulting FGB was finally implemented in a materials processing application where the application of the FGB was successfully demonstrated. Compared to the multimode beam, the FGB yielded the desired improvements in the beam propagation parameters and also in the uniformity of the energy intensity across the beam. The theory, design and application of FGBs were therefore successfully demonstrated in a real-life industrial application.

6.3 Recommendations

In the application of laser-based paint removal it is generally required that large surface areas must be stripped of paint in a realistic timeframe to make the process economically viable. The paint removal process can be improved by increasing the energy per pulse of the laser and by increasing the repetition rate of the laser. In the implementation of the FGB it is evident that some of the energy that is present in the multimode beam is lost due to the fact that the FGB has a circular profile. Approximately 25% to 32% of the energy of the

multimode beam is lost due to this fact. In the science and engineering of lasers a great deal of effort is expended to generate the laser output energy. The capital cost of the laser almost scales quadratic in terms of the output power of the laser. It is therefore counterproductive to not utilise the complete gain area. The output efficiency of the system is decreased if the entire gain area of the laser is not used as in the case of the circular FGB implementation.

It is therefore recommended that the possibility of implementing a rectangular FGB in the TEA CO₂ laser should be investigated. In the implementation of the DOE mirror to generate a rectangular FGB it is envisaged that almost the entire gain area of the laser will be utilised. It might be necessary to add a rectangular aperture to the resonator but in essence most of the gain area will be utilised. If the rectangular FGB could be realised it would still have the improved propagation properties that are also desired. The manufacturing and the alignment of the DOE mirror for the rectangular FGB might pose some technical challenges that need to be addressed in the implementation. It will be required to properly align the DOE mirror with the vertical axis and horizontal axis of the resonator with reference to the placement of the electrodes in the resonator.

If the technical challenges of implementing the rectangular FGB could be overcome it would be a viable option for improving the pulse energy of the laser. The pulse energy can also be improved by staying with the circular FGB but increasing the size of the beam and hence the gain area of the laser.

7 REFERENCES

1. **Shealy, D.L. and Hoffnagle, J.A.** Laser beam shaping profiles and propagation. *Applied Optics*. 20 July 2006, Vol. 45, 21, pp. 5118-5131.
2. **De Silvestri, S., Laporta, P., Magni, V., Svelto, O. and Majocchi, B.** Unstable laser resonators with super-Gaussian mirrors. *Optics Letters*. 1988, Vol. 13, 3, pp. 201-203.
3. **Gori, F.** Flattened gaussian beams. *Optics Communications*. 1 May 1994, Vol. 107, pp. 335-341.
4. **Amarande, S.-A.** Beam propagation factor and the kurtosis parameter of flattened Gaussian beams. *Optics Communications*. 1 September 1996, Vol. 129, 5-6, pp. 311-317.
5. **Amarande, S.-A.** Approximation of super-Gaussian beams by generalized flattened Gaussian beams. *Proceedings of SPIE*. 1997, Vol. 3092, pp. 345-348.
6. **Dickey, F.M. and Holswade, S.C.** *Laser Beam Shaping - Theory and Techniques*. New York : Marcel Dekker, 2000.
7. **Zeitner, U.D., Aagedal, A. and Wyrowski, F.** Comparison of resonator-originated and external beam shaping. *Applied Optics*. 20 February 1999, Vol. 38, 6, pp. 980-986.
8. **Paré, C. and Bélanger, P.A.** Optical resonators using graded-phase mirrors. *Optics Letters*. 15 July 1991, Vol. 16, 14, pp. 1057-1059.
9. **Paré, C. and Bélanger, P.A.** Custom laser resonators using graded-phase mirrors. *IEEE Journal of Quantum Electronics*. 1992, Vol. 28, 1, pp. 355-362.
10. **Bélanger, P.A.** Beam propagation and the ABCD ray matrices. *Optics Letters*. 15 February 1991, Vol. 16, 4, pp. 196-198.
11. **Leger, J.R., Chen, D. and Wang, Z.** Diffractive optical element for mode shaping of a Nd:YAG laser. *Optics Letter*. 15 January 1994, Vol. 19, 2, pp. 108-110.
12. **Bélanger, P.A., Lachance, R.L. and Paré, C.** Super-Gaussian output from a CO₂ laser by using a graded-phase mirror resonator. *Optics Letters*. 15 May 1992, Vol. 17, 10, pp. 739-741.
13. **Van Neste, R., Paré, C., Lachance, R.L. and Bélanger, P.A.** Graded-Phase Mirror Resonators with a Super-Gaussian Output in a CW-CO₂ Laser. *IEEE Journal of Quantum Electronics*. November 1994, Vol. 30, 11, pp. 2663-2669.
14. **Fox, A.G. and Li, T.** Resonant modes in a maser interferometer. *The Bell System Technical Journal*. March 1961, Vol. 40, pp. 453-488.

15. **Mathews, J.H.** *Numerical Methods for Mathematics, Science and Engineering*. Englewood Cliffs : Prentice-Hall, Inc, 1992.
16. **Solms, F.** *Computational Methods for Science and Engineering with C++ Implementations*. Johannesburg : Rand Afrikaans University, 1998.
17. **Rypma, R.** Fundamentals of Photonics: Laser Beam Characterization. *Laser Focus World Web Cast*. February 2010.
18. **Roundy, C.** Propagation factor quantifies laser beam performance. *Laser Focus World*. 1 December 1999.
19. **Spiricon Inc.** Laser Measurement Instruments - Spiricon Beam Profilers - Tutorials. *Ophir Spiricon - Laser Measurement Instruments*. [Online] [Cited: 27 03 2010.] <http://www.ophir-spiricon.com/laser-measurement-instruments/beam-profilers/knowledge-center/tutorial>.
20. **Spiricon Inc.** *Operators Manual - Version 4.xx - Laser Beam Analyzer*. Logan : Spiricon Inc., 2005.
21. **Forbes, A.** Back to basics: Measuring Laser Beams. *African Laser Centre Course: Introduction to Laser Beams*. March 2009.
22. **International Organisation for Standardisation.** Test methods for laser beam widths, divergence angles and beam propagation ratios. 2005. ISO 11146.
23. **Siegman, A.E.** *Lasers*. Mill Valley, CA : University Science Books, 1986.
24. **Svelto, O.** *Principles of lasers*. New York : Plenum Press, 1998.
25. **Hoffnagle, J.A. and Jefferson, C.M.** Design and performance of a refractive optical system that converts a Gaussian to a flattop beam. *Applied Optics*. 20 October 2000, Vol. 39, 30, pp. 5488-5499.
26. **Li, Y.** Light beams with flat-topped profiles. *Optics Letters*. 2002, Vol. 27, 12, pp. 1007-1009.
27. **Li, Y.** New expressions for flat-topped light beams. *Optics Communications*. 1 June 2002, Vol. 206, 4-6, pp. 225-234.
28. **Morse, P M and Feshbach, H.** *Methods of Theoretical Physics*. New York : McGraw-Hill, 1953. Vol. 1, ch. 5.
29. **Siegman, A. E., Bélanger, P. A. and Hardy, A.** "Optical Resonators Using Phase Conjugate Mirrors" in *Optical Phase Conjugation*. [ed.] R.A. Fisher. New York : Academic Press, 1983.

30. **Paré, C, and Bélanger, P.A.** Custom Laser Resonators Using Graded-Phase Mirrors: Circular Geometry. *IEEE Journal of Quantum Electronics*. April 1994, Vol. 30, 4, pp. 1141-1148.
31. **Du Preez, N.C., Forbes, A. and Botha, L.R.** High power infrared super-Gaussian beams: generation, propagation and application. *Proceedings of SPIE*. 2008, Vol. 7131.
32. **Forbes, A.** Laser beam propagation in non-linearly absorbing media. *Proc. of SPIE*. 2006, Vol. 6290.
33. **Forbes, A., Strydom, H.J., Botha, L.R. and Ronander, E.** Beam delivery for stable isotope separation. *Proceedings of SPIE*. 2002, Vol. 4770, pp. 13-27.
34. **Siegman, A. E., Nemes, G. and Serna, J.** How to (Maybe) Measure Laser Beam Quality. *DPSS (Diode Pumped Solid State) Lasers: Applications and Issues, OSA Trends in Optics and Photonics*. 1998, Vol. 17.

8 APPENDICES

8.1 MATLAB program

```
%%%% CLEAR THE VARIABLES
clear all;
clear function;

%%%% INITIALISE THE VARIABLES
A = -0.015;           % initialise lower integration limit
B = 0.015;           % initialise upper integration limit
wo = 0.01;           % beam waist
wave = 0.0000106;    % wavelength
kk = 2*pi/wave;      % propagation constant
L = 1.772;           % resonator length
b = L;
s = A;               % initialise the s variable for the integration over
the beam
steps = 5e-6;        % step size of s
sind = 1;            % index of s
resultvar = 0;
ss = 0;
Io = 1;              % super-Gaussian amplitude scale factor
N = 10;              % super-Gaussian order parameter
numofpasses = 500;  % number of passes for the stability analysis must be
an EVEN number!
sarr(1) = double(0);

sindmax = (B-A)/steps + 1;
for sind = 1:sindmax, sarr(sind) = A + steps*(sind-1); end
csvwrite('s-array.csv',sarr);

%%%% GENERATE THE FGB FUNCTION FOR PROPAGATION
for sind = 1:sindmax, fgbfield(sind) = fgbfunc(Io,sarr(sind),wo,N,wave);
end
csvwrite('fgbfield amp.csv',abs(fgbfield));
csvwrite('fgbfield angle.csv',angle(fgbfield));

%%%% CALCULATE THE MIRROR PHASE AND SURFACE PROFILE
for sind = 1:sindmax
    h = steps;
    sum = 0;
    for k = 2:(sindmax-1)
        sum = sum + sqrt(j/(wave*L))*fgbfield(k)*exp((( -
j*pi)/(wave*L))*power((A+(k-1)*h)-sarr(sind),2));
    end
    fa = sqrt(j/(wave*L))*fgbfield(1)*exp((( -j*pi)/(wave*L))*power(A-
sarr(sind),2));
    tempmax = cast(sindmax,'int16');
    fb = sqrt(j/(wave*L))*fgbfield(tempmax-1)*exp((( -
j*pi)/(wave*L))*power(B-sarr(sind),2));
    resultvar(sind) = h*((fa+fb)/2 + sum);
end
csvwrite('fieldatmirror.csv',abs(resultvar));
csvwrite('phaseatmirror.csv',angle(resultvar));
sprintf('%s','Mirror surface and phase determined')
```

```

%%%% DETERMINE THE MIRROR PHASE FOR THE RESONATOR ANALYSIS TEST
tfunc = conj(resultvar)./resultvar;

%%%% GENERATE AN ARBITRARY FIELD FOR THE START OF THE RESONATOR STABILITY
%%%% ANALYSIS
%for sind = 1:sindmax, startfield(sind) =
fgbfunc(0.1,sarr(sind),0.005,1,wave); end
for sind = 1:sindmax, startfield(sind) = rand; end % create random start
field
csvwrite('startfield amp.csv',abs(startfield)); % output the start
field amplitude to a *.csv file
csvwrite('startfield angle.csv',angle(startfield)); % output the start
field phase to a *.csv file

%%%% PROPAGATE THE BEAM BACK AND FORTH THROUGH THE RESONATOR FOR THE
%%%% SPECIFIED NUMBER OF PASSES
for passind = 1:numofpasses
% Select the right field to be propagated for the next round trip
if passind == 1
propfield = startfield;
else
propfield = nextfield;
end

for sind = 1:sindmax
h = steps;
sum = 0;
for k = 2:(sindmax-1)
p = sqrt(b*b+power((A+(k-1)*h)-sarr(sind),2));
sum = sum +
((exp(j*(pi/4)))/(2*sqrt(wave)))*propfield(k)*((exp(-
j*kk*p))/sqrt(p))*(1+b/p);
end
p = sqrt(b*b+power(sarr(1)-sarr(1),2));
fa = ((exp(j*(pi/4)))/(2*sqrt(wave)))*propfield(1)*((exp(-
j*kk*p))/sqrt(p))*(1+b/p);
p = sqrt(b*b+power(sarr(tempmax-1)-sarr(tempmax-1),2));
fb = ((exp(j*(pi/4)))/(2*sqrt(wave)))*propfield(tempmax-1)*((exp(-
j*kk*p))/sqrt(p))*(1+b/p);
nextfield(sind) = h*((fa+fb)/2 + sum);
end

%if rem(passind,2) == 0
filename1 = strcat('amplitude',int2str(passind), '.csv');
csvwrite(filename1,abs(nextfield));
%end

% Add the phase of the doe mirror for reflections from the DOE mirror
if rem(passind,2) ~= 0
amplitude = abs(nextfield);
theta = angle(nextfield);
nextfield = nextfield.*tfunc;
end

sprintf('%s %d','Resonator pass number',passind)
end

%%%% PLOT THE FGB AT THE OUTPUT COUPLER
intensityla = abs(fgbfield);
phasel = angle(fgbfield);
figure(1);

```

```

plot(sarr,intensity1a);
xlabel('x (m)');
ylabel('Amplitude (a.u.)');
title('Beam amplitude at OC');
figure(2);
plot(sarr,abs(phase1));
xlabel('x (m)');
ylabel('phase (rad)');
title('Beam phase at OC');

%%% PLOT THE BEAM AT THE DOE MIRROR
figure(3);
intensity2a = abs(resultvar);
phase2 = angle(resultvar);
plot(sarr,intensity2a);
xlabel('x (m)');
ylabel('Amplitude (a.u.)');
title('Beam amplitude at the DOE mirror');
figure(4);
plot(sarr,phase2);
xlabel('x (m)');
ylabel('phase (rad)');
title('Beam phase at the DOE mirror');

%%% PLOT THE MIRROR SURFACE
phase3 = ((angle(conj(resultvar))+pi)*wave)/(2*pi))*1e+006;
figure(5);
plot(sarr,phase3);
xlabel('x (m)');
ylabel('Mirror surface (μm)');
title('Mirror surface');
mirrorphase = angle(conj(resultvar));
figure(6);
plot(sarr,mirrorphase);
xlabel('x (m)');
ylabel('Mirror phase');
title('Mirror phase');

%%% PLOT THE BEAM AT THE DOE MIRROR
figure(7);
intensity3a = abs(nextfield);
phase4 = angle(nextfield);
plot(sarr,intensity3a);
xlabel('x (m)');
ylabel('Amplitude (a.u.)');
title('Beam amplitude at stop');
figure(8);
plot(sarr,phase4);
xlabel('x (m)');
ylabel('phase (rad)');
title('Beam phase at stop');

```